Institut für Umweltwissenschaften und Geographie

On the influence of density and morphology on the Urban Heat Island intensity

Yunfei Li

2024

Kumulative Dissertation
zur Erlangung des akademischen Grades
doctor rerum naturalium
(Dr. rer. nat)
in der Wissenschaftsdisziplin
Geoökologie

eingereicht an der
Mathematisch-Naturwissenschaftlichen Fakultät
der Universität Potsdam

Version as of January 15, 2024

Yunfei Li: *On the influence of density and morphology on the Urban Heat Island intensity*

Potsdam
January 15, 2024

Gutachter:
Prof. Dr. Jurgen P. Kropp
Institut fur Umweltwissenschaften und Geographie, Universitat Potsdam
Potsdam-Institut fur Klimafolgenforschung (PIK)

Prof. Dr. Anders Levermann
Potsdam-Institut fur Klimafolgenforschung (PIK)

Institut fur Physik und Astronomie, Universitat Potsdam
Prof. Dr. Dieter Scherer
Leiter des Fachgebiets Klimatologie, Institut fur Okologie
Fakultat VI – Planen Bauen Umwelt, Technische Universitat Berlin

Published online on the
Publication Server of the University of Potsdam:
https://doi.org/10.25932/publishup-62150
https://nbn-resolving.org/urn:nbn:de:kobv:517-opus4-621504

Family means nobody gets left behind, or forgotten.

— Lilo & Stitch

Dedicated to the loving memories of Z.J. Li (1961 – 2011)

千里之行，始于足下

A journey of a thousand miles begins with a single step

— 老子 (Laozi, ca.500 BC)

ABSTRACT

The urban heat island (UHI) effect, describing an elevated temperature of urban areas compared with their natural surroundings, can expose urban dwellers to additional heat stress, especially during hot summer days. A comprehensive understanding of the UHI dynamics along with urbanization is of great importance to efficient heat stress mitigation strategies towards sustainable urban development. This is, however, still challenging due to the difficulties of isolating the influences of various contributing factors that interact with each other. In this work, I present a systematical and quantitative analysis of how urban intrinsic properties (e.g., urban size, density, and morphology) influence UHI intensity.

To this end, we creatively combine urban growth modelling and urban climate simulation to isolate the influence of urban intrinsic factors from that of background climate, so as to focus on the impact of urbanization on the UHI effect. The urban climate model can create a laboratory environment which makes it possible to conduct controlled experiments to separate the influences from different driving factors. The urban growth model provides detailed 3D structures that can be then parameterized into different urban development scenarios tailored for these experiments. The novelty in the methodology and experiment design leads to the following achievements of our work.

First, we develop a stochastic gravitational urban growth model that can generate 3D structures varying in size, morphology, compactness, and density gradient. We compare various characteristics, like fractal dimensions (box-counting, area-perimeter scaling, area-population scaling, etc.), and radial gradient profiles of land use share and population density, against those of real-world cities from empirical studies. The model shows the capability of creating 3D structures resembling real-world cities. This model can generate 3D structure samples for controlled experiments to assess the influence of some urban intrinsic properties in question. [Chapter 2]

With the generated 3D structures, we run several series of numerical climate simulations with urban structures varying in properties like size, density and morphology, under the same weather condition. Analyzing how the 2m air temperature based canopy layer urban heat island (CUHI) intensity varies in response to the changes of the considered urban factors, we find the CUHI intensity of a city is directly related to the built-up density and an amplifying effect that urban sites have on each other. We propose a Gravitational Urban Morphology (GUM) indicator to capture the neighborhood warming effect. We build a regression model to estimate the CUHI intensity

based on urban size, urban gross building volume, and the GUM indicator. Taking the Berlin area as an example, we show that the regression model can predict the CUHI intensity under various urban development scenarios. [Chapter 3]

Based on the multi-annual average summer surface urban heat island (SUHI) intensity derived from Land surface temperature, we further study how urban intrinsic factors influence the SUHI effect of 5,000 largest urban clusters in Europe. We find a similar 3D GUM indicator to be an effective predictor of the SUHI intensity of these European cities. Together with other urban factors (vegetation condition, elevation, water coverage), we build different multivariate linear regression models and a climate space based Geographically Weighted Regression (GWR) model that can better predict SUHI intensity. By investigating the roles background climate factors play in modulating the coefficients of the GWR model, we extend the multivariate linear model to a nonlinear one by integrating some climate parameters, such as the average of daily maximal temperature and latitude. This makes it applicable across a range of background climates. The nonlinear model outperforms linear models in SUHI assessment as it captures the interaction of urban factors and the background climate. [Chapter 4]

Our work reiterates the essential roles of urban density and morphology in shaping the urban thermal environment. In contrast to many previous studies that link bigger cities with higher UHI intensity, we show that cities larger in the area do not necessarily experience a stronger UHI effect. In addition, the results extend our knowledge by demonstrating the influence of urban 3D morphology on the UHI effect. This underlines the importance of inspecting cities as a whole from the 3D perspective. While urban 3D morphology is an aggregated feature of small-scale urban elements, the influence it has on the city-scale UHI intensity cannot simply be scaled up from that of its neighbourhood-scale components. The spatial composition and configuration of urban elements both need to be captured when quantifying the influence of urban 3D morphology as nearby neighbourhoods also cast influences on each other. Our model serves as a useful UHI assessment tool for the quantitative comparison of urban intervention/development scenarios. It can support harnessing the capacity of UHI mitigation through optimizing urban morphology, with the potential of integrating climate change into heat mitigation strategies.

ZUSAMMENFASSUNG

Der städtische Wärmeinseleffekt (engl. Urban Heat Island effect – UHI effect) beschreibt höhere Temperaturen in städtischen Gebieten im Vergleich zur natürlichen Umgebung, was zu erhöhtem Hitzestress für städtische Bewohner führt. Das Verständnis der Dynamik von UHI in Bezug auf die Urbanisierung ist entscheidend für die Entwicklung effektiver Strategien zur Hitzestressminderung und nachhaltigen städtischen Entwicklung. Es bleibt jedoch eine Herausforderung, die Einflüsse der verschiedenen interagierenden Faktoren zu isolieren. In dieser Arbeit präsentiere ich eine systematische und quantitative Analyse, wie städtische intrinsische Eigenschaften wie Dichte und Morphologie die UHI-Intensität beeinflussen.

Um dies zu erreichen, kombinieren wir städtisches Wachstumsmodellieren und städtische Klimasimulation, um den Einfluss städtischer intrinsischer Faktoren von Hintergrundklima zu trennen und den Fokus auf die Auswirkungen der Urbanisierung auf den UHI-Effekt zu legen. Durch Schaffung einer Laborumgebung mithilfe des städtischen Klimamodells können kontrollierte Experimente zur Bewertung der Einflüsse verschiedener Treiberfaktoren durchgeführt werden. Das städtische Wachstumsmodell erzeugt detaillierte 3D-Strukturen, die in verschiedene städtische Entwicklungsszenarien für diese Experimente parametrisiert werden können.

Wir stellen ein stochastisches gravitatives städtisches Wachstumsmodell vor, das 3D-Strukturen mit unterschiedlicher Größe, Morphologie, Kompaktheit und Dichtegradient erzeugen kann. Das Modell wird durch den Vergleich seiner Eigenschaften mit denen realer Städte validiert. Unter Verwendung der generierten 3D-Strukturen werden mehrere Serien von Simulationen unter denselben Wetterbedingungen durchgeführt, um zu analysieren, wie Änderungen städtischer Faktoren wie Größe, Dichte und Morphologie die Intensität der städtischen Wärmeinsel beeinflussen. Die Studie zeigt, dass die bebaute Dichte und der Verstärkungseffekt der städtischen Standorte aufeinander direkt mit der Intensität der städtischen Wärmeinsel zusammenhängen. Wir schlagen einen Gravitational Urban Morphology (GUM)-Indikator vor, um den Erwärmungseffekt in der Nachbarschaft zu erfassen, und entwickeln ein Regressionsmodell, das die Intensität der städtischen Wärmeinsel anhand der städtischen Größe, des Bruttogebäudevolumens und des GUM-Indikators schätzt.

Darüber hinaus untersuchen wir, wie städtische intrinsische Faktoren den Effekt der städtischen Wärmeinsel auf die Oberfläche (SUHI) der 5.000 größten städtischen Ballungsräume in Europa basierend auf dem mehrjährigen durchschnittlichen Sommerwärmeinsel (SU-

HI) ableiten. Ein ähnlicher GUM-Indikator erweist sich als effektiver Prädiktor für die SUHI-Intensität. Durch Berücksichtigung anderer städtischer Faktoren wie Vegetationszustand, Höhe, Wasserversorgung und Einbeziehung von Klimaparametern entwickeln wir verschiedene Regressionsmodelle, die die SUHI-Intensität besser vorhersagen. Das nichtlineare Modell, das Klimaparameter integriert und die Wechselwirkungen zwischen städtischen Faktoren und Hintergrundklima erfasst, übertrifft lineare Modelle in der SUHI-Bewertung.

Die Arbeit betont die Bedeutung von städtischer Dichte und Morphologie für die Gestaltung der städtischen thermischen Umgebung. Sie stellt die Annahme in Frage, dass größere Städte zwangsläufig einen stärkeren UHI-Effekt haben, und hebt den Einfluss der städtischen 3D-Morphologie hervor. Die Studie betont die Notwendigkeit, Städte als Ganzes aus einer 3D-Perspektive zu betrachten, da der Einfluss der städtischen Morphologie nicht einfach von ihren kleineren Bestandteilen hochskaliert werden kann. Unser Modell kann als wertvolles Instrument zur quantitativen Vergleich verschiedener urbaner Interventions- und Entwicklungsszenarien dienen und unterstützt Bemühungen zur UHI-Minderung durch die Optimierung der städtischen Morphologie und die Integration des Klimawandels in Hitzeminderungsstrategien.

PUBLICATIONS

Publications constitute the cumulative thesis:

Y. Li, D. Rybski, and J. P. Kropp (2021a). "Singularity cities." *Environ. Plan. B* 48.1, pp. 43–59. DOI: 10.1177/2399808319843534

Y. Li, S. Schubert, J. P. Kropp, and D. Rybski (2020c). "On the influence of density and morphology on the Urban Heat Island intensity." *Nat. Commun.* 11.1, pp. 1–9. DOI: 10.1038/s41467-020-16461-9

Y. Li, B. Zhou, M. Glockmann, J. P. Kropp, and D. Rybski (2021b). "Context sensitivity of surface urban heat island at the local and regional scales." *Sustain. Cities Soc.* 74, p. 103146. DOI: 10.1016/j.scs.2021.103146

Other Publications:

M. Glockmann, Y. Li, T. Lakes, J. P. Kropp, and D. Rybski (2022). "Quantitative evidence for leapfrogging in urban growth." *Environ. Plan. B* 49.1, pp. 352–367. DOI: 10.1177/2399808321998713

D. Rybski, Y. Li, S. Born, and J. P. Kropp (2021b). "Modeling urban morphology by unifying Diffusion-Limited Aggregation and Stochastic Gravitation." *Findings*, p. 22296. DOI: 10.32866/001c.22296

D. Rybski and Y. Li (2021a). "Chapter 27: Comparing power laws and exponentials in simulations of gravitational growth." *Handbook on Entropy, Complexity and Spatial Dynamics*. Cheltenham, UK: Edward Elgar Publishing. DOI: 10.4337/9781839100598.00037

ACKNOWLEDGEMENTS

This thesis would not have been possible without the aid of many. I want to express my unreserved thanks and appreciation for the help and support from all individuals and organizations.

First and foremost, thanks are due to my first supervisor Prof. Jürgen P. Kropp, for the opportunity of conducting my PhD study in the working group. His breadth and depth of expertise and wisdom in scientific research and beyond have opened my horizon wide. My study has benefited enormously from the professional training and exchange opportunities he has offered. The continuous support, dedicated guidance and advice, and constant encouragement from him have been invaluable for me to overcome the obstacles in both my work and life. I would also like to sincerely thank Prof. Anders Levermann for his willingness to be my second supervisor. I am deeply grateful for his help and support over the years.

I would also like to thank Prof. Dr. Dieter Scherer for reviewing my thesis; Prof. Dr. Annegret Thieken for chairing the examination committee; Prof. Dr. Axel Bronstert, Prof. Dr. Hubert Wiggering for being willing to be members of the committee. I thank all the committee members for their valuable feedback and insights.

I am deeply indebted to Dr. Diego Rybski for his day-to-day supervision. With great patience, substantial dedication, and comprehensive involvement, he has trained me in almost every aspect of doing research, including particularly experimental design, scientific thinking and writing, data analysis and visualization. There were so many times when I felt lost and confused, he led me out with his deep expertise in complexity science and keen insights. The valuable guidance, discussions, support and encouragement offered by him not only have laid the foundation of my doctoral study, but will also foster my future scientific research career. My gratitude to him goes beyond words and I will forever cherish our friendship.

Special thanks are owed to Dr. Bin Zhou, who introduced me to the working group. From the early beginning of my scholarship application, to the finalizing of my thesis, he has continuously helped me in my research work and my daily life. The tremendous support, advice, and encouragement from him, spread throughout my doctoral journey, and will extend way beyond in the future, which I am very sure.

I am sincerely thankful to Dr. Sebastian Schubert, for leading me into the urban climate simulation field, and for the active and critical engagement in my research work. Sincere thanks also go to Dr. Jan

Volkholz and Dr. Christoph Menz for helping me out when I got stuck for several months due to a bug in the numerical model.

I give heartfelt thanks to many helpful and thoughtful people in the Urban Transformations group. Many thanks to Bin, Prajal, Luis and Diego for their comments on the earlier version of my thesis; to Manon and Linda for the help, discussions and suggestions; to Christiane for all the support regarding the administrative issues; to Diego, Luis, Prajal, Christiane, Tobi and Fabian, for the discussions that improved my work in various ways, and for the nice talks that enriched the daily life. Sincere thanks go to all past and present colleagues in the group, for their continuous support and encouragement.

I would also like to extend my gratitude to other colleagues at PIK, especially David and Peggy from the RD2 secretary team, that provided me with various support. Special thanks go to Dr. Yang Liu for helping me with my code at the beginning of my PhD study.

I warmly acknowledge the funding agencies – China Scholarship Council (CSC), for the scholarships which made the research possible, and Potsdam Graduate School (PoGS), for providing many other training opportunities.

Last but not least, I would like to thank my family and friends for their constant support and encouragement.

Yunfei Li

2023 in Potsdam

CONTENTS

LIST OF FIGURES

LIST OF TABLES

ACRONYMS

AIC	Akaike Information Criterion
BUHI	boundary layer urban heat island
CCA	City Clustering Algorithm
CPM	Correlated Percolation Model
CUHI	canopy layer urban heat island
DCEP	Double Canyon Effect Parametrization
DLA	Diffusion-Limited Aggregation
EVI	Enhanced Vegetation Index
GHG	Greenhouse Gas
GUHI	subsurface urban heat island
GUM	Gravitational Urban Morphology
GWR	Geographically Weighted Regression
LULC	land use/land cover
LST	Land Surface Temperature
MODIS	Moderate Resolution Imaging Spectroradiometer
OLS	ordinary least squares
RMSE	root mean-square error
SEB	surface energy balance
SUHI	surface urban heat island
UBL	urban boundary layer
UCL	urban canopy layer
UCP	urban canopy parameters
UHI	urban heat island

1 INTRODUCTION

1.1 RESEARCH BACKGROUND AND MOTIVATION

Cities are the centres where population and social-economic activities concentrate (UN-Habitat, 2016). The period between 1975 and 2015 saw the staggering pace of global urbanization. The world urban population grew by almost 2.4 billion, and cities now house more than half the global population (United Nations 2019, world population). Urbanization improves people's quality of life through better access to jobs, services, education, housing, and health care (Vardoulakis et al., 2019). However, various health, socioeconomic, and environmental problems arise with the rapid urban growth, such as mental disorders (Vlahov et al., 2002) due to stress, pollution and waste, inequality of access to services, infrastructure and resources, traffic congestion, environmental degradation, resource depletion and biodiversity loss (UNEP et al., 2021). The global population is estimated to grow from 7.7 billion in 2019 to 9.7 billion by 2050, while its urban component will experience an increment of 2.5 billion during the same time span, reaching 68% of the world's population. This means that urban areas are expected to absorb virtually all the future growth of the world's population (United Nations Population Division, 2019). Populations, economic activities, social and cultural interactions, as well as environmental and humanitarian impacts, are increasingly concentrated in cities (United Nations Population Division, 2019). This poses massive sustainability challenges to cities in various aspects, especially in terms of climate change and environmental degradation, and places cities on the front line of the climate crises (van den Broek d'Obrenan et al., 2022). The sixth Global Environment Outlook (GEO for Cities) identified five main drivers of environmental change: population growth, urbanization, economic development, technology innovation and sustainability, and climate change — all with strong linkage to cities (UNEP et al., 2021).

Cities are the engines of global economic and development but come with a huge environmental footprint (UNEP et al., 2021). Although cities today occupy approximately only 2% of the total land, they account for 70% economy (GDP), over 60% global energy consumption, 70% global waste and 70% greenhouse gas Greenhouse Gas (GHG) emissions (UN-Habitat, 2016). Therefore, cities have a pivotal role to play, and even have the potential to drive the progress towards the Sustainable Development Goals and targets(UN-Habitat, 2016; UNEP et al., 2021). In 2016 the UN Conference on Housing

and Sustainable Development established a New Urban Agenda (UN-Habitat, 2016; UNEP et al., 2021) which envisages cities as part of the solutions for sustainable development, climate change adaptation, and mitigation (Masson-Delmotte et al., 2021).

At the global scale, cities contribute the majority of anthropogenic GHG emissions, which is the primary cause of human-induced climate warming. At the regional scale, cities cause local warming due to the well-known urban heat island (UHI) effect (Oke, 1973) – enhanced temperature experienced by urban areas compared with the outlying areas, mainly due to the land surface modification from urbanization, and more intensive anthropogenic heat emissions. Consequently, more intense, longer and more frequent heatwaves are estimated to take place in cities due to the warming climate (Masson-Delmotte et al., 2021). This makes cities the hot spots of excessive heat. The heat burdens come with costly impacts on public health and the economy, especially when considering the increasingly concentrated trend of population and infrastructure. Rapid urbanization and urban population growth are expected to happen in the next few decades, with more than half of the growth taking place in Africa and South Asia, predominantly in the tropic areas, places that people are already under severe heat stress. Worse still, elderly people aged 65 or over makes up the world's fastest-growing population group (United Nations Population Division, 2019), increasing the heat venerability of the population.

Therefore, integrated city planning towards urban heat mitigation and reduction will be of particular importance, and the subsequent benefits on health, economy and environment are far-reaching (UNEP, 2021). Most importantly, risks from heat related morbidity and mortality (Tan et al., 2010; He et al., 2022) will be reduced. Secondly, it helps to avoid losses in productivity caused by extreme heat stress. Last but not least, energy consumption for cooling will be saved, which in turn reduces pollution and lowers the urban GHG emissions. Heat-resilient urban planning cannot be achieved without a comprehensive understanding of how urban areas experience and accumulate excess heat – particularly due to the UHI effect, as well as how this process is influenced by urban development. This knowledge is essential for efficient urban planning practices aiming at healthy, climate-resilient, and sustainable cities.

The overarching goal of this work is to advance our understanding on how urban development (usually comes with the changes in, e.g., urban size, density, morphology) influences the UHI effect. So that the improved understanding can be incorporated into urban planning and design practices towards a better urban thermal environment.

1.2 STATUS QUO OF UHI STUDIES

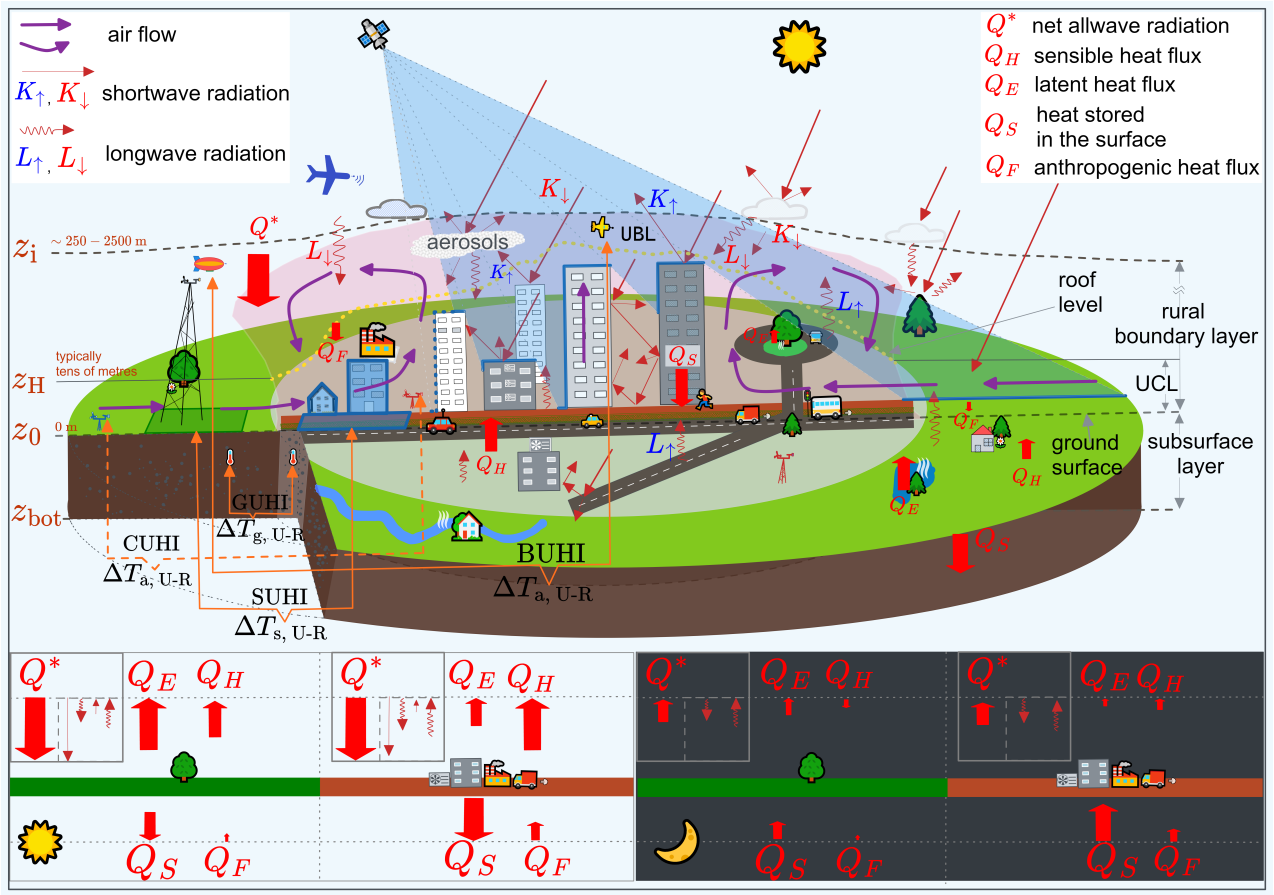

Figure 1.1: Top: Schematic of the structure of the boundary layer over urban areas, and the radiation and energy flux, as well as different urban heat island (UHI) types, during the daytime, under calm and mostly clear condition. Bottom: the surface radiation budget and surface energy balance (SEB) for both daytime and nighttime (note that the size of arrows denotes only qualitatively the relative intensity of the radiation and energy fluxes only under some generalized and simplified ideal conditions – calm and clear summer days, flat terrain, etc. It does not reflect the absolute scale, nor does it necessarily cover all aspects and variations of the complex urban climates. The magnitude and direction of the fluxes may vary depending on specific conditions given the complexity of urban climate and the interactions between its components). The four types of UHI compare at different levels the temperature difference between the city and the countryside at a comparable height. Their detailed definitions can be found in section 1.2.2. (adapted from Oke et al., 2017; Zhou, 2017; Li, 2018; Schubert, 2013; Zhou et al., 2019a; Stewart et al., 2021a.)

1.2.1 *The definition of UHI*

The urban heat island (UHI) effect, which refers to the phenomenon that urban areas tend to experience higher temperatures than their rural/non-urban surroundings, is one of the clearest examples of anthropogenic climate modification (Oke et al., 2017). It can have various impacts on the environment and human health (Grimm et al., 2008). The UHI science has been studied for over 200 years, with its origin dated back to the work by Howard (1818) on the Climate of

London in 1818, which was based on the comparison of near-surface air temperatures of a countryside site and an urban site in the city centre (Stewart et al., 2021a).

Numerous scientific papers emerged along the history of urban climate studies, making the UHI effect one of the most actively studied topics. Especially in recent years, it has attracted considerable research interests due to its association with rapid urbanization and global warming which draw increasing attention (Zhou et al., 2019a). The immense literature on this topic involves cities worldwide with a great diversity of geographical locations and climate settings, including almost all major cities on the globe (Stewart et al., 2021a). Studies on the UHI effect cover a wide range of topics, including (but not limited to):

- the spatial and temporal variations of the UHI (e.g., Zhou et al., 2014; Zhou et al., 2016; Li et al., 2017; Zhou et al., 2018; Geletič et al., 2019; Zhou et al., 2019a; Manoli et al., 2020),
- its influencing factors (e.g., Oke, 1981; Taha, 1997; Shahmohamadi et al., 2011; Peng et al., 2012; Zhou et al., 2014; Zhou et al., 2016; Estoque et al., 2017; Li et al., 2019b; Liu et al., 2021a; Liu et al., 2021b),
- assessment of its impacts (e.g., Tan et al., 2010; Shahmohamadi et al., 2011; Laaidi et al., 2012; Kolokotroni et al., 2012; Georgescu et al., 2013; Estrada et al., 2017; He et al., 2022),
- as well as how UHI interacts with the climate at regional scale (e.g., Georgescu et al., 2013; Li et al., 2013a; Zhao et al., 2014; Chapman et al., 2017; Wouters et al., 2017; Zhao et al., 2018; Khan, 2022), and even beyond (e.g., Kalnay et al., 2003; Cao et al., 2018; Ren et al., 2021; Khan, 2022).

1.2.2 *Heat island types*

There are four distinct types of UHI depending on the schemes used to measure them (Oke et al., 2017; Stewart et al., 2021a). According to the height at which the temperatures are measured, their definitions are (also see Fig. 1.1):

- **Subsurface UHI** (GUHI) – difference between the temperature pattern in the subsurface layer under the city, and that in the subsurface layer under the surrounding non-urban area. The subsurface layer extends from the ground surface (z_o) down to the depth (z_{bot}) of active temperature change over the period of interest. It includes soils and subterranean built fabric.
- **Surface UHI** (SUHI) – difference between the temperatures at the solid-air interface in the city, and those in the rural area. In the city, it is the interface of the outdoor atmosphere with the solid materials, which ideally comprises the three-dimensional complete surface including the ground surface and all exposed facets of

urban elements, e.g., walls, and rooftops. In the rural area, the air-to-ground interface is the equivalent surface.

- **Canopy layer UHI** (CUHI) – difference between the near-surface (typically 2 m above ground) *air temperature* in the urban canopy layer (UCL), and the near-surface air temperature at the corresponding height in the rural area. The UCL lies between the urban ground surface (0m) and the roof level (z_H).
- **Boundary layer UHI** (BUHI) – difference between the *air temperature* (typically 2-4 times the roof height) in the layer between the top (z_H) of the UCL and the top (z_i) of urban boundary layer (UBL), and the air temperature at a similar altitude in the rural boundary layer.

Among them, SUHI and CUHI are the most studied types. The CUHI effect, based on the pedestrian level air temperature which is directly related to thermal comfort of residents, is the UHI type that has the longest study history and has been continuously receiving great research interests. On the other hand, SUHI has gained increasing popularity within the urban climate community in the past few decades, due to the advantages (large spatial coverage, high resolution) and advancement of thermal remote sensing techniques (Zhou et al., 2019a).

However, despite the massive scientific literature on SUHI and CUHI, by the time this work started, research on some important aspects was missing. For example, due to the coverage of records, few researchers investigated at city scale the response of CUHI to urban development; studies linking the SUHI intensity with city-scale factors usually do not consider the heterogeneity in the spatial arrangement of urban elements.

1.2.3 *The physical mechanism of UHI*

Many of the factors and processes determining the UHI have been discussed nearly two hundred years ago by Luke Howard. Following-up studies kept adding facts that confirm and broaden our understanding of the formation of UHI and the underlying mechanisms (Zhou, 2017).

Given the temporally and spatially dynamic feature of the UHI effect and the underneath processes, to slightly simplify the discussion, hereafter throughout this text, we restrict the weather conditions by referring to **calm, clear sky, summertime cases** unless explicitly otherwise specified.

Energetic basis

The root cause of the UHI is the modification of land surface coming along with urbanization, which leads to changes to the surface energy balance (SEB). These alterations to SEB further lead to the divergence in cooling/heating rates between the urban area and its surrounding

rural area. The UHI effect logically begins at the urban surface (Stewart et al., 2021a), where sealed ground and built fabric (e.g., walls, rooftops) differ from the natural landscape in their radiative, thermal, moisture and aerodynamic properties. These differences, together with the geometrical arrangements of the building elements, affect the SEB through determining the distribution and partition of radiation absorbed by the surface (Mirzaei et al., 2010; Oke et al., 2017). Generally, compared with the natural landscape, the urban surface favours more heat storage and trapping and less evapotranspiration cooling.

Under calm conditions when the contribution from convection can be ignored, the energy balance of the urban surface can be expressed as:

$$Q^* + Q_F = Q_H + Q_E + Q_S \,, \tag{1.1}$$

where

Q_H is sensible heat flux to the atmosphere,

Q_E is the latent heat flux to the atmosphere,

Q_S is the heat stored in the substrate,

Q_F is the anthropogenic heat flux,

Q^* is the net allwave radiation which is determined by the surface radiation budget as:

$$Q^* = K_\downarrow - K_\uparrow + L_\downarrow - L_\uparrow \,, \tag{1.2}$$

where

$K_\downarrow$ is the incoming shortwave radiation,

$K_\uparrow$ is the outgoing shortwave radiation,

$L_\downarrow$ is the incoming longwave radiation,

$L_\uparrow$ is the outgoing shortwave radiation.

The energy balance of the urban surface differs from that of vegetated land in various aspects, resulting from many tangled processes that cause the variations in the components of Eq. (1.1) and (1.2) (see Fig. 1.1).

From the perspective of radiation budget, the urban surface generally has a smaller albedo than the land surface in the rural area, which leads to less shortwave reflectance ($K_\uparrow -$). The geometry of street canyons enables the multiple reflections (e.g., from wall to wall, from lower roof to wall, as illustrated in Fig. 1.1) of both short and longwave radiation between facades. This trapping effect results in reduced outgoing shortwave ($K_\uparrow -$) and longwave ($L_\uparrow -$) radiation (Oke, 1981).

From the perspective of SEB, the urban-rural Q^* difference can be ascribed to the unique thermal, moisture and aerodynamic properties

of urban surface (Mirzaei et al., 2010; Oke et al., 2017). Firstly, urban surface, composed of impervious sealing and building/infrastructure with asphalt and concrete of high thermal capacity, and high thermal conductivity, has a stronger ability to uptake and conduct heat into the substrate, namely, into the fabric of the city which includes its construction materials, trees and ground (Q_S+). Secondly, compared with the natural surface with more vegetation, soil and surface water moisture, the urban surface exhibits reduced latent heat flux (Q_E-) due to less evapotranspiration. In addition, urban surfaces featuring buildings and street canyons have reduced overall wind ventilation as a consequence of increased roughness. This constrains the heat dissipation through further more sensible heat (Q_H) transfer into the atmosphere (note this does not mean the Q_H in the urban surface is smaller than that in rural surface). Lastly, anthropogenic heat (Q_F+) released from human activities also adds to the accumulation of heat. Anthropogenic heat can warm both the atmosphere (car exhausts, factory chimneys, air conditioning, etc.) and the surface (pipes, cables, sewers, etc). It has to be noted that, when compared to net allwave radiation, anthropogenic heat can range from dominant to negligible, depending on the location, season, and energy consumption. The combined effect of these features makes cities distinct in heat storage, and consequently form the UHI (Oke et al., 2017).

The formation of different types of UHIs

In general, the dynamic of heat storage Q_S of the SEB over time is the primary driver of different types of UHI and their diurnal courses. Typically, in the morning during hot days, when the urban surface is initially cool, a large proportion of the net allwave radiation Q^* is transferred into heat storage. The Q_S accumulates as a result, and the surface warms up, forming the SUHI gradually after the warming rate of urban surface surpasses that of rural area. In the afternoon, even the deeper canyon floor and shaded areas that cannot be reached directly by solar radiation ($K_\downarrow$) warm up. The accumulated Q_S also reaches the underground soil, creating the subsurface urban heat island (GUHI). After building materials and soils arrive at equilibrium and Q_S saturates. The surface discharges more heat in the form of turbulent fluxes, namely, the latent heat fluxes Q_E and especially the sensible heat fluxes Q_H (see bottom left on Fig. 1.1). During the night when solar radiation is absent, the urban surface is still warmer than that of the rural area due to the higher heat storage and slower cooling rate (canyon trapping, polluted atmosphere, higher heat inertia). The heat stored in the fabric (Q_S) is channelled as longwave radiation ($L_\uparrow$) and slight sensible heat fluxes Q_H into the atmosphere (see the bottom right on Fig. 1.1). This makes the air temperature warmer than that of rural areas, resulting in more pronounced canopy layer urban heat island (CUHI). At night, both urban canyon geometry and

air pollutants contribute positively to CUHI formation by trapping the longwave radiation. The sensible heat fluxes Q_H reach the upper atmosphere and warm up the air in the UBL and contribute to the boundary layer urban heat island (BUHI).

Other influencing factors

Aside from the urban intrinsic properties that distinguish the urban surface from that of rural areas, the UHI effect, as per its definition, is susceptible to the impacts of regional synoptic conditions, seasonal climate, and topography (Stewart, 2011; Oke et al., 2017; Chapman et al., 2017; Li, 2018; Zhou et al., 2019a). Particularly when it comes to quantifying the UHI magnitude, the rural area, as the reference, its surface energy balance (SEB) is primarily controlled by the surface status (e.g., soil moisture, vegetation cover, aerodynamic roughness, albedo, emissivity, and thermal admittance, etc.) (Oke et al., 2017; Zhou et al., 2019a). Additionally, the cloud cover can narrow the urban-rural difference in heat storage during the day, and lower the cooling rate for both urban and rural areas during the night. Therefore, the difference signal is attenuated, and it can be further diminished by the wind that fosters urban-rural heat transfer through advection (see the airflow as illustrated in Fig. 1.1).

1.2.4 *Methodology of UHI studies*

There are a great variety of methods for studying the UHI effect (Oke et al., 2017; Deilami et al., 2018; Kim et al., 2021). Most of the studies can be categorized into 2 groups with respect to the methodology: *empirical studies*, and *modelling studies*. The former consists of diverse observational techniques and the latter involves various modelling strategies.

Empirical studies are based on observations obtained from sensors onboard ground-based, aerial and remote sensing platforms (see on the left of Fig. 1.1). Depending on the properties and processes of interest, temperatures can be recorded from, either fixed or mobile stations, or remote sensors, to sample within a certain range of space and time (Oke et al., 2017; Stewart, 2011).

Modelling studies usually resort to either physical models or numerical models. Physical modelling is conducted in the manner of mimicking real-world urban systems with a surrogate constructed from simplified and scaled urban elements. Depending on the objectives and experiment design, the climatic environment settings can be realistic outdoor weather or artificial conditions generated in a laboratory (Oke, 1981; Oke et al., 2017). Numerical models can simulate real-world processes using a set of governing equations based on the principle of momentum, mass and energy conservation (Mirzaei

et al., 2010). The models partition the space into different volumes, and simulate the exchanges of energy, mass and momentum between them by solving the equations with given boundary and lateral conditions that usually come from field observations and from another model at a larger scale, respectively (Mirzaei et al., 2010). A variety of models have been developed for urban climate studies, with a great diversity in sophistication and scale suitability (Mirzaei et al., 2010; Theeuwes et al., 2014; Schubert, 2013; Oke et al., 2017; Li, 2018; Zhou, 2017).

Both empirical and modelling approaches come with advantages and disadvantages (Mirzaei et al., 2010). For example, empirical studies based on robust observations have the ability to resolve the influences from all the real-world factors that cast their footprints. On the other hand, it also means casual attributing can be very complicated due to the entangled processes jointly controlled by different factors. In addition, access restrictions, measurement errors, noise contamination, and discontinuous records can make the samples lack suitable spatial-temporal coverage (Li, 2018; Oke et al., 2017). As a result, it is impossible to record all combinations of scenarios, especially when the occurrence possibility of the interested ones or their analogues is low under the present context. Moreover, deployment and maintenance of the instrument sometimes can be costly (Mirzaei et al., 2010; Oke et al., 2017).

In contrast, modelling approaches enable well controlled experiments that can greatly simplify the order of complexity by isolating certain processes of interest (Mirzaei et al., 2010; Oke et al., 2017). In some cases, studies can only be done through simulation as ideal observation scenarios cannot be satisfied due to the complex interactions between different driving factors. Yet due to the simplified nature of the simulations, not all processes can be captured in the model. It also requires great effort in model design or input parameterization to achieve appropriate similarity between the simulated and the real-world conditions at different scales, thus reliability of the models needs to be assessed against field observations (Mirzaei et al., 2010; Oke et al., 2017). The time and resource expenses can be also high considering the infrastructure (e.g., construction costs of a physical model, computational resources for numerical modelling) required to conduct the modelling.

1.2.5 *SUHI vs. CUHI*

While each type of UHI has a seemingly straightforward definition, great methodological complexity can arise when it comes to studying them. This complexness results from the mixed nature of the processes that control the UHI formation. Each type of UHI is linked to its own set of primary drivers, resulting in distinct spatial/temporal patterns and dynamics of them (Oke et al., 2017). This in turn influences

the suitability of how the temperatures are obtained and how the UHI magnitude is quantified, especially when considering that scale matters in the UHI studies. This is particularly true for the two most studied UHI types — SUHI and CUHI.

The SUHI effect reflects the urban-rural difference in the surface energy balance (SEB) which is responsible for many observed urban climate effects (Oke et al., 2017; Zhou et al., 2019a; Stewart et al., 2021b). Studying the SUHI effect helps to better understand the SEB at different scales, and therefore are relevant to the mitigation of many adverse urban climate effects. The underlying processes of UHI formation (see 1.2.3) suggest that the surface temperature (T_s) is critically important to near-surface air temperature (T_a), as it is mainly the heat released from the surface during the night that slow down the cooling rate of the near-surface air, and causes the CUHI.

Although SUHI and CUHI are closely connected through mass, energy, and momentum exchanges primarily driven by the SEB (Stewart, 2011), they behave differently in their diurnal courses. Usually, SUHI reaches its maximum during the day, while CUHI peaks in the middle of the period of darkness. The diurnal profiles and the timing of their peaks depend on the urban and rural surface properties.

CUHI and SUHI also intrinsically favour different monitoring schemes and study methodologies, mainly due to different media for which the temperatures are sensed, and where the media lie. Due to the spatial heterogeneity of the myriad urban fabrics, the surface temperature estimated by thermal remote sensing, provides the most favourable data source for studying the SUHI, due to its unparalleled advantages (e.g. high spatial resolution and coverage, cost-efficient, easy data accessibility) (Zhou et al., 2019a). However, spatial and temporal coverage of LST can be reduced to different extents due to the trade-off issue between spatial and temporal resolution of satellite imagery, and due to the missing values caused by the cloud contamination (Wan et al., 2015; Deilami et al., 2018). As for the air temperature on which the CUHI is based, spatial characteristics of near-surface temperature may be resolved with acceptable accuracy by interpolating records from sufficiently dense (though usually not available) in situ observations. However, long time series of air temperature records from dense observation networks usually are not available due to practical difficulties (see section 1.2.4) of obtaining high spatio-temporal coverage air temperature observations.

Difference in the temperature records also leads to different manners of quantifying the magnitude of SUHI and CUHI, especially when taking into account that the UHI intensity is also critically subject to the properties of the rural surface (see the passage in 1.2.3). The diverse data preprocessing operations for temperature records screening, inevitably lead to inconsistency in the methodology of individual studies of both CUHI and SUHI (Stewart, 2011; Stewart

et al., 2021a; Stewart et al., 2006). This makes it rather difficult to generalize the knowledge through comparing UHIs across cities or studies, especially when they lack congruences and sometimes even have contradictory findings. Moreover, the ambiguity in urban/rural definition exacerbates further the incomparability due to the lack of a common urban/rural delineation method.

1.3 THE IMPACTS OF UHI

The UHI effect has various impacts on the local environment and human health (Grimm et al., 2008).

During hot days, the UHI effect can raise energy demand for cooling (Hsieh et al., 2007; Li et al., 2014), which in turn leads to an increase in pollutant, greenhouse gas emissions and waste heat from fossil fuel combustion for energy supply (UNEP, 2021; Khan, 2022). The rural-urban air circulation driven by the UHI effect pulls more moist air from the rural area and forms greater upward motion, which is favourable conditions for cloud formation over the urban area and thus induces additional shower and thunderstorm events (Li et al., 2020b). UHI also impairs water quality as hot pavement and rooftop surfaces transfer their excess heat to storm-water run-off, which can lead to a raised temperature of local water bodies, stressing the aquatic ecosystems (UNEP, 2021; Khan, 2022).

Apart from adverse impacts on the environment, the UHI effect has various direct and indirect impacts on urban dwellers and their health (Grimm et al., 2008; Patz et al., 2005; Eliasson, 2000). The most direct impacts are heat-related health problems (Tan et al., 2010) and increased risk of heat morbidity and mortality (Gabriel et al., 2011; Krummenauer et al., 2019) during hot summer days, as in many cities the UHI effect exposes urban dwellers to extra heat stress. In particular, during heat wave events, the UHI effect increases the frequency of extreme heat events, extends the duration of high temperatures, and narrows the time window for relief from high-heat exposure (Zhao et al., 2018; Schatz et al., 2015; Tan et al., 2010). As a result, the risk of heat morbidity and mortality increases (Tan et al., 2010; Zhao et al., 2018; Habeeb et al., 2015; Gabriel et al., 2011).

The impacts can be further exacerbated when the UHI effect interacts with urbanization and climate change, since it will lead to prolonged and intensified hot conditions (Heaviside et al., 2017; Chapman et al., 2017). Warming enhanced by urbanization has been identified in many cities and regions (Cao et al., 2018; Kalnay et al., 2003; Argüeso et al., 2014; Georgescu et al., 2013), which implies more severe heat stress in the future. Moreover, urban areas are expected to absorb all the future global population growth which is estimated to be 2.2 billion by the end of this century (United Nations Population Division, 2019). This means in the future many more people will be

exposed to more frequent and intense extreme heat events, let alone the demographic change with an increasing proportion of vulnerable elderly people. Therefore, urban development policies need to take the UHI effect into account (Estrada et al., 2017) and make proper use of effective ways to reduce excessive urban heat.

1.4 RESEARCH GAPS AND RESEARCH QUESTIONS

1.4.1 *Research gaps*

As more than half of the world's population now lives in cities and this share is expected to continue growing in the future (United Nations Population Division, 2019), urban development that avoids stronger UHI can help to reduce the heat risk and costs, especially under the background of global warming (Estrada et al., 2017). Rapid urban growth poses challenges to urban heat mitigation, but it also presents important opportunities to implement urban climate knowledge in newly developing areas. In this way, urban development can take place in a way that does not create a strong UHI effect in the first place instead of reducing the urban heat after growth.

Since there is no single best design that meets climate objectives at all scales, urban planning requires a multi-scale perspective (Oke, 1984; Oke, 2006; Mills, 2006; Mills et al., 2010; Oke et al., 2017). Design interventions have to be conducted in a coordinated and balanced manner that brings different parts together and evaluates the climate impacts via tools suitable for different scales (Oke, 2006; Mills, 2006; Mills et al., 2010). Benefits of some local interventions like increasing vegetation space (Schubert et al., 2013), green roofs (Straka et al., 2019), and cool coating of buildings and infrastructure (Ng, 2012) have been proven by a great number of both numerical and empirical studies.

However, it is also necessary to inspect at the city scale and to consider the urban system as a whole which is the totality of tightly connected and constantly interacting components (Oke et al., 2017). Especially, when there is a need for more built-up space to house the growing population while the developable area is limited, where and how to grow are equally important. Because the environmental impacts of an area usually transcend the local scale, and the resource quota for the whole city is bounded. This calls for a quantitative tool that can evaluate the UHI effect from different urban development scenarios at the city scale. Yet that is still challenging due to the research gaps which impede robust quantitative assessment of the UHI intensity in view of urban development. Mainly they are :

- At the city scale, studies linking the CUHI intensity to factors like urban size, density, and morphology are missing.
- Although many researchers studied at the city scale the relationship between the SUHI intensity and urban size and 2D

shape, few covered the influences of the internal configuration urban components, for instance, urban density and its spatial arrangement.

- Most studies analyse the influence of climate factors qualitatively, a few studies integrate climate factors into their multilinear SUHI predicting models, while the nonlinear influence is less explored.

This is partly due to the data availability issues (e.g., spatial-temporal coverage of temperature data, 3D urban structure data). Another major difficulty is to separate the influence of urban factors from that of the background climate, due to the fact that a myriad of factors influencing UHI, and they interact with each other in a super complex manner (Chapman et al., 2017). For instance, studies that compare the UHI of different cities face the problem of difference in climate settings. Even when an individual city is studied, urban development still involves the changes in urban size, density, and morphology. Influence from a specific aspect can hardly be separated from the others. In addition, the background climate varies over the time of urban development.

In this work, we advance the knowledge by systematically designing controlled experiments, and strive to get a comprehensive understanding through quantitative analysis on how the intensity of UHI (with a particular focus on CUHI) is determined by some key urban intrinsic factors (e.g., urban size, density, morphology) at the city scale, aiming to gain knowledge that can support quantitative UHI assessment, and thus support urban heat mitigation practices in view of urbanization.

The main research questions and the motivations are detailed below.

1.4.2 *Research Question 1*

It is of great methodological complexity to study the UHI effect, mainly due to the huge number of potential contributing factors and their non-linear interactions through the mixed processes lying underneath. Many factors and the relevant processes play a role in the formation of UHI, which includes particularly, the background climate (Zhao et al., 2014), thermal properties of the rural surface (Runnalls et al., 2000), city size (Oke, 1973), density (Oke, 1987), urban form (Middel et al., 2014), street geometry (Eliasson, 2000; Oke, 1987), and building material (Chapman et al., 2017; Oke, 1987).

Case studies for a specific city based on observations with a limited spatial-temporal resolution often end up with some simple linear regression models (Zhou et al., 2018; Kim et al., 2021) while the nonlinear interacting effects are rarely captured. Aside from that, it is unlikely that the observed UHI variation results from the change

of a single one of these factors, due to the fact that the city-scale influencing factors (such as urban size, density, and morphology) evolve together over time. Things become even more complicated when taking the nonlinear effect from background climate parameters into account (Manoli et al., 2019; Yu et al., 2018) as they also vary temporally. Cities in existing studies vary from one to another on their background climate and surrounding environment, as well as the extremely diverse schemes (see section 1.2.5) for data acquiring and UHI quantification, which makes it extremely difficult to put different results together and to compare them to get a general quantitative understanding (Chapman et al., 2017).

Facing these challenges, one can easily think of numerical modelling approach, as it enables well controlled experiments to isolate the influence from factors of interest. And meanwhile, it provides a seamless temperature map at designed spatial/temporal coverage and resolution. Despite that, the numerical modelling approach has its own disadvantages as also discussed in the part 1.2.4, namely, the huge effort for input data parameterization, numerical computations, and model validation. Urban climate models that consider many factors at high resolution, in turn, need detailed spatial distribution of these factors so that they can be parameterized as input data (Schubert, 2013; Li, 2018). Most of the factors driving the UHI effect show great heterogeneity and some are even featured with 3 dimensions (Schubert et al., 2012; Li et al., 2019b). It is very difficult to find the suitable sample from the real-world data to do controlled experiments.

Therefore, the first research question (RQ1) we need to address is: How to systematically and quantitatively study the relationship between the UHI effect and some key urban intrinsic properties (e.g., urban size, density, morphology, etc.) at the city scale with reduced complexity?

1.4.3 *Research Question 2*

The relationship between urban morphology and the UHI effect is a long-standing topic that attracts plenty of research interest.

Logically, urban morphology, as a city scale indicator, should be linked to the UHI effect also at the city scale. This is the reason why most studies explore the relationship between SUHI and 2D urban morphology since both of them can be quantified from spatially explicit remote sensing maps at the city scale. Some previous investigations have found that many aspects of urban form (such as overall dimensions, skyline, poly-centricity and sprawling/compactness) (Oke et al., 2017) are related to the SUHI intensity (Zhou et al., 2018; Zhou et al., 2017). For example, in order to reduce the noise from the background climate, Zhang et al. (2012) analysed the SUHI of 42 northeastern US urban areas within a similar ecological context, and

they found a linear relationship between the SUHI intensity and an urban shape indicator calculated as logarithmic urban area-perimeter ratio. Some studies also qualitatively explored the climate sensitivity of the relationship between SUHI and urban morphology. For instance, from the statistics based on the 5,000 largest urban clusters in Europe, Zhou et al. (2017) found that a compact urban form featured with large box-counting fractal dimension and a smaller anisometry tends to increase the summer SUHI intensity whilst the influence varies regionally. In a more recent work, Liu et al. (2021b) examined the relationships between different urban form metrics and the SUHI intensity based on 1288 urban clusters in China, and they found these relationships vary with the climate zones.

Results from SUHI studies suggests the potential of urban morphology to mitigate urban heat stress. However, when it comes to the relationship between the CUHI intensity and urban morphology, the first challenge is that CUHI magnitude is usually calculated based on 2-m air temperature data from in situ observations. These temperature records, cannot represent the CUHI pattern at the city scale unless they come from a sufficiently dense station network, which is usually not available due to practical reasons (see the disadvantages of field observation of part 1.2.4). The mixed processes through which both the urban intrinsic properties and background climates control the CUHI effect present another challenge for addressing this question. Therefore, it is hard to compare the CUHI intensities of different cities of various forms, as their climate backgrounds also differ. Similar problems arise when trying to look at the CUHI development along with the growth of a specific city, due to the dynamic of climates within the same time span. Apart from this, the availability of such air temperature records with sufficient coverage of space and time is another commonly existing problem.

Urban morphology is a factor highly relevant to the urbanization process, better knowledge of the CUHI effect and urban morphology relation helps to understand how UHI and the urban climate evolve along with future urban growth. As the near air temperature is more relevant to the thermal comfort of urban residents, the question that would naturally emerge is that:
How does urban morphology influence canopy layer UHI?

This is the focus of our second research question (RQ2). The major challenge being faced is to find a proper 3D urban morphology indicator that links quantitatively with the CUHI intensity.

1.4.4 *Research Question 3*

With the great advantages of doing controlled simulations with a high spatial-temporal resolution, numerical modelling provides a powerful tool which makes it possible to address the research question

above. At the same time, urban climate models suffer from limited spatial/temporal coverage and difficulty in fast application, mainly due to the high demand for computational resources and input data parameterization. This further constrains the fast application of the knowledge gained from urban climate simulations on other cities. Without running more simulations for model validation, a regression model developed from one specific city usually cannot be directly applied to another one that has a different climate setting.

Instead, remote sensing data have been widely used for urban thermal studies, and have great advantage of spatial coverage for Land Surface Temperature (LST) based SUHI study (Manoli et al., 2019). Although SUHI varies in physical mechanism from CUHI, they are found to be highly related (Zhou, 2017; Li et al., 2019b), and both of them are important indicators of urban thermal properties (Oke et al., 2017; Zhou et al., 2019a). Studying how the background climate factors influence relationships between the SUHI and some urban intrinsic factors can improve our understanding of how they jointly impact the SUHI effect (Oke et al., 2017).

Although many researchers studied at the city scale the relationship between the SUHI intensity and urban factors (i.e., urban size and morphology), few covered the influences of the internal configuration urban components, for instance, urban density and its spatial arrangement. In addition, how the background climate determines the relationship is less explored. Despite that similar topic has been covered in some existing studies and the influences from background climate have also been discussed qualitatively (Zhang et al., 2012; Peng et al., 2012; Zhou et al., 2013; Zhou et al., 2017; Li et al., 2017; Liang et al., 2020; Liu et al., 2021a; Liu et al., 2021b), very little effort has been addressed towards quantitative analysis of the interaction between background climate and urban factors due to the complex non-linear interactions of those factors (Manoli et al., 2020).

Therefore, our third research question is:
How do urban intrinsic factors, in particular urban density and morphology, determine the SUHI effect? How is the process controlled by the background climate?

1.5 STRUCTURE AND CONTENTS OF THE THESIS

To address the research questions above, we combine urban growth modelling and urban climate simulation to separate the urban structure factors from background climate influences, and to focus on the impact of urbanization on the UHI effect. The urban climate model enables to study driving factors separately by running controlled experiments and the urban growth model provides detailed 3D urban scenarios tailored for those experiments. The whole project is partitioned into 3 parts, which are the urban growth model, CUHI analysis

and SUHI analysis, respectively. While each subtopic provides support for its following ones, the second part is the focal work.

In Chapter 2 we propose a 3D stochastic gravitational urban growth model. The model provides artificial 3D urban structures for controlled urban climate simulations.

In Chapter 3 we simulate the urban climate of various generated cities under the same weather conditions. These controlled simulations enable us to isolate the influence of a specific urban factor (i.e., city size, density and urban morphology) from other urban factors and background climate.

In Chapter 4 we explore spatial variation of the influence of urban morphology and size on the SUHI intensity based on remotely sensed land data. With a Geographically Weighted Regression (GWR) model we analyse quantitatively how background climate parameters control the influences of urban morphology and size on the SUHI intensity. We propose nonlinear model that can predict SUHI intensity for cities across climate zones by incorporating climate factors.

In Chapter 5, I summarize our findings and achievements, discuss some limitations of this work, and shed light on potential future work.

2

STOCHASTIC GRAVITATIONAL URBAN GROWTH MODEL[1]

ABSTRACT

We propose an upgraded gravitational model which provides population counts beyond the binary (urban/non-urban) city simulations. Numerically studying the model output, we find that the radial population density gradients follow power-laws where the exponent is related to the preset gravity exponent γ. Similarly, the urban fraction decays exponentially, again determined by γ. The population density gradient can be related to radial fractality, and it turns out that the typical exponents imply that cities are basically zero-dimensional. Increasing the gravity exponent leads to extreme compactness and the loss of radial symmetry. We study the shape of the major central cluster by means of another three fractal dimensions and find that overall its fractality is dominated by the size and the influence of γ is minor. The fundamental allometry, between population and area of the major central cluster, is related to the gravity exponent but restricted to the case of higher densities in large cities. We argue that cities are shaped by power-law proximity. Our work contributes to the understanding of gravitational effects, radial gradients, and urban morphology. The model allows to generate and investigate city structures under laboratory conditions.

KEYWORDS:

Gravity models, population density, urban fraction, fractal geometry

1 This chapter is based on the published paper: Y. Li et al. (2021a). "Singularity cities." *Environ. Plan. B* 48.1, pp. 43–59. DOI: 10.1177/2399808319843534, Copyright © The Author(s) 2019.

2.1 INTRODUCTION

The large number of processes working in cities make them complex objects extending over a range of spatio-temporal scales (White et al., 2015; Barthelemy, 2016). As pointed out by Batty (2013), a city science that explains city growth, sprawl, etc. needs to be supported by theories about how people relate to each other. Despite ongoing digitalization and globalization, geographical proximity still matters (Morgan, 2004). The small distances within cities, as extreme agglomerations, attract urbanites and thereby enhance the proximity.

Certainly, ideas of geographical gravitation have a long tradition and can be traced back to the middle of the 20th century and beyond (Zipf, 1946; Stewart, 1948; Carrothers, 1956). In view of new empirical findings we revisit and extend a probabilistic city model (Rybski et al., 2013) from two states (non-urban, urban) to population counts. Specifically, we validate it against recent findings of urban fraction and population density gradients (Lemoy et al., 2020) as well as of building heights within cities (Schläpfer et al., 2015).

The model to a large extent reproduces the features described for real-world cities. The numerical simulations enable us to relate both works to each other as well as to other properties including 4 different measures of city fractality and the fundamental allometry, i.e. between population and area of cities. Interestingly, the population density gradient decaying with the radial distance to the power -2 as found in Lemoy et al. (2017) corresponds to a fractal dimension of 0, which supports the point character of cities, i.e. singularities in space. We complement the numerical analysis by economics arguments employing travel costs as well as housing rent determined by supply and demand.

2.2 MODEL

We consider a two-dimensional square lattice of size $N \times N$ whose sites w_j with coordinates $j \in \{(1 \dots N, 1 \dots N)\}$ can be empty (0) or occupied by an integer number of 'inhabitants'. The probability that an inhabitant is added to a site is

$$q_j = G \frac{\sum_{k \neq j} w_k d_{j,k}^{-\gamma}}{\sum_{k \neq j} d_{j,k}^{-\gamma}} \quad , \tag{2.1}$$

where $d_{j,k}$ is the Euclidean distance between the sites j and k. The denominator compensates for the border effects of the finite system. The exponent $\gamma > 0$ is a free parameter that determines how strong the influence of occupied sites decays with the distance. The constant G (exogenously) determines the overall growth rate and is given by $G = g / \left(\max \frac{\sum w d^{-\gamma}}{\sum d^{-\gamma}} \right)$ where the parameter g is used to tune the speed of growth ($0 < g \leq 1$).

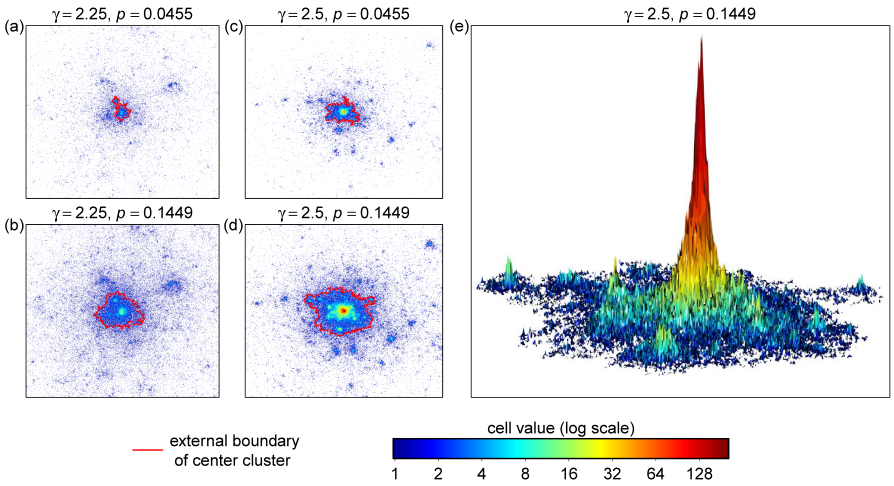

Figure 2.1: Examples of city structures generated by the model, Eq. (2.1). For panels (a) and (b) $\gamma = 2.25$ was used and for (b) and (c) it was $\gamma = 2.5$. For better comparability, in (a) and (c) as well as (b) and (d) iterations with approximately the same fraction p of occupied cells were chosen. The colour bar indicates the number of 'inhabitants' in the cells (in log scale). The red line in (a)-(d) shows the boundary of the major central cluster. Panel (e) is a 3-dimensional illustration of the major cluster from (d), whereas the third dimension is in linear scale.

We start with an empty grid ($w_j = 0$ for all j) and, without loss of generality, put one inhabitant on the single central site. In every iteration, a random number z is drawn (from a uniform distribution between 0 and 1) for each grid cell with coordinates j and if $z < q_j$ then w_j is incremented by 1. We consider w as population counts in each grid cell. The procedure is repeated and stopped before the major central cluster reaches any of the system boundaries. Figure 2.1 shows examples of the emerging structures.

This version differs from the original model (Rybski et al., 2013) only by (i) the w_j which originally were 0 or 1 and (ii) the g which originally was fixed to $g = 1$, so that the maximum probability was 1. Please see Rybski et al. (2013) for details.

For some analyses, we extract the major cluster by applying the City Clustering Algorithm (CCA) (Hoshen et al., 1976; Rozenfeld et al., 2008; Rozenfeld et al., 2011; Fluschnik et al., 2016; Kriewald et al., 2016) with $l = 1$, i.e. only connecting nearest neighbours. The area A_c of the major cluster is given by the number of cells with $w > 0$ belonging to the cluster. Analogously, the total population S_c of the cluster is defined by the sum over w it consists of. For each major cluster, we extract its envelope, i.e. those cells which have at least one empty (nearest) neighbour which is not part of a hole within the cluster. We denote the number of cells the envelope consists of as perimeter C, and the largest distance from the envelope to the central cell of the lattice as R_c.

The cells of the grid can also be understood as plots for buildings and the w_j as the height of the buildings. Assuming each floor corresponds to one apartment and each apartment is home to one person, then w_j corresponds to the number of inhabitants. More apartments per floor or more persons per apartment only represent a factor. We assume homogeneity, i.e. living space per person is constant throughout the city.

2.3 ANALYSIS

On a square lattice of size 1000×1000 we run 10 realizations for various γ-values. As with the same normalization constant g a larger γ requires more iterations to fill the lattice, we take different normalization constants g for different γ-values to balance between the need of enough iterations and the computational time. Specifically, we run simulations for $\gamma = 2.0, 2.05, \ldots, 2.7, 2.75$ with $g = 0.02, 0.02, 0.1, 0.1, 0.1, 0.1, 0.2, 0.5, 0.5, 0.5, 0.5, 1, 1, 1, 1, 1$ respectively. All iterations where the major central cluster is smaller than 200 occupied cells are excluded during the post-processing. We end up with approximately 1700 useful iterations in total for $\gamma = 2.0$. The number of iterations increases with γ.

2.3.1 *Radial gradients*

First we want to study the gradients generated by the model and compare them with empirical results (Guérois et al., 2008; Peiravian et al., 2014; Lemoy et al., 2020). Following Lemoy et al. (2020) we define concentric rings around the initial central cell and calculate within them the population density and urban fraction. We also apply the rescaling proposed in (Lemoy et al., 2020).

2.3.1.1 *Population density gradient*

The density is given by $D(r) = \sum_k w_k / \sum_k 1$, where k is the index representing all cells at a distance between r and $r + \delta r$ from the centre. In this study the width of the rings is $\delta r = 1$. We only take rings up to R_c into account.

We rescale the population density according to

$$r^* = \frac{r}{S^{1/3}} \qquad D^*(r) = \frac{D(r)}{S^{1/3}} \tag{2.2}$$

as proposed in Lemoy et al. (2020). It can be seen in Fig. 2.2, that the rescaled curves collapse (Stanley, 1999; Malmgren et al., 2009), i.e. they reasonably well fall onto each other.

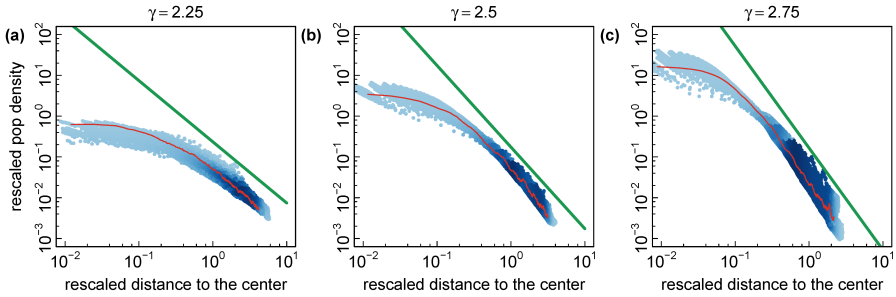

Figure 2.2: Population density gradients. The rescaled population density is plotted as a function of the rescaled distance to the centre, both according to Eq. (2.2), for (a) $\gamma = 2.25$, (b) $\gamma = 2.5$, and (c) $\gamma = 2.75$. All panels are in log-log scale. Due to rescaling the values of all realizations and iterations fall onto each other. The shades of blue represent densities, the red line corresponds to the data of an individual curve, and the straight green line is a guide to the eye with slope given by Eq. (2.5). The population density asymptotically decays as power-law.

Specifically, we find that the population density decays following a power-law

$$\frac{D(r)}{S^{1/3}} \sim \left(\frac{r}{S^{1/3}}\right)^{-\alpha} \tag{2.3}$$

for $r^* > r_p^*$, where r_p^* is the rescaled radius at which the plateau ends and the power-law decay begins. Rescaling does not affect the power-law relation, and we conclude that the population density generated by our model follows

$$D(r) \sim r^{-\alpha} \tag{2.4}$$

for $r^* > r_p^*$. The power-law reasonably well agrees with the empirical results (Lemoy et al., 2020). Since Lemoy et al. (2020) and Lemoy et al. (2017) study profiles across many cities at the same time step and we rescale various realizations but across time (instead of only across samples) we hypothesize ergodicity, in a sense that cross-sectional and temporal behaviour are the same.

As can be seen in Fig. 2.2, the density gradient exponent α depends on the gravity exponent γ. We find

$$\alpha = 2\gamma - 3\,. \tag{2.5}$$

Small γ-values lead to scattered/sprawled structures and large γ-values lead to compact patches. The value $\gamma \simeq 2.5$ as estimated for Paris (Rybski et al., 2013) agrees well with $\alpha \simeq 2$ as indicated in Lemoy et al. (2020).

2.3.1.2 *Urban fraction gradient*

Analogously to the population density, the urban fraction is given by $u(r) = \sum_k \theta(w_k) / \sum_k 1$, where $\theta(w_k) = 0$ for $w_k = 0$ and $\theta(w_k) = 1$

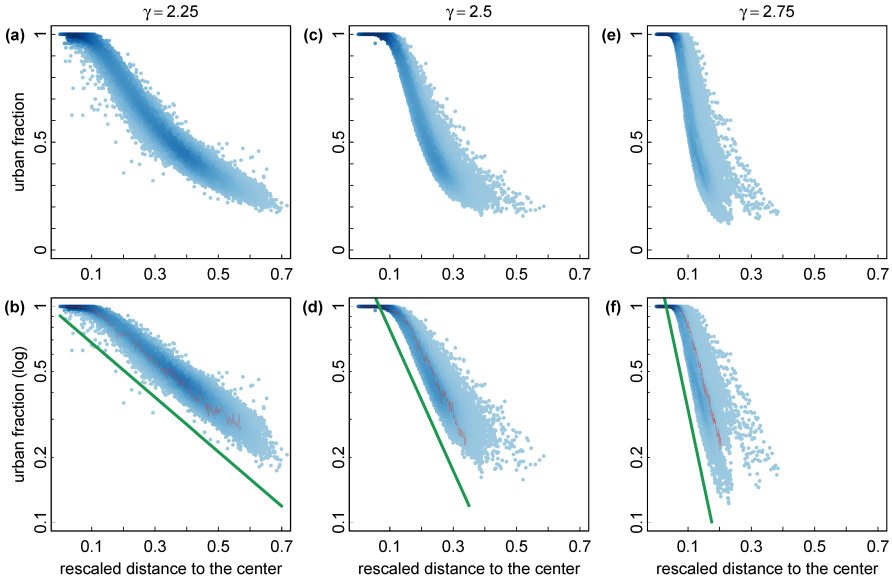

Figure 2.3: Urban fraction gradients. The urban fraction is plotted as a function of the rescaled distance to the centre according to Eq. (2.6), for (a)+(b) $\gamma = 2.25$, (c)+(d) $\gamma = 2.5$, and (e)+(f) $\gamma = 2.75$. Panels (a), (c), (d) are in lin-lin scale and in panels (b), (d), (f) the vertical axis is logarithmic. Due to rescaling the values of all realizations and iterations fall onto each other. The shades of blue represent densities. The red line in (b), (d), and (f) corresponds to the data of an individual curve, and the straight green line is a guide to the eye from Eq. (2.7). The urban fraction decays exponentially.

for $w_k > 0$. Again, as proposed in Lemoy et al. (2020), we rescale the urban fraction according to

$$r^* = \frac{r}{S^{1/2}} \qquad u^*(r) = u(r)\,. \tag{2.6}$$

Similar to the population density, the rescaled curves of urban fraction collapse onto each other in Fig. 2.3. For the urban fraction we find an exponential decay

$$u(r) = \exp\left(-\frac{b}{S^{1/2}} r\right) \tag{2.7}$$

for $r^* > r^*_{\mathrm{p}}$. The urban fraction gradient parameter depends on the gravity exponent, i.e. $b/S^{1/2} \sim \exp(c\,\gamma)$ with $c \approx 10/3$, see Fig. 2.3(b),(d),(f).

Equation (2.7) seems to hold reasonably well (Makse et al., 1995), but overall Lemoy et al. (2020) find a slower than exponential decay.

2.3.2 *Urban fractality*

Next we want to argue that Eq. (2.4) is related to fractality (Batty et al., 1994; Frankhauser, 2008; Encarnação et al., 2012; Zhou et al., 2017). The fractal dimension d is commonly defined by $M \sim L^d$, i.e. by the way

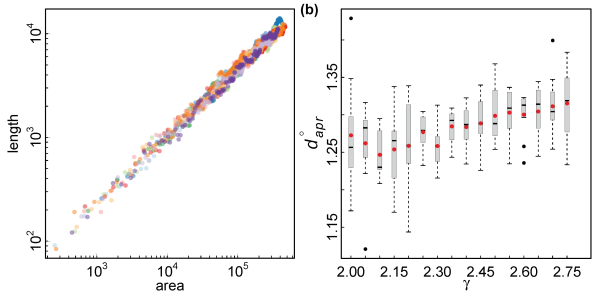

Figure 2.4: Area-perimeter relation. (a) The area and perimeter of the major central cluster are correlated according to a power-law Eq. (2.9), here shown for $\gamma = 2.5$. In the panel all realizations have been combined. (b) Fractal dimension of the perimeter d°_{apr} according to the area-perimeter relation as a function of the gravity exponent γ. The red dots represent the averages among the realizations.

how the mass M of the considered structure changes with linear size L, see Bunde et al., 1995, e.g. In our case the relation between M and L can be expressed as a mass-radius relation (Makse et al., 1998; Daqing et al., 2011). Moreover, we are studying the density $D = M/L^2$. In combination we can write $D(r) \sim r^{d_{\mathrm{rad}}-2}$ (Batty et al., 1994, Eq. (8.12)). Comparison with Eq. (2.4) leads to $\alpha = 2 - d_{\mathrm{rad}}$ and with Eq. (2.5) to

$$d_{\mathrm{rad}} = 5 - 2\gamma\,. \tag{2.8}$$

For $\gamma = 2.5$ the resulting structures are zero-dimensional in terms of fractal geometry, i.e. essentially corresponding to a point. For $\gamma > 2.5$ we obtain negative fractal dimensions, from which we infer that the mass-radius relation is not valid anymore, i.e. radial symmetry is lost.

2.3.2.1 *Area-perimeter relation*

While so far we have studied the resulting w-values of the whole system, from now on we focus on the properties of the major central cluster. To be more specific, here we consider its shape. As introduced by Lovejoy (1982) we first investigate the area-perimeter relation [see also Batty et al., 1994, Ch. 6.2], according to which the area $A_{\cdot}$ and the perimeter C of the object under consideration are related by a power-law

$$C \sim A_{\cdot}^{d^{\circ}_{\mathrm{apr}}/2} \tag{2.9}$$

where d°_{apr} is the fractal dimension of the perimeter. By $A_{\cdot}$ we denote the area of the cluster where we fill any empty cells (holes) within the perimeter, accordingly, $A_{\mathrm{c}} \leq A_{\cdot}$.

Figure 2.4(a) shows an example of the correlations between area and perimeter. As expected there is a power-law relation. We have fitted the exponent in Eq. (2.9) based on the evolution of the major central cluster of each realization separately. In Fig. 2.4(b) the resulting

fractal dimensions of all realizations are plotted as a function of the various γ-values. There is considerable spreading among the realizations but a minor increase of the average values can be observed from $d^{\circ}_{\mathrm{apr}} \approx 1.25 \ldots 1.32$ for $\gamma = 2.1 \ldots 2.75$, respectively. This range is comparable to the range achieved by the Correlated Percolation Model (CPM) (Makse et al., 1998). Any size dependence of d°_{apr} cannot be studied since in this case size variation defines the dimension.

2.3.2.2 *Box-counting dimensions*

Next we employ box-counting to characterize the structure of the major central cluster. The method consists of counting the number of non-overlapping square-shaped boxes necessary to cover an object, see Bunde et al. (1995) and references therein. By varying the size of the box the dimension is quantified via

$$N_{\mathrm{bc}} \sim L^{d} \tag{2.10}$$

where N_{bc} is the number of boxes, L their size, and d the dimension. We assess the cluster as a whole as well as the envelope of the cluster and denote the dimensions $d^{\bullet}_{\mathrm{bc}}$ and d°_{bc}, respectively.

In Fig. 2.5 we plot the resulting fractal dimensions as a function of the size of the major central cluster A_{c}. It can be seen that the fractal dimensions tend to increase with A_{c}, which is qualitatively consistent with empirical findings and previous results (Shen, 2002; Rybski et al., 2013; Zhou et al., 2017). The correlations are non-linear and more pronounced for $d^{\bullet}_{\mathrm{bc}}$, i.e. the fractal dimension of the entire cluster correlates better with the size.

In (Zhou et al., 2017), based on 5,000 clusters of urban land-cover in Europe, the fractal dimension of the envelope roughly varies between 1.3 and 1.5, while for the cluster itself it varies between 1.3 and 1.7. From our simulations we obtain d°_{bc} roughly between 1.1 and 1.4 [Fig. 2.5(a),(b)] and $d^{\bullet}_{\mathrm{bc}}$ roughly between 1.5 and 1.9 [Fig. 2.5(c),(d)]. However, Zhou et al. (2017) also report an anisometry of the clusters which could affect the fractal dimension. The influence of γ is small and can be seen in Fig. 2.5(e) where we plot the fractal dimensions against each other. The smaller $\gamma = 2.25$ leads to slightly larger d°_{bc}. Overall, the dependence on the size is more pronounced than the influence of the gravity exponent γ.

It needs to be noted that while d_{rad} in Eq. (2.8) describes the fractality of the entire cluster, including the population (i.e. the third dimension), d°_{apr} in Eq. (2.9) and d°_{bc} characterize what in the context of the CPM is called percolation front (Makse et al., 1998), i.e. the fuzziness of the envelope [see Fig. 2.5(f)]. The measure $d^{\bullet}_{\mathrm{bc}}$ is a combination of both, but does not consider the third dimension.

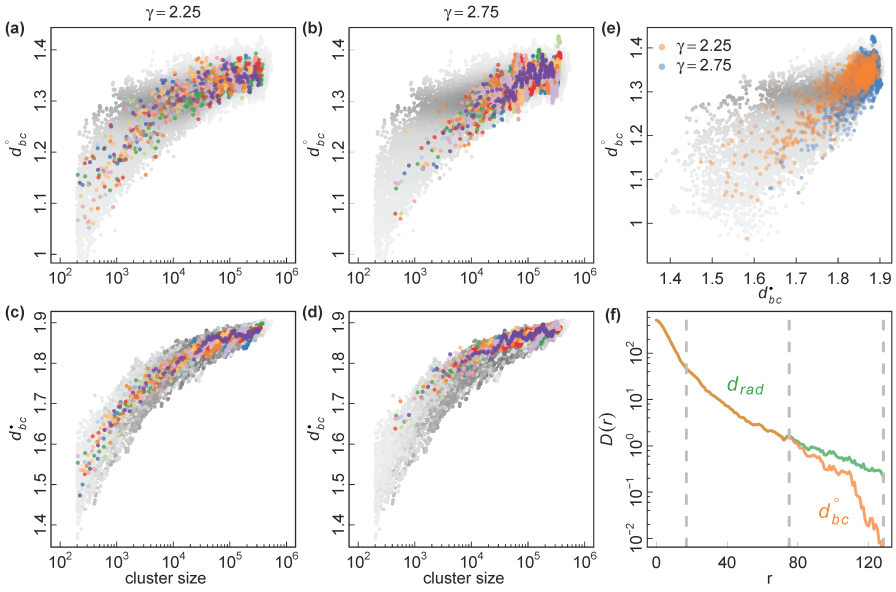

Figure 2.5: Box-counting fractal dimensions of major central cluster and its envelope. The fractal dimensions are plotted vs. cluster size in (a)-(d) for the envelope, d°_{bc}, in (a)+(b), and the entire cluster, $d^{\bullet}_{bc}$, in (c)+(d). As examples, we use (a)+(c) $\gamma = 2.25$ and (b)+(d) $\gamma = 2.75$. The different colours represent the various realizations. The two fractal dimensions are plotted against each other in (e), where it can be seen that the fractal dimension of the envelope is slightly smaller for the larger γ-value. Overall, the influence of the cluster size is stronger than the gravity exponent. Panel (f) illustrates for an example of the population density gradient (semi-log) how the different fractal dimensions are defined by different features of the simulations. The orange curves represent the major central cluster and the green one the entire system, i.e. including small surrounding clusters.

2.3.3 *Fundamental allometry*

Schläpfer et al. (2015) find a power-law between the *average building height and city size*. In our context the building height translates into population density so that their relation corresponds to $S_c/A_c \sim S_c^{\phi}$. This power-law, in turn, is associated with the fundamental allometry relating the population and area of cities (Stewart et al., 1958; Nordbeck, 1971; Batty et al., 2011; Fluschnik et al., 2016; Rybski, 2016; Rybski et al., 2017)

$$S_c \sim A_c^{\delta} \tag{2.11}$$

via $\phi = 1 - 1/\delta$. Accordingly, in the following we analyse Eq. (2.11) for our model, i.e. the major central cluster.

In Fig. 2.6(a) one can see that the resulting populations and areas follow power-laws according to Eq. (2.11). The allometry exponent δ depends on the gravity exponent γ, approximately following a parabolic relationship, see Fig. 2.6(b). Schläpfer et al. (2015) report $\phi \simeq 0.34$ – considering buildings within 2 km from the city centre –

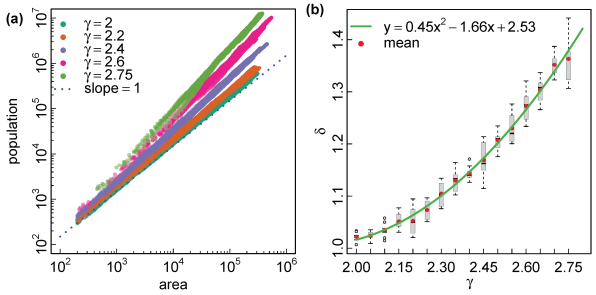

Figure 2.6: Fundamental allometry. The population of the major central cluster as a function of its area is plotted in panel (a) for various γ-values as indicated in the legend. The dotted line has slope 1. Values of all realizations and iterations are shown. The scaling exponent δ according to Eq. (2.11) is plotted in panel (b) together with a parabolic regression. The 10 realizations for each γ-value are represented by a box plot. Larger values of γ lead to increased population density in big cities.

which corresponds to $\delta \simeq 1.52$ and $\gamma \approx 3$ according to our numerical results. Our model seems to be restricted to $\delta > 1$, which is consistent with the results for the majority of real-world cities (Batty et al., 2011; Bettencourt et al., 2016).

2.4 SUMMARY & DISCUSSION

In summary, our simulations show that the gravitational approach – according to which the probability of incremental growth is proportional to $d^{-\gamma}$ – is capable of reproducing radial gradients of real-world cities. We numerically find a relation between the gravity exponent γ and the population density exponent α, suggesting equivalence i.e. the power-law population gradient is an expression of the gravitation (or vice versa). Accordingly, our results confirm the idea of a *friction of distance* (Batty et al., 2011), (Benenson et al., 2004, Sec. 3.2.2). However, the strength of proximity follows a power-law and it can be anticipated that an exponential function instead of $d^{-\gamma}$ in Eq. (2.1) will not lead to rich spatial complexity. If we accept that the model generates structures that resemble real-world cities, then we can conclude that gravitation represents a composite mechanism of the various attractive processes influencing location choices (proximity to friends and work, availability of infrastructure, clustering of business types, etc.).

Our results add to the pioneering work by Batty et al. (1992) who described a power-law population density gradient – in contrast to an exponential one (Clark, 1951). However, the proposed range of α between 0 and 1 corresponds to γ between 1.5 and 2, which is below the range investigated here. For $\gamma < 2$ the emerging structures are too noisy (Rybski et al., 2013) and unrealistic compared with real-world cities. A recently suggested value is $\alpha \simeq 2$ (Lemoy et al., 2017) which corresponds to $\gamma \simeq 2.5$ (Rybski et al., 2013). Interestingly, at this

precise value of $\alpha = 2$ and $\gamma = 2.5$ the fractal dimension is $d_{\text{rad}} = 0$ which agrees with the perception of cities as (zero-dimensional) points. For $\gamma > 2.5$ a transition occurs where the fractal dimension is not defined or does not well-behave which we denote *singularity*.

Moreover, it needs to be mentioned that we study our model results in terms of mono-centric cities. If the main cluster merges with surrounding smaller ones, then sub-centres can appear, but overall the main centre dominates, as illustrated in Fig. 2.1. It remains to be studied what happens in the regime $\gamma > 2.5$. In any case, a coherent definition and an appropriate measure for poly-centrism are lacking.

We investigate additional three fractal dimensions characterizing the structure of the major central cluster, disregarding the population density. Overall we find that the fractality is dominated by the size of the cluster while the gravity exponent γ has a minor influence. This is consistent with various previous papers.

Our approach also leads to urban allometry between population and area, although the scaling seems to be restricted to $\delta > 1$ in Eq. (2.11), i.e. the case where large cities exhibit higher densities. In a sense the exponent γ determines how sprawled or compact the emergent cities are. If one could find a policy instrument to control γ, then one could use it to influence urban development in the desired way. This could address sustainability questions, e.g. related to the ratio of land consumption rate to population growth. Specifically, larger γ-values lead to more compact cities – due to the fundamental allometry Eq. (2.11) this influences mostly the large ones.

An alternative model that elegantly generates spatial complexity and radial gradients is Diffusion-Limited Aggregation (DLA) (Witten Jr. et al., 1981; Fotheringham et al., 1989; Batty et al., 1989; Batty et al., 1994; Batty, 2013). Contrasting Eq. (2.7), DLA leads to a power-law gradient of the urban fraction (Fotheringham et al., 1989, Eq.(3)). A form of allometry, Eq. (2.11), is also obtained from DLA (Fotheringham et al., 1989, Eq.(5)). The fractal dimension of the DLA in its basic form is ≈ 1.71 (Batty et al., 1994, e.g.). However, as the present model also grows in the third dimension, DLA can rather be compared to the binary gravitational model (Rybski et al., 2013).

In contrast to the Correlated Percolation Model (CPM) proposed in (Makse et al., 1995; Makse et al., 1998), where the urban fraction gradient and the structure are introduced artificially, in the gravitational approach presented here they are emergent. Moreover, it is not straightforward to extend the CPM to also simulate population density. It would be interesting to analyse which gradients are generated by the Spatial Network Model (SNM) (Frasco et al., 2014; Wickramasinghe et al., 2018).

The q_j in Eq. (2.1) are often interpreted as the potential of a gravitational force $F_{j,k}$ (Batten et al., 1987). In physics, they are related

via $F = -\nabla q$ and as the distance appears $\sim d^{-\gamma}$ in the potential, it should be $\sim d^{-(\gamma+1)}$ in the force. However, the analogy only works partly. First, the system does not have any dynamics and the kinetic energy as the counterpart to the potential is missing. Second, the q_j are probabilities and more similar to the probability density of finding a particle at a given place, i.e. the squared modulus of a wave function, but it is questionable if a wave function makes sense in this context.

We also would like to discuss some limitations of our gravitational model. (i) The maximum urban fraction reaches 1 which is higher than in real cities. Analogously, the population shows unbounded growth in the core and not a plateau as in real cities (although in Fig. 2.2 a plateau can be seen in the log-log scale, in lin-lin representation it is negligible). (ii) The assumed proportionalities between the w-values, population density, and building height do not affect the model interpretations but for the comparison with real-world cities they represent rough assumptions and might require refinements from follow-up studies (Biljecki et al., 2016). In particular, a central business district and similar features would require to distinguish residential from commercial and other uses. (iii) Real-world cities are rarely radial and many exhibit anisometry (Zhou et al., 2017), which in most cases results from landscape constraints (e.g. coastlines). Our model apparently does not reproduce such anisometry but was also not intended to do so. (iv) The growth is exogenous and the constant growth parameter g leads to idealized urban development trajectories.

In principle the model can be extended by another exponent ϵ, i.e. $w_k^\epsilon d_{j,k}^{-\gamma}$ in Eq. (2.1), giving more or less dense cells more or less weight. For the sake of simplicity we did not follow this approach. Moreover, in the context of complex networks it has been shown that "nonlinear preferential attachment" ($\epsilon \neq 1$) leads to degree distributions which are different from power-laws (Krapivsky et al., 2000). For systems of cities this would imply deviations from Zipf's law.

Last but not least we would like to discuss an outlook for future work. (i) Recently, Volpati et al. (2018) proposed a dispersion index to characterize the degree of localization in populous areas. A direction of future research could be to apply it to our model output and establish a relation. (ii) It could also be of interest to operationalize the gravitational approach in order to apply it to real-world data (Jones et al., 2016). More landscape features need to be taken into account for realistic modelling. (iii) The described gradients could be related to other quantities, such as the urban heat island (UHI) effect (Watkins et al., 2002, Fig. 6), (Zhou et al., 2017).

3

INFLUENCE OF URBAN DENSITY AND MORPHOLOGY ON CUHI[1]

ABSTRACT

The canopy layer urban heat island (CUHI) effect, as manifested by elevated near-surface air temperatures in urban areas, exposes urban dwellers to additional heat stress in many cities, specially during heat waves. We simulate the urban climate of various generated cities under the same weather conditions. For mono-centric cities, we propose a linear combination of logarithmic city area and logarithmic gross building volume, which also captures the influence of building density. By studying various city shapes, we generalize and propose a reduced form to estimate CUHI intensities based only on the structure of urban sites as well as their relative distances. We conclude that in addition to the size, the CUHI intensity of a city is directly related to the density and an amplifying effect that urban sites have on each other. Our approach can serve as a CUHI rule of thumb for the comparison of urban development scenarios.

KEYWORDS:

Canopy layer urban heat island, urban area, building, density, urban morphology

1 This chapter is based on the published paper: Y. Li et al. (2020c). "On the influence of density and morphology on the Urban Heat Island intensity." *Nat. Commun.* 11.1, pp. 1–9. DOI: 10.1038/s41467-020-16461-9, Copyright © 2020, The Author(s).

3.1 INTRODUCTION

The canopy layer urban heat island (UHI) effect, a phenomenon manifested by elevated near-surface air temperatures in cities compared with their non-urban surroundings, is mainly due to land surface modification in connection with urbanization. The surface energy balance of urban areas differs from that of vegetated land in various aspects. First, as impervious surfaces replace the natural land cover of low albedo, high thermal capacity, and high thermal conductivity, urban areas exhibit reduced latent heat flux and increased heat absorption (Oke et al., 2017). Second, the geometry of urban surfaces featuring buildings and street canyons leads to reduced overall wind ventilation as a consequence of increased roughness, and to more radiation trapping due to in-canyon reflections (Chapman et al., 2017; Oke, 1982). Anthropogenic heat release from human activities also adds to the accumulation of heat. The combined effect of these properties causes the UHI phenomenon. Usually, the canopy layer UHI (CUHI) intensity peaks at night (Oke, 1981) as heat stored in the urban surfaces during daytime is released (Zhao et al., 2014) resulting in a lower cooling rate compared with vegetated surfaces.

The UHI effect has various direct and indirect impacts on urban dwellers and their health (Grimm et al., 2008; Patz et al., 2005; Eliasson, 2000). In many cities, it exposes urban dwellers to extra heat stress and thus leads to thermal discomfort as well as heat-related health problems during hot summer days (Tan et al., 2010; Cao et al., 2018). In particular during heat wave events, the risk of heat morbidity and mortality increases (Tan et al., 2010; Zhao et al., 2018; Habeeb et al., 2015; Gabriel et al., 2011) as the UHI effect interacts with heat waves by prolonging and intensifying hot conditions (Schatz et al., 2015; Zhao et al., 2018; Li et al., 2013a). Warming enhanced by urbanization has been identified in many cities and regions (Cao et al., 2018; Kalnay et al., 2003; Argüeso et al., 2014; Georgescu et al., 2013), which implies more severe heat stress in the future.

The impacts are further exacerbated when taking climate change into consideration (Chapman et al., 2017; Zhao et al., 2018; Heaviside et al., 2017), though they interact non-linearly and are found to produce warming that is less than the simple sum of their individual contributions (Krayenhoff et al., 2018). Apart from health risks, the joint economic costs of urban impacts from the UHI effect and climate change have been estimated to be 2.6 times those without the UHI effect (Estrada et al., 2017). Although UHIs do not remain stable under climate change (Chapman et al., 2017; Grossman-Clarke et al., 2017) or urban development (Krayenhoff et al., 2018), future strong nocturnal warming due to urban effects has been found in many cities (Zhao et al., 2018; Krayenhoff et al., 2018; Schatz et al., 2015; Cao et al., 2018; Georgescu et al., 2013). This may not be too critical under normal

temperature conditions. However, during heat waves this aggravated heat stress can create significant risks to urban residents as mortality risk is found to be significantly associated with minimum temperatures (Laaidi et al., 2012; Kalkstein et al., 1989). Therefore, measures to reduce the impact of UHI will also contribute to urban heat stress mitigation, especially in the future with more frequent and stronger extreme heat events due to the interactions between urban climate, heat waves, climate change, and urbanization.

Many studies on the neighbourhood or block scale have related higher temperature to urban characteristics such as impervious surface fraction (or its opposite, nature surface fraction), building density (Gabriel et al., 2011), and street canyon aspect ratio (Marciotto et al., 2010; Oke, 1981). Some researchers have also tried to quantify the neighbourhood scale UHI intensity based on this knowledge (Van Hove et al., 2015; Li et al., 2019b). Those findings not only help to advance our understanding of the physical mechanism behind the UHI formation, but also shed light on useful measures to alleviate heat stress in hot spots, or to generally create a better thermal environment. Benefits of some local interventions like increasing vegetation space (Schubert et al., 2013), green roofs (Straka et al., 2019), and cool coating of buildings and infrastructure (Ng, 2012) have been proven by both numerical studies and practical applications.

However, such mitigation strategies have very local influences on climate (Zhou et al., 2017) and may not always work as efficiently at night as during hot afternoons (Krayenhoff et al., 2018). Besides, many aspects of urban form (such as overall dimensions, skyline and polycentricity, sprawling and compactness) (Oke et al., 2017) can affect the spatial pattern of urban climates (Zhou et al., 2018; Zhou et al., 2017). This suggests the potential of urban form and structure to mitigate urban heat stress. For example, urban characteristics measured by a sprawling index were found to be strongly related to the growth rate of extreme heat event frequency (Stone et al., 2010). Thus, rapid urban growth poses challenges to urban heat mitigation, but it also presents an important opportunity to implement urban climate knowledge in newly developing areas. A quantitative assessment is needed to support urban decision-making that takes the UHI effect into account. In this work, we quantify the relationship between canopy layer urban heat island (CUHI) and the urban form, namely the three-dimensional configuration of urban elements. With this, urban growth can be developed in a way that does not create a strong CUHI effect in the first place instead of reducing the urban heat after expanding. As the CUHI effect has the greatest impact during heat waves and usually reaches its maximum at nighttime, we focus on these conditions.

Here we simulate the urban climate of hypothetical cities with variable size, density, and compactness/sprawling. To this end, we use the surface and vegetation characteristics of the region around

Berlin (Germany), replace the city with generated clusters, run the urban climate model driven by the same lateral climate conditions, and extract the CUHI intensity. By repeating the procedure for different mono-centric clusters we infer an expression for the CUHI intensity that is solely based on the area and the gross building volume. By studying a wider range of city shapes, we generalize and propose a reduced form to estimate CUHI intensities based only on the structure of urban sites as well as their relative distance. We conclude that in addition to the size, the CUHI intensity of a city is directly related to the building density and an amplifying effect that urban sites have on each other.

3.2 METHODS

3.2.1 *Climate model and urban canyon scheme*

The mesoscale non-hydrostatic climate model CCLM (Steppeler et al., 2003) coupled with a multi-layer urban canopy model (UCM), the Double Canyon Effect Parametrization (DCEP) Scheme (Schubert et al., 2012), was used in this study. Previous work has shown that diurnal variation and magnitude of CUHI can be well represented in CCLM/DCEP during summer months (Schubert et al., 2014; Schubert et al., 2013).

CCLM was developed from the operational weather forecast Local Model (LM) of the German Meteorological Service by the CLM-Community and has been the community model of German climate research since 2005. In the standard CCLM, cities are represented by a bulk-transfer scheme with modified soil and vegetation parameters. An urban scheme is necessary to represent important urban characteristics in terms of thermal properties and vertical effects of buildings (Schubert et al., 2013). The DCEP scheme, based on the Building Effect Parametrization (Martilli et al., 2002) (BEP), accounts for the effects of buildings and streets configuration on the atmosphere. When coupled with CCLM, DCEP is only applied to the urban fraction of a mesoscale model grid cell, the remaining natural surface fraction is treated by the land surface scheme of CCLM. In DCEP, the urban surface is conceptualized as multiple series of identical street canyon elements which are characterized by canyon direction, street width, building height, and building width. Therefore, urban canopy parameters (UCP) required by DCEP for each urban grid cell are: urban surface fraction, canyon direction distribution, building height distribution, street width, and building width.

3.2.2 *Simulation setup and data analysis*

We conducted a chain of 3 nested CCLM simulations with resolutions of 0.165°, 0.025°, 0.009°, see coverage of each model domain in Appendix B, Fig. B.6b. The domain of the innermost simulation was centred at Berlin. A period of one week during a heat wave event was simulated (Schubert et al., 2013). The coarsest simulation was driven by ERA-Interim reanalysis data with a spin-up time of 5 years. The remaining two nesting steps started 6 months and 12 days, respectively, before the analysed period.

The DCEP scheme is only applied in the finest simulations. To validate our model configuration we conducted a reference run with UCP data derived from a 3D dataset of Berlin at 1 km resolution (Schubert et al., 2013). Statistics of the model performance against observational data (measured at 6 weather stations located in and near Berlin, see Appendix B, Fig B.6b) are shown in Appendix B, Table B.1. In terms of mean error (ME), mean absolute error (MAE), and root mean-square error (RMSE), the model satisfactorily reproduces the 2 m air temperature.

Configurations for the simulations with generated UCP data were the same with the reference run except that the external data such as vegetation, orography and soil parameters were made homogeneous based on the mean value of the finest domain. This minimizes the effect of non-urban parameters on our results.

For each generated urban cluster we define a non-urban boundary of approximately the same area by determining several layers of cells surrounding the urban area (Zhou et al., 2013). The difference between average 2 m air temperatures of the urban area and rural boundary area was taken as the CUHI intensity.

3.2.3 *Stochastic gravitational urban growth model*

We used a stochastic gravitational urban growth model (Li et al., 2021a) to create realistic 3D urban canopy data. This model, based on the concept that growth is more likely to take place close to high densities, is capable of reproducing various attributes of real-world cities, such as the radial gradients of population density, radial gradients of urban fraction, and the power-law between the population and city area. On a square grid, the probability of growth in cell i is given by $p_i = \frac{G}{M_i} \sum_{j \neq i} v_j d_{i,j}^{-\gamma}$, where γ is the main parameter, $d_{i,j}$ is the Euclidean distance from cell i to j, v_j is the value in cell j, M_i is a site-specific normalization constant (Li et al., 2021a; Rybski et al., 2013), and G is another parameter determining the overall rate of growth. Starting with a single $v = 1$ cell in the centre, the model is run iteratively incrementing the counts $v_i \to v_i + 1$, if $z < p_i$, where z is a random number between 0 and 1. The exponent γ controls the shape of the

emerging urban clusters, i.e. small γ lead to sprawled and radial symmetric structures and large γ lead to compact forms with less radial symmetry. Consistent with Li et al. (2021a) we explored $\gamma \in \{2.0, 2.05, \ldots, 2.7, 2.75\}$ and 1000×1000 system size.

From the resulting 141758 clusters, for each γ value we first select one cluster with an area of approximately 2000 cells (as we put these clusters in the climate model domain with 1km^2 resolution, its area corresponds to 2000km^2). The corresponding gross building volume increases with γ. We name these clusters set 1 and took the cluster for $\gamma = 2.5$ in set 1 as reference cluster C_{ref}. Similarly, we select one cluster for each γ value which has approximately the same gross building value as C_{ref}. The corresponding cluster areas decrease with γ. We name these clusters set 2. At last, another 9 clusters emerging from the same growth sequence (realization) as C_{ref} are selected. Together with C_{ref}, they make up set 3. In addition, 10 clusters from different γ values are selected according to the criterion that they are close to C_{ref} in terms of gross building volume and size. They constitute set 4. See Appendix B, Fig. B.1 for the cross plot of size versus gross building volume of all selected clusters and some of them depicted.

3.2.4 *3D urban canopy parameter (UCP) data*

In order to make use of the gravitational urban growth model output, the grid value v_i in pixel i was taken as the floor count of the building in this pixel. The system was aggregated into to a coarser domain of 200×200, thus each coarse pixel consists of 25 finer pixels with values $\{v_1, v_2, ..., v_{25}\}$. Then the urban fraction f_{u} of this coarse pixel was calculated as $\frac{N(v_i>0)}{25}$, where $N(\cdot)$ is a function that counts the number of considered values that match the criterion of it. Only coarse pixels with urban fraction no less than 20% were taken as urban cells (Stewart et al., 2012), in the end, we got a 200×200 urban/non-urban matrix for each output. For some outputs from large γ values, the v values of pixels near the centre become very large after many iterations. In order to have more realistic city centres, we applied a threshold of 30 for the maximum average number of building storeys on each coarse pixel and rescaled the building height distribution as follows. If $\bar{v} = \frac{\sum v_i}{N(v_i>0)} > 30$, $v_i = \frac{30 v_i}{\bar{v}}$, thus the average building height $\bar{v}$ for all coarse pixels will not exceed 30 storeys. Then for each coarse pixel marked as an urban cell, we calculated the building height distribution $\{f_{\text{h}1}, f_{\text{h}2}, ..., f_{\text{h}j}\}$ following $f_{\text{h}i} = \frac{N(v_i=i)}{N(v_i>0)}$, where $f_{\text{h}i}$ denotes the share of buildings with a height of i storeys, j is the maximum value of the original 1000×1000 lattice.

We applied the City Clustering Algorithm (CCA) algorithm (Rozenfeld et al., 2008) on the aggregated urban/non-urban matrix to assign all urban pixels into clusters. In this study, we only focus on the central, the largest cluster of each output. In addition, only the central

clusters with more than 200 pixels which do not touch any edge of the coarse domain were considered.

For each coarser grid cell, the proportion of urban surface occupied by building footprints was calculated (Schubert et al., 2013) as $f_b = \frac{W_b}{Y+W_b}$, where W_b and Y are building width and street width, respectively. The building volume w for each grid was calculated according to

$$w = A_{grd} \times f_u \times f_b \times \bar{v} \times H_f\,, \tag{3.1}$$

where A_{grd} is the area of the grid cell (1×1 km^2 throughout all the simulations), f_u is urban fraction measured as urban surface fraction, $\bar{v}$ is the aforementioned average building height measured by the number of storeys, and H_f is the floor height (we assume constant floor height of 3 m for all buildings to further simplify conditions in this study), see the notation in Appendix B, Table B.3. We take the number of pixels of the considered cluster as the urban size A, and the sum of the building volume covered by the cluster as the gross building volume, namely $S = \sum w_i$.

For other parameters required by the DCEP scheme, such as street direction distribution, street width and building width (Schubert et al., 2013), we first assumed they are distributed homogeneously within the urban area in order not to introduce further variability. The fraction for each direction ($-45°$, $0°$, $45°$, $90°$ to the north clockwise) in each pixel is 25%. For street width Y and building width W_b, 20 m and 15 m are taken, respectively. Based on the selected clusters, 50 urban canopy parameters (UCP) datasets are created.

We create additional 42 UCP datasets that feature 10 spatial patterns (see Appendix B, Fig. B.3 and Table B.2 for examples of each pattern), which are named set 5. For these clusters, we chose a street canyon width of 15 m and a building width of 20 m. We take a different street canyon width compared with sets 1-4 since in set 5 some clusters are rather small and as smaller canyon width leads to stronger CUHI intensities, we have a better signal-to-noise ratio.

To study how the street canyon width influences the parameters a_1, a_2, a_3 in Eq. (3.2), we pick 5 UCP datasets from set 1 and another 5 from set 3 to create additional UCP data. Based on each of these UCP datasets, we then create 4 new UCP datasets by only changing the street canyon width to 10 m, 15 m, 25 m and 30 m, respectively, and changing the building width accordingly to keep the fraction of building plan area unchanged. Then for each street width in $\{10, 15, 20, 25, 30\}$ m, we get 10 simulations and fit the results with Eq. (3.2). Comparing the resulted a_1, a_2, a_3, we are able to study the influence of the street width. These modified UCP datasets are together named set 6.

The Parameters taken for different UCP datasets can be found in Appendix B, Table B.4.

3.2.5 *UCP data from different urbanization scenarios of Berlin*

To illustrate how our findings can be used for real-world cities, we create a series of urban canopy parameters (UCP) data based on different hypothetical urbanization scenarios for Berlin. This is done by modifying the real UCP data taken for the reference run. Assuming that the change of living space only happens in the vertical direction, we increased (or decreased) the average building height proportionally by -50 %, -25 %, +25 %, +50 %, +100 %. Thus, we get 5 UCP scenarios with a gross building volume increment of -50%, -25%, 25%, 50%, 100% relative to the real UCP data.

Similarly, we can also allocate the change by altering the urban fraction. For the scenarios of decreasing gross building volume by 50% and 25%, we simply decrease the urban fraction of each grid cell by 50% and 25%. However, for increasing gross building volume scenarios, we decrease the vegetation surface of each grid cell by the same percentages to get 3 scenarios with gross building volume increased by 25%, 50%, 100%. A similar method has been used by Schubert et al. (2013).

It has to be noted that both vertical changes and horizontal changes are constrained within already urbanized grid cells, that is, without changing the shape of the urban cluster. In the third scenario, the change in gross building volume is achieved by modifying the extent of the urban cluster. This is implemented by randomly adding or removing urban grid cells. For decreased gross building volume scenarios, we simply repeated the process of randomly removing an urban grid cell from the edge of the cluster. For increased gross building scenarios, the following steps are repeated until the gross building volume of the expanded urban cluster approximately agrees with the desired size. Step 1: randomly pick a grid cell from the urban cluster; Step 2: randomly select a non-urban grid cell which is adjacent to an urban grid cell; Step 3: replace this non-urban cell with the urban cell selected by step 1. At the end, we get 10 scenario UCP datasets with gross building volume changed by -50%, -25%, -10%, +10%, +25%, +40%, +50%, +60%, +75%, 100% respectively,

3.3 RESULTS

3.3.1 *Modelling setup and CUHI definition*

We start by generating urban clusters resembling real-world cities and define the urban canopy parameters (UCP) accordingly. Then we use the physical characteristics of the region around Berlin to simulate the urban climate employing the CCLM/DCEP urban climate model (Schubert et al., 2012), always driven by the same lateral climate conditions (see Methods) An example urban cluster and its building

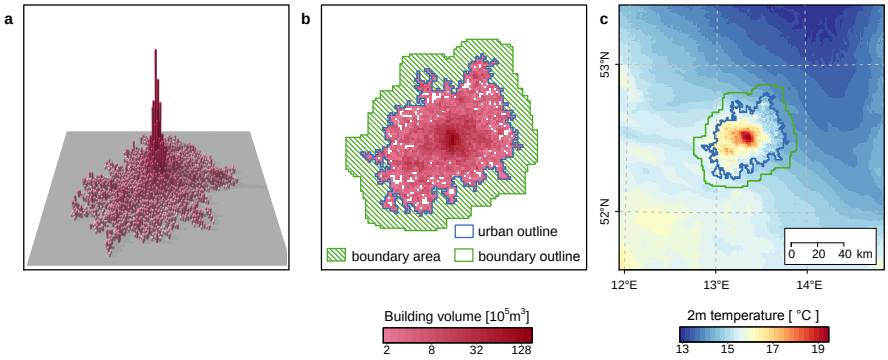

Figure 3.1: Example of generated urban clusters and resulting heat patterns. **a**, 3-dimensional illustration of average building height in each grid cell of a considered cluster. **b**, Gross building volume in the cluster together with cluster edge and surrounding boundary. **c**, Simulated temperature field at night (02:00 local time). The canopy layer urban heat island (CUHI) intensity is defined as $\Delta T_a = \langle T_{a,C} \rangle - \langle T_{a,B} \rangle$, where $\langle T_{a,C} \rangle$ and $\langle T_{a,B} \rangle$ are the average 2 m air temperatures in the city (blue line) and boundary (green line), respectively.

information are illustrated in Fig. 3.1a. With each configuration we simulate the 2 m air temperature in the period of August 1st-7th, 2003, i.e. during a heat wave characterized by predominately clear skies and light winds (Schubert et al., 2013). In order to analyse the overall urban heat island intensity of the city, we consider the urban cluster and a non-urban belt with an approximately equal area (Fig. 3.1b), as used for remote sensing data (Peng et al., 2012; Zhou et al., 2013). Then we define the hourly canopy layer urban heat island (CUHI) intensity $\Delta T_{a,i}$ as the difference between the average 2 m air temperatures in both areas, i.e. $T_{a,i} = \langle T_{a,C_i} \rangle - \langle T_{a,B_i} \rangle$, where $\langle T_{a,C_i} \rangle$ and $\langle T_{a,B_i} \rangle$ are the average temperatures at local time i in the cluster and the boundary, respectively (see Fig. 3.1c). We extract the daily maximum CUHI magnitude, and average it over 7 days for each simulation. For simplicity, CUHI intensity and ΔT_a henceforth refer to the 7-day-average maximum CUHI magnitude based on 2 m air temperature difference, unless otherwise indicated. A more general discussion of the UHI intensity and shortcomings of how to measure it can be found in previous studies (Oke, 2006; Stewart et al., 2006). Finally, we build models expressing ΔT_a as a function of building parameters.

3.3.2 *Simulations with mono-centric urban clusters*

We repeat the analysis for 50 clusters (generated by a gravitational urban growth model (Li et al., 2021a; Rybski et al., 2013), see Methods) which vary by size and compactness. In Appendix B, Fig. B.1 we provide details on the clusters. The clusters are characterized by their size A (km^2), which is given by the number of urban cells, and by the gross building volume S (km^3), which is given by the sum of building

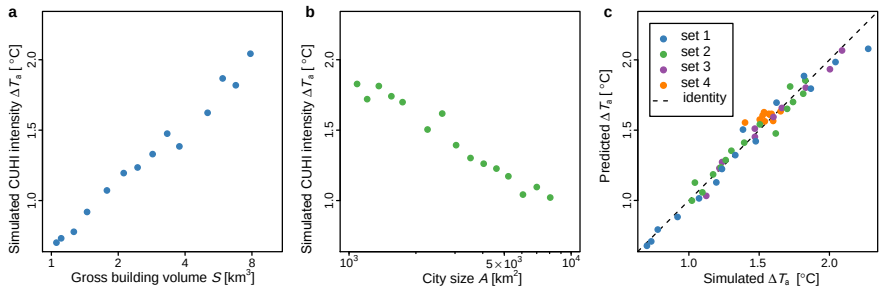

Figure 3.2: Canopy layer urban heat island (CUHI) intensity ΔT_a as a function of city characteristics and fitting performance of Eq. (3.2). **a**, the CUHI intensity is plotted vs. gross building volume for constant city size. **b**, the CUHI intensity is plotted vs. city size for constant gross building volume. **c**, predicted and simulated CUHI intensities are plotted against each other. Appendix B, Fig. B.1 illustrates the various sets of generated clusters.

volumes w_i over all urban cells i (for calculation of w_i, see Methods). Assuming constant floor height and constant floor area per person, S is proportional to the population size of the entire city. If we keep the cluster size constant, we can study how the CUHI intensity depends on the gross building volume. As shown in Fig. 3.2a, ΔT_a increases approximately linearly with $\ln S$. Analogously, we can keep the gross building volume constant and test how the CUHI intensity depends on the cluster size (Fig. 3.2b). In this case, ΔT_a decreases approximately linearly with $\ln A$. It is plausible that given the same urban area, cities with higher density exhibit more pronounced CUHI intensities and less dense cities exhibit reduced CUHI intensities (Chapman et al., 2017; Straka et al., 2019).

Combining both results, we find that the CUHI intensity can be described by

$$\Delta T_a = a_1 \ln A + a_2 \ln S + a_3 \,, \tag{3.2}$$

where a_1, a_2, a_3 are parameters. When fitting this form to all 50 investigated clusters we obtain $a_1 = -0.43\,\mathrm{K}$, $a_2 = 0.65\,\mathrm{K}$, $a_3 = 3.90\,\mathrm{K}$ and $R^2 = 0.96$. In Fig. 3.2c we plot predicted and simulated CUHI intensities against each other. From these results we conclude that the CUHI intensity can be described by a linear combination of the logarithmic city area and logarithmic gross building volume (resembling city population), which is a generalization of previous findings (Oke, 1973; Zhou et al., 2013; Zhao et al., 2014; Li et al., 2017; Zhou et al., 2017; Manoli et al., 2019). If we introduce the urban density (Chapman et al., 2017; Oke et al., 2017) and define it as S/A, then we can rewrite Eq. (3.2), $\Delta T_a = (a_1 + a_2) \ln A + a_2 \ln(S/A) + a_3$ or $\Delta T_a = -a_1 \ln(S/A) + (a_1 + a_2) \ln S + a_3$, showing that the CUHI intensity increases linearly with the logarithm of the density (given $a_1 < 0$ and $a_2 > 0$). Moreover, in Appendix B, Fig. B.2 we show that according to the simulations the parameters a_i approach 0 with growing street canyon width. Certainly, the parameters a_i also depend on

additional factors, in particular the background climate (Zhao et al., 2014; Oke, 1973; Oke, 1987) (such as wind speed, precipitation, and cloud cover) and thermal properties of the rural surface (Chapman et al., 2017; Oke, 1987; Runnalls et al., 2000).

3.3.3 *Simulations with a wide range of urban forms*

One can easily think of configurations where A and S are unchanged, but the urban form is very different. The investigated urban clusters do exhibit a range of compact or scattered shapes (Appendix B, Fig. B.1), but more complex spatial features, e.g. as captured by the fractal dimension (Batty et al., 1994; Zhou et al., 2017), can hardly be analysed based on those clusters since their fractal dimension covers a comparably small range (Li et al., 2021a). Accordingly, we perform further simulations with more extreme urban forms that are beyond real-world cities. We generate 10 different spatial patterns with a range of sizes and repeat the urban climate simulations. In order to avoid additional complexity, here we use constant building height and canyon width throughout the urban sites and simulations. The shapes considered range from the rather sparse Cantor Dust to the more compact Sierpinski Carpet. In addition to these regular fractals, the patterns also include irregular ones, e.g. Diffusion-Limited Aggregation (DLA) (Witten Jr. et al., 1981; Fotheringham et al., 1989; Batty et al., 1994) clusters, and non-fractal shapes such as the filled circle (Appendix B, Fig. B.3 and Table B.4).

As the density here held constant, i.e. $A \sim S$, it is sufficient to plot ΔT_a as a function of the area A if we want to apply Eq. (3.2). The results are shown in Fig. 3.3, demonstrating that overall, the CUHI intensity tends to increase with the logarithmic size, but that for a given size, the resulting ΔT_a-values spread over a wide range which is certainly due to the variety of shapes that have been used. Although fractal geometry represents a convenient formalism to characterize spatial structures, we found that the fractal dimension is not a sufficient indicator to describe the CUHI intensities, and we propose an alternative ansatz as follows. Motivated by the perception that any urban site has a heating influence on other urban cells that declines with the distance between the urban cells, we explore the following educated guess combining a size term and a form term

$$\Delta T_\mathrm{a} = b_1 \ln A + b_2 \frac{1}{N} \sum_{j}^{N} \sum_{i \neq j}^{N} d_{ij}^{-\delta} + b_3 \quad \text{with} \quad \delta \simeq 3/2\,, \tag{3.3}$$

where d_{ij} is the Euclidean distance (km) between the urban sites i and j, N is the total number of urban cells, and b_1, b_2, b_3 are parameters. If h_{ij} is the heat influence that site i has on j, then $H_j = \sum_i h_{ij}$ is the influence that site j receives from all other sites. Since for ΔT_a we calculate the average over all the cells of a city, we need an additional sum over all sites and a division by their number, i.e. $\frac{1}{N} \sum_j H_j$, which

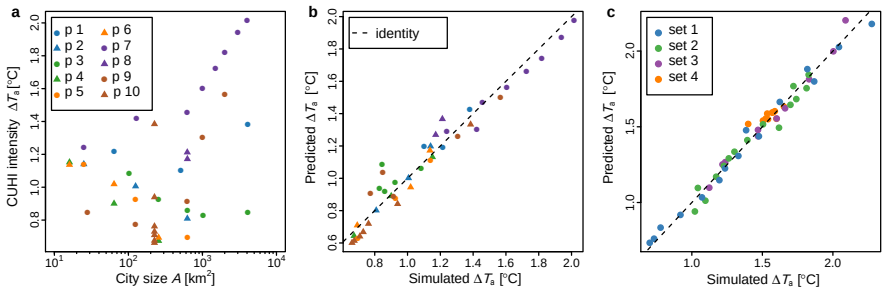

Figure 3.3: Canopy layer urban heat island (CUHI) intensity as a function of city size and form attributes. **a**, the CUHI intensity is plotted against the city size of corresponding spatial patterns (Appendix B, Fig. B.3 and Table B.4). **b**, the CUHI intensity predicted by Eq. (3.3) is plotted against simulated CUHI intensity. **c**, for the realistic urban clusters (Appendix B, Fig. B.1) the CUHI intensity predicted by Eq. (3.4) is plotted against simulated CUHI intensity.

with $h_{ij} \sim d_{ij}^{-\delta}$ corresponds to the second term in Eq. (3.3). When fitting Eq. (3.3) to all 10 patterns (42 simulations) we obtain $b_1 = -0.19\,\mathrm{K}$, $b_2 = 0.04\,\mathrm{K\,km}^{3/2}$, $b_3 = 1.60\,\mathrm{K}$ and $R^2 = 0.95$. The performance is visualized in Fig. 3.3b where predicted and simulated CUHI intensities are plotted against each other. In the Appendix B, Fig. B.4 we show how we found the value of the exponent δ based on the simulations of pattern 10 (Appendix B, Fig. B.3), i.e. a square of constant N but with varying space between the urban pixels. Equation (3.3) suggests that the distribution of distances between the urban sites contains the information necessary to capture the CUHI intensity of basically any urban shape.

3.3.4 *General regression model*

A naturally emerging question is if Eq. (3.3) can also be used to estimate the CUHI intensity of the generated urban clusters which led to Eq. (3.2). In order to unify both approaches, we introduce a weighting factor $f(f_{\mathrm{u}i}, w_i, Y_i)$ into the second term of Eq. (3.3), i.e. as a function of the building volume w_i, the urban fraction $f_{\mathrm{u}i}$, and the street canyon width Y_i for each urban cell. We find reasonable fitting for $f(f_{\mathrm{u}i}, w_i, Y_i) \sim \left(\frac{f_{\mathrm{u}i} w_i}{Y_i}\right)^{1/2}$. Moreover, we have to include the $\ln S$ term as in Eq. (3.2). Thus, in general,

$$\begin{aligned} &\Delta T_\mathrm{a} = c_1 \ln A + c_2 \ln S + c_3 D + c_4 \\ &\text{with:} \\ &D = \frac{1}{N} \sum_j^N \sum_{i \neq j}^N \left(\frac{f_{\mathrm{u}i} w_i}{Y_i}\right)^{1/2} d_{ij}^{-3/2}, \end{aligned} \tag{3.4}$$

where c_1, c_2, c_3, c_4 are parameters. Fitting leads to $c_1 = -0.26\,\mathrm{K}$, $c_2 = 0.28\,\mathrm{K}$, $c_3 = 0.07\,\mathrm{K\,km}^{1/2}$, $c_4 = 2.43\,\mathrm{K}$ and $R^2 = 0.99$. In Fig. 3.3c

we again plot predicted and simulated values against each other and find similar agreement as in Fig. 3.2c, despite the more general approach. We would like to note that we also obtain decent fitting if we employ $f(f_{u_i}, w_i, Y_i) \sim \ln\left(\frac{f_{u_i} w_i}{Y_i} + 1\right)$, as the forms of power-laws with small exponents and of the logarithmic function are quite similar. We find that regressing $\Delta T_a = c_1 \ln A + c_2 D + c_3$, i.e. without the $\ln S$ term, also provides reasonable fitting but Eq. (3.4) is preferable according to the Akaike Information Criterion (AIC) (Wagenmakers et al., 2004). Moreover, Eq. (3.4) can be rewritten into another form which includes urban street canyon aspect ratio (Marciotto et al., 2010; Ali-Toudert et al., 2006) (see Appendix B, Note B.1). Overall, Eq. (3.4) represents a comparatively simple way to estimate the CUHI intensities based on urban form and size. Given that the parameters c_i are known, all that is necessary to estimate the CUHI intensity is the spatial information of urban sites and building heights.

3.3.5 *Application to a real-world example*

Here we briefly illustrate how the above findings can be applied to idealized urbanization scenarios of the (real) city of Berlin. We restrict the simulations to urban development that takes place vertically (decrease/increase in building height), horizontally (shrinking/expanding the extent of the urban cluster), or that decreases/increases the urban fraction. For each of these three urbanization types, we have created several configurations with changes in gross building volume varying between -50% and +100% compared to the present urban canopy data of Berlin (see "Methods" section). The parametrization is then used both to run the urban climate model and to calculate the quantity D in Eq. (3.4). Of course, in addition to urban structure factors, weather conditions (e.g. cloud cover and type, wind speed and direction) and rural surface conditions (such as thermal admittance and surface wetness) are very important factors influencing the CUHI intensity (Runnalls et al., 2000). Together with the reference run (the simulation with real urban canopy data for Berlin that was used to validate the configuration of the climate model, see "Methods" section), we performed 21 simulations.

The simulated CUHI intensities from these scenarios are plotted against the change in gross building volume in Fig. 3.4a. We find that the increases in building height and urban fraction both lead to increases in CUHI intensity, yet they behave differently, as the latter leads to a faster CUHI intensity increase. This is probably due to the stronger shadow effects from taller buildings, which reduce heat storage during the day. For the scenarios with changed urban cluster size, the trends are less clear. The fluctuations may be caused by the fact that the randomly removed or added urban cells vary in urban surface fraction, building structure, and street canyon configurations.

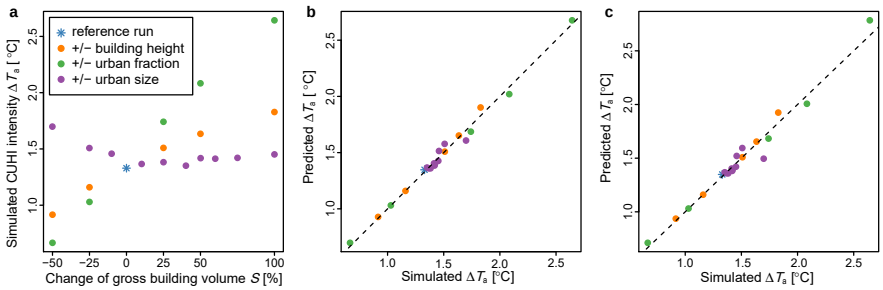

Figure 3.4: Canopy layer urban heat island (CUHI) intensity from urbanization scenarios of Berlin. **a**, the CUHI intensity is plotted against the gross building volume S for corresponding urbanization scenarios. **b**, the CUHI intensity predicted by Eq. (3.4) is plotted against simulated CUHI intensity. **c**, as panel **b** but with out-of-sample validation, i.e. the value to be validated is removed from the sample and the regression is based on the remaining ones (repeated for each value).

In addition, the background climate and rural surface characteristics are heterogeneous throughout the domain, so that different expansion directions of the urban cluster will have slightly different influences on the resulting CUHI intensity. The higher than reference run CUHI intensity of the scenarios with decreased urban cluster size can be understood, when considering that outer cells normally exhibit lower urban surface fraction and building height. When these cells are removed, the remaining central urban core has relatively high building density, leading to higher CUHI intensity.

When regressing Eq. (3.4) on the urban climate results from these scenarios, we obtain $c_1 = -0.25\,\mathrm{K}$, $c_2 = 0.13\,\mathrm{K}$, $c_3 = 0.18\,\mathrm{K km}^{1/2}$, $c_4 = 1.85\,\mathrm{K}$ and $R^2 = 0.99$. As for these simulations, we use heterogeneous real-world external data (such as vegetation, orography and soil parameters, etc.) instead of homogeneous external data for simulations with model-generated mono-centric urban structures, the coefficients here differ slightly from before. The predicted and simulated values are plotted against each other in Fig. 3.4b. Considering the high heterogeneity of the urban structure factors within the real urban canopy parameters (UCP) data and the derived scenario UCP data, we can conclude that our general regression form as in Eq. (3.4) holds not only for model-created urban structures but also for real-world urban structures. In order to test the robustness of these results, we last perform an out-of-sample validation: we remove one simulation from the 21 samples, regress Eq. (3.4), and obtain a prediction which is independent of its corresponding simulated value. Then we repeat the procedure for each sample in the set (leave-one-out cross-validation). Comparing the predicted and simulated values, we can see that the CUHI intensities predicted by our approach show agreement with the simulated CUHI intensities. Except for two values with a deviation

of $-0.21\,\mathrm{K}$ and $0.14\,\mathrm{K}$, the rest of the predictions have an error within $\pm 0.1\,\mathrm{K}$.

3.4 DISCUSSION

The UHI effect can increase the frequency of extreme heat events, extend the duration of high temperatures, and narrow the time window for relief from high-heat exposure (Zhao et al., 2018; Schatz et al., 2015; Tan et al., 2010). This heat stress may deteriorate further when taking climate change and rapid ongoing urbanization into account. Moreover, as the majority of the world's population already lives in cities, urban areas are expected to absorb the lion's share of global population growth which is estimated to be 2.2 billion by the end of this century (United Nations Population Division, 2019). This means that in the future many more people will be exposed to more frequent and intensified extreme heat events, not to mention demographic change and an increasing proportion of vulnerable elderly people. Therefore, urban development policies need to take the UHI effect into account (Estrada et al., 2017) and make proper use of effective ways to reduce excessive urban heat.

Achieving this goal requires a more comprehensive understanding of how the UHI effect is influenced by key local- and regional-scale factors such as urban canyon structure, building density, urban surface fraction, and urban form. A challenge in the study of cities is that many factors and characteristics vary among cities, most notably the background climate (Zhao et al., 2014), thermal properties of the rural surface (Runnalls et al., 2000), city size (Oke, 1973), density (Oke, 1987), urban form (Middel et al., 2014), street geometry (Eliasson, 2000; Oke, 1987), and building material (Chapman et al., 2017; Oke, 1987). Here, by employing simulated cities, we can keep the climate conditions constant and clearly define these factors and thus investigate the UHI phenomenon for cities over almost two orders of magnitude.

We quantify the relationship between key urban factors and the CUHI intensity and propose a regression model to quantitatively estimate the CUHI intensity based on detailed 3D urban structure data. Our results show that: firstly, given the same urban area or gross building volume, the CUHI intensity is strongly influenced by the building density (gross building volume per unit area, calculated as the product of total building plan area and average building height within an urban area unit); secondly, increasing building density will lead to stronger CUHI intensity. However, due to different effects of aspect ratio, increasing building plan area causes a more rapid increase in CUHI intensity than adding vertical building height. Given knowledge about the coefficients, Eq. (3.4) can serve to quantify the effect of interventions on the city in question and to investigate scenarios of urban development.

Our results confirm that increasing urban fraction and building height will enhance the CUHI intensity, which is consistent with previous studies (Li et al., 2019b; Yin et al., 2018; Schubert et al., 2013; Van Hove et al., 2015; Straka et al., 2019; Oke, 1981; Oke, 1973). Although increasing building height means more shading effect and less heat storage within a street canyon during the day, it also leads to larger aspect ratios and lower nighttime cooling rates due to stronger trapping of outgoing radiation. The extent to which one of these two effects offsets another still requires further investigation. According to our results, increasing the building density through taller buildings leads to a slower increase in CUHI intensity, and the increase rate gets smaller for larger street canyon aspect ratio (Oke, 1981). On the other hand, based on numerical modelling, Marciotto et al. (2010) found a peak point of aspect ratio at around 3.5, beyond which the maximum CUHI intensity will decrease with increasing aspect ratio. This is not a contradiction as in our work, most of the street canyons still have an aspect ratio below 3.5 even when the height of all buildings is doubled. However, it is also unrealistic to have that large average aspect ratio within many grid cells at 1 km resolution.

Regarding the influence of urban form, our results show that sprawling development will lead to a better thermal environment when considering the entire urban area. Stone et al. (2010) found that sprawled cities show a greater rate of increase in the frequency of annual extreme heat events. A reason for this difference could be their use of observational data acquired at weather stations that are often located near the airport instead of the city centre. Moreover, when the urban area and the gross building volume are controlled, the factors within the term D in Eq. (3.4) still interact with each other non-linearly. Under the premise that the street canyon geometry is homogeneous over all urban sites, the term D clearly indicates that more compact urban clusters will lead to higher CUHI intensities. However, without this precondition, the situation is more complex. Future work that links the quantity D to factors like urban fractality (Batty et al., 1994; Batty et al., 1989; Zhou et al., 2017), urban centrality/poly-centrism (Stone et al., 2010; Batty, 2013), anisometry (Zhou et al., 2017), and intra-urban street canyon geometry will further our understanding of the influence of the urban form on the UHI effect.

Our results, to some extent, cross the scale hierarchy with regards to urban heat stress mitigation by aggregating the complex interactions of vegetation fraction and canyon geometry at the neighbourhood scale grid cell (in our case, at the scale of 1 km^2) into an impact at the city scale. This means that city-scale UHI intensity cannot simply be scaled up from that of the neighbourhood scale, as nearby neighbourhoods also influence each other. Since there is no single best design that meets all climate objectives (Oke et al., 2017), a quantitative assessment of the impact of different designs can help to balance between different

objectives (Oke, 1984; Oke, 2006; Mills, 2006; Mills et al., 2010; Ng, 2012). However, it is beyond the scope of this paper to integrate our findings into a more holistic frame, since decision-making on urban design is a very complex process that requires consideration of many other aspects. For example, a denser city can be preferable regarding energy efficiency but will lead to greater UHI intensity (Mills, 2006), a proper comparison requires a quantitative assessment of both objectives. Even for the same objective of urban heat stress mitigation, it is difficult to clearly prefer one development design over another one before their detailed 3D urban structures are available, or at least some of the factors are fixed. The main reason is that the factors in Eq. (3.4), in particular building height and street width, interact and impose limits on each other. Instead, our approach permits an assessment (Mills et al., 2010; Ng, 2012; Oke, 1984) that takes the 3D urban structures of different urban development scenarios as inputs and enables the comparison between these scenarios with regard to heat stress mitigation on the city scale.

Some limitations exist in this work and the application of our results. Firstly, besides urban form and factors related to street canyon geometry (Oke et al., 2017), weather conditions and rural surface characteristics (Runnalls et al., 2000; Oke, 1987) play an important role in determining CUHI intensities. To apply Eq. (3.4) to another city, one would need to derive the coefficients of the regression again, requiring around 20 simulations. This hampers the fast application of our results, especially for those without expertise in running numerical climate simulations. Properly identifying a representative heat wave event and always using it as standard driving data could help to avoid unnecessary simulations. Secondly, with the coefficients known, applying Eq. (3.4) still requires detailed 3D urban structure data for the development scenarios under consideration. This data will become increasingly available with the rapid development of spatial information technology. Lastly, for simplification and to better separate the influences of the various factors, we excluded anthropogenic heat in this study. For Berlin, the influence of anthropogenic heat release on nocturnal UHI effect should be relatively small during summer according to studies on other temperate cities (Runnalls et al., 2000; Bohnenstengel et al., 2014; Shahmohamadi et al., 2011; Taha, 1997). Moreover, during the night, anthropogenic heat release from cooling should be negligible as the majority of households do not use air conditioning. However, for cities or scenarios where cooling equipment is widely operated during hot summer, UHI intensity can be increased by more than 1 °C (Li et al., 2014; Salamanca et al., 2014; De Munck et al., 2013). Further work on the influence of anthropogenic heat will be helpful for more accurate UHI prediction for cities where cooling devices are widely used.

4

INFLUENCE OF URBAN FACTORS AND BACKGROUND CLIMATE ON SUHI[1]

ABSTRACT

In this study, we analysed the multi-annual (2002-2011) average summer surface urban heat island surface urban heat island (SUHI) intensity of the 5,000 largest urban clusters in Europe. We investigated its relationship with a proposed Gravitational Urban Morphology (GUM) index that can capture the local context sensitivity of SUHI. The GUM index was found to be an effective predictor of SUHI intensity. Together with other urban factors we built different multivariate linear regression models and a climate space based Geographically Weighted Regression (GWR) model that can better predict SUHI intensity. As the GWR model captures the variation of influence from different urban factors on SUHI, it considerably outperformed linear models in predicting SUHI intensity in terms of R^2 and other statistical criteria. By investigating the variation of GWR coefficients against background climate factors, we further built a nonlinear regression model that takes into account the sensitivity of SUHI to regional climate context. The nonlinear model showed comparable performance to that of the GWR model, and it prevailed against all the linear models. Our work underlines the potential of SUHI reduction through optimizing urban morphology, as well as the importance of integrating future urbanization and climate change into the implementation of urban heat mitigation strategies.

KEYWORDS:

Urban form, surface urban heat island, climate context, geographically weighted regression

1 This chapter is based on the published paper: Y. Li et al. (2021b). "Context sensitivity of surface urban heat island at the local and regional scales." *Sustain. Cities Soc.* 74, p. 103146. DOI: 10.1016/j.scs.2021.103146, © Elsevier Ltd. Used with permission.

Notations	
ΔT_s	surface urban heat island intensity, [°C]
A	urban area, [km^2]
D	Gravitational Urban Morphology (GUM) index
$U_{\Delta Wat}$	water surface fraction difference between urban area and boundary area
$U_{\Delta Veg}$	EVI difference between urban area and boundary area
$U_{\Delta Ele}$	elevation difference between the urban area and boundary area, [m]
B_{Ele}	average elevation of boundary area, [m]
B_{Win}	average summer wind speed of boundary area, [ms^{-1}]
B_{Pre}	average summer precipitation of boundary area, [mm]
B_{Tmx}	average summer maximum daily temperature of boundary area, [°C]
B_{Lat}	Latitude of the urban centroid

4.1 INTRODUCTION

The urban heat island (UHI) effect, which refers to the phenomenon that urban areas tend to experience higher temperatures than their rural surroundings, is one of the clearest examples of anthropogenic climate modification (Oke et al., 2017). The UHI effect has various impacts on the local environment and human health (Grimm et al., 2008). The most direct adverse impacts are heat-related health problems (Tan et al., 2010) and increased risk of heat morbidity and mortality (Gabriel et al., 2011; Krummenauer et al., 2019) during hot summer days, as in many cities the UHI effect exposes urban dwellers to extra heat stress.

There are several types of UHIs according to the schemes used to measure them (Oke et al., 2017). Among them, the surface urban heat island (SUHI), measured by urban/non-urban radiative temperature differences derived usually from Land Surface Temperature (LST) data, has attracted considerable interest in recent years due to the advancement of remote sensing techniques, as well as its association with rapid urbanization and global warming which draw increasing attention (Zhou et al., 2019a). The advantages (e.g. spatial/temporal resolution and coverage, data accessibility) of remote sensing data enable researchers to conduct spatially-explicit studies at various spatial and temporal scales (Deilami et al., 2018; Zhou et al., 2019a).

Case studies on small scales (e.g. raster pixel, block, and district level) usually try to explore spatial or temporal SUHI variations to examine statistically a wide range of factors (for example, the share

of vegetation and impervious surface, building density, etc.) and their contributions to SUHI (Deilami et al., 2018; Li et al., 2018; Yang et al., 2019). Studies at this scale often take the LST as a proxy of SUHI intensity and mainly use ordinary least squares (OLS) regression with one or more factors as predictors (Deilami et al., 2018). Recently, an increasing number of studies on the relationship between Local Climate Zones (LCZs) and SUHI intensity (Demuzere et al., 2019; Geletič et al., 2019; Ochola et al., 2020) have been published with resort to the LCZ classification scheme proposed by Stewart et al. (2012). Some researchers also try to link SUHI variations across time with the dynamic of land use/land cover (LULC) (Singh et al., 2017; Sultana et al., 2020).

However, due to fluxes and energy flows between different LULC types, the landscape heterogeneity also plays an important role (Li et al., 2017; Zhou et al., 2019b) and therefore the SUHI is context-sensitive at the local scale (Song et al., 2014). It was found when taking the effects of neighbouring elements (e.g. grid cell or landscape patch) into account by using spatial regression models (Chun et al., 2018; Yin et al., 2018; Dai et al., 2018; Galletti et al., 2019; Guo et al., 2020) or Geographically Weighted Regression (GWR) models (Buyantuyev et al., 2010; Li et al., 2010; Su et al., 2012; Szymanowski et al., 2012; Deilami et al., 2018; Liu et al., 2019; Zhang et al., 2019), higher explanatory or predictive power can be obtained to model/assess the relationship between SUHI variations and the contributing factors. This implies that SUHI at the local scale is influenced by the proximity to and the spatial distribution of nearby warming/cooling factors, and this influence decays as the distance increases.

With this in mind, one could easily arrive at the presumption that when the city is considered as a whole, urban morphology (used in the narrow sense, refers mainly to geometric form) could also have an impact on the city-scale SUHI effect, as urban morphology per se is the aggregated result of the spatial configuration/placement of the fine-scale urban elements. Although many studies (Deilami et al., 2018; Zhou et al., 2019a) have compared SUHI intensities of different cities and attempted to explore the influence of city-level factors (e.g. urban size and density) (Zhou et al., 2013; Li et al., 2017; Song et al., 2020) on SUHI, only a few efforts have been addressed regarding the influence of urban morphology on SUHI. The reasons may be twofold. On the one hand, cities are complex systems with high heterogeneity in various aspects, a less pronounced association between the urban morphology and SUHI intensity is more likely to be obscured by the noise. For example, "compact city" means denser land utilization but probably also leads to less traffic emission (Wang et al., 2015), to which extent the influence from one of these two aspects prevails the other varies across cities. On the other hand, the difference in the biophysical background may further dim the signal from intercity statistics as the

SUHI effect is also sensitive to the regional background climate (Peng et al., 2012; Zhao et al., 2014; Zhou et al., 2014; He, 2018; Manoli et al., 2019).

Regardless of the challenges, some previous investigations provided important insights on this topic. For example, Zhang et al. (2012) analysed the SUHI of 42 northeastern US urban areas within the same ecological context, and they found a linear relationship between SUHI intensity and an urban shape indicator calculated as logarithmic urban area/perimeter ratio. In order to reduce the noise from the background climate, Liang et al. (2020) studied the SUHI of 150 cities with a relatively uniform climate condition in the Jing-Jin-Ji region of China. Based on various regression models, urban form indicators like fractal dimension, contiguity, and elongation have been found to have a stronger positive contribution to the summer daytime SUHI, whereas for SUHI during nights or other seasons, their contributions vary both quantitatively and qualitatively. Some studies also explored qualitatively the climate sensitivity of the relationship between SUHI and urban morphology. For instance, from the statistics based on the 5,000 largest urban clusters in Europe, Zhou et al. (2017) found that a compact urban form featured with large box-counting fractal dimension and small anisometry tends to increase the summer SUHI intensity whilst the influence varies regionally. In more recent work, Liu et al. (2021b) examined the relationships between different urban form metrics and SUHI intensity based on 1288 urban clusters in China, and they found these relationships vary against the climate zones.

These findings advance our understanding of the influence of urban morphology on SUHI as well as its sensitivity to the climate context. However, the quantitative understanding of this sensitivity, which is important for fast SUHI assessment across climate regions, is still lacking. Moreover, urban morphology indicators used in previous studies focus mainly on the 2D morphology of the urban clusters or their component elements, while the spatial pattern of the intra-city heterogeneity in density, which is key to capturing the context sensitivity of SUHI at the local scale, is largely underrepresented.

Recently, based on numerical climate simulations with generated 3D urban structure data (Li et al., 2021a), Li et al. (2020c) proposed a 3D urban morphology indicator that was found to be an effective quantitative indicator linking urban form and canopy layer urban heat island (CUHI) intensity. Although physical processes behind the SUHI effect and the CUHI effect are different (Oke et al., 2017; Peng et al., 2012), the underlying assumption may still apply in both cases, i.e. individual urban cells exert a warming/cooling effect on each other which decays with distance. This assumption is consistent with the context sensitivity of SUHI at the local scale. Therefore, whether a similar indicator also applies to SUHI is worth exploration. As

in (Li et al., 2020c) the urban morphology indicator was calculated resembling the gravitational force, hereafter we name it *Gravitational Urban Morphology* index and GUM index in short.

In this work, we extract the 5,000 largest urban clusters in Europe and calculate their SUHI intensities as well as the GUM index similar to Li et al. (2020c) and analyse the correlations between both. Further, various regression models are built by taking several city-level variables as predictors, such as urban size, the urban-rural difference in vegetation, and water surface share. We explore quantitatively the context sensitivity of SUHI to the regional climate with resort to climate space based GWR model. We explore quantitatively the background climates governed influences of urban factors on SUHI and illustrate how background climate factors can be integrated into a nonlinear model that outperforms linear ones.

4.2 DATA AND METHODS

4.2.1 *Data*

The binary urban/non-urban Urban Morphological Zones 2006 (UMZ2006) data-set at 250 m resolution from the European Environment Agency (EEA) was used to delineate the urban/non-urban area. It was created from CORINE Land Cover data of the year 2006 (CLC2006) following the reclassification method as described in (Simon et al., 2010). UMZ2006 covers 38 European EEA member states and cooperating countries except Greece.

The Land Surface Temperature (LST) data set from the Moderate Resolution Imaging Spectroradiometer (MODIS) onboard the NASA Aqua platform was used, i.e. the 8-day composite product (MYD11A2, version 6 (Wan et al., 2015)). For this work, we only analysed the LST at around 13:30 local time during summer months (June, July, and August) from the years 2002-2011. The LST data set was then processed to get multi-annual summer mean LST following the method used in (Zhou et al., 2017).

Auxiliary data considered in this work include vegetation, background climate, topography, water bodies, as well as urban impervious density.

The vegetation information was extracted from MODIS Enhanced Vegetation Index (EVI) data (MOD13Q1, version 6, Didan (2015)). We downloaded the 16-day composite product during all summer months from the years 2002-2011 and calculated the multi-annual average of the summer EVI.

Regarding the background climate conditions, the multi-annual average of summer precipitation, summer daily maximum 2 m temperature, and summer 10 m wind speed were calculated based on

the corresponding monthly values from two data sets. The monthly precipitation and daily maximum air temperature during summer from 2002-2011 were taken from CHELSA (climatologies at high resolution for the Earth's land surface areas) climate data set. CHELSA is based on a quasi-mechanistical statistical downscaling global reanalysis and global circulation model output (Karger et al., 2017) and has a resolution of 30 arc seconds (∼1km). It is hosted by the Swiss Federal Institute for Forest, Snow and Landscape Research (WSL) and freely available at https://chelsa-climate.org/. The monthly 10 m wind speed data set comes from the German Weather Service (Deutscher Wetterdienst, DWD) Climate Data Centre. This data set consists of gridded monthly mean near-surface (10 m) wind speed values (Brinckmann, 2016) for Europe, and it was created by the project DecReg/MiKlip (Brinckmann et al., 2016) using an interpolation model which combines observation data and reanalysis data. The data set covers the period of 2001–2010 and has a resolution of 0.044° (∼5km). Similar to the precipitation data, only values from the summer months were processed.

Another data source is the Copernicus Land Monitoring Service (CLMS, https://land.copernicus.eu/) funded by the European Union. From CLMS we downloaded the Imperviousness Density 2006 (IMD2006) at 20 m resolution, and the European Digital Elevation Model (EU-DEM, version 1.0) with 25 m resolution, as well as the CLC2006 at 100 m resolution. We aggregated the IMD2006 and EU-DEM data to a coarser resolution of 250 m by assigning each coarse cell the mean value from the fine cells it covers. The CLC2006 was first reclassified into binary water/land map according to whether the cells belong to the level-1 class "Water" (which includes watercourses, water bodies, coastal lagoons, estuaries, sea and ocean, see (Büttner et al., 2012)). The binary map was then resampled to a 250 m resolution with each coarse cell receiving a value of water surface fraction.

To overlay the various quantities, all the processed data sets were reprojected to the sinusoidal coordinate system as used by the LST data set.

4.2.2 *Methods*

4.2.2.1 *SUHI intensity calculation*

We follow a similar methodology as Peng et al. (2012) and Zhou et al. (2013) and Zhou et al. (2017). First, we apply the City Clustering Algorithm (CCA) (Rozenfeld et al., 2008; Rozenfeld et al., 2011; Fluschnik et al., 2016) to the UMZ2006 map, with the parameter $l = 250$m, to assign all cells which are no more than 250 m apart from each other to the same urban cluster. Then we identify the 5,000 largest urban clusters (in terms of area) and the centroid location of each cluster

(indicated in Fig. 4.1(h)). For each of the selected urban clusters, a boundary area with approximately the same size as the urban cluster is created following the method used in (Zhou et al., 2013). Cells that have a water surface fraction over 50% or belong to other urban clusters are excluded when creating the boundary area. Some example urban clusters and the corresponding boundary areas are shown in Fig. 4.1(a-f). Last we define the SUHI intensity (°C) as $\Delta T_s = \overline{T}_u - \overline{T}_b$, where $\overline{T}_u$ and $\overline{T}_b$ are the average LST of the urban cluster and of the boundary area, respectively.

4.2.2.2 *Extraction of other variables*

Analogously, for each urban cluster, we calculate the difference between the average value of water surface fraction, summer EVI, and elevation of the urban area and the corresponding average value of the boundary area, and denote them as $U_{\Delta Wat}$, $U_{\Delta Veg}$, $U_{\Delta Ele}$ (m), respectively.

Moreover, we calculate the average value (summer if applicable) of elevation, EVI, wind speed, precipitation, and maximum temperature within each boundary area and denote them as background biophysical factors B_{Ele} (m), B_{Veg}, B_{Win} (ms^{-1}), B_{Pre} (mm) and B_{Tmx} (°C), respectively. As an important factor controlling solar radiation, the latitude of the centre of mass for each urban cluster is also extracted and is denoted as B_{Lat} (°).

4.2.2.3 *Geographically weighted regression model*

In addition to ordinary least squares (OLS) regression models, we performed a Geographically Weighted Regression (GWR) to explore spatially varying relationships between the SUHI intensity and its explanatory variables. GWR is a non-parametric model that takes spatial non-stationary influences from associated factors into account by applying a locally weighted linear regression (Jian et al., 1996) for each observation with a subset of nearby observations (Fotheringham et al., 2003), and therefore allows parameters to vary across space. GWR usually takes the form

$$y_i = \theta_0(u_i, v_i) + \sum_k^n \theta_k(u_i, v_i) x_{k,i} + \epsilon_i \,, \tag{4.1}$$

where n is the number of independent variables; i denotes the ith observation; (u_i, v_i) is the coordinate of the ith location; $\theta_0(u_i, v_i)$ is the constant intercept depending on the coordinate (u_i, v_i); y_i, $x_{k,i}$, and ϵ_i are dependent variables, independent variable and the error term respectively; and the coefficients $\theta_k(u_i, v_i)$ are varying conditionals of the observation locations (Nakaya et al., 2014). The proximity of geographical positions can, to some extent, represent the similarity of climate conditions, but not always. For example, two

cities located in proximity to each other but on opposite sides of a ridge may largely differ in background climate, especially in the patterns of precipitation and wind. One of our goals is to investigate climate control on the SUHI. Therefore, instead of a common GWR that takes only geographical location (u, v) as coordinates into account for Eq. (4.1), in this work we project the 5,000 cities into a 6-dimension space using their corresponding background biophysical factors, namely B_{Pre}, B_{Tmx}, B_{Veg}, B_{Win}, B_{Ele}, and B_{Lat} – forming a kind of *climate space*. A similar application of GWR can be found in (Hooker et al., 2018). To remove the influence of the magnitude of different climate variables, z-score normalization is applied to each of them. The coordinate of the ith city in the constructed space will be $\vec{P_i} = \{z(B_{Pre})_i, z(B_{Tmx})_i, z(B_{Lat})_i, z(B_{Veg})_i, z(B_{Ele})_i, z(B_{Win})_i\}$. This way, the distance between city i and j within the 6-dimension space can be calculated as $d_{i,j} = |\overrightarrow{P_i P_j}| = \sqrt{\sum_{k=1}^{6}(P_{i,k} - P_{j,k})^2}$.

For a city at location i, coefficients $\theta_{k,i}$ and ϵ_i are estimated by locally fitting a weighted linear regression that only takes its neighbouring cities within a certain distance L in the constructed climate space into account. In this work, the weight of city j is calculated using a tricube function, i.e. $w_j = (1 - (d_{i,j}/L)^3)^{1/3}$, with $d_{i,j} \leq L$. The local WLR leads to a set of coefficients $\{\theta_0(\vec{P_i}), \theta_1(\vec{P_i}), ..., \theta_n(\vec{P_i}), \epsilon_i\}$ and after application to each of the 5,000 cities we get 5,000 sets of coefficients. The GWR is implemented using the R-package "GWmodel" (Lu et al., 2014). An optimally fixed bandwidth L is estimated using the leave-one-out cross-validation method, technical details can be found in Lu et al. (2014).

4.2.2.4 *GUM index calculation*

In the work of Li et al. (2020c), a Gravitational Urban Morphology (GUM) index was found to be capable of capturing the influence of urban form on canopy layer urban heat island (CUHI) intensity. This index is calculated as $\frac{1}{N}\sum_{j}^{N}\sum_{i\neq j}^{N} f(x_i) d_{ij}^{-\beta}$, where N is the number of cells of the considered urban cluster, d_{ij} is the distance between two urban cells i and j, and $f(x_i)$ is the function of the urban metric x influencing the temperature at site i. This was based on the hypothesis that an urban cell is affected by the warmth of other urban cells and this effect declines with the distance between them, also warmer urban cells have stronger effects on their neighbouring cells. Many studies show that the land surface temperature is highly related to characteristics like impervious surface fraction (Morabito et al., 2020; Li et al., 2011), building density (Song et al., 2020; Yin et al., 2018), vegetation fraction (Mathew et al., 2017; Li et al., 2011; Zhou et al., 2014), etc. Particularly, Li et al. (2018) revealed a linear relationship between land surface temperature and regionalized impervious surface area.

Therefore, in this work, we include impervious surface fraction and calculate our GUM index according to

$$D = \frac{1}{N} \sum_{j}^{N} \sum_{i \neq j}^{N} u_i^{\alpha} d_{ij}^{-\beta}, \tag{4.2}$$

where u_i is the impervious surface fraction of urban grid cell i, α and β are key exponent parameters. We calculate D for each of the 5,000 urban clusters and examine whether it also has an impact on the SUHI intensity.

4.3 RESULTS

4.3.1 *Influence of urban size and morphology on SUHI*

We find that SUHI intensity ΔT_s is moderately related to urban area A, see Appendix C, Table C.1 and Fig. C.1. There is roughly a linear relationship between ΔT_s and logarithmic A, which is consistent with previous studies (Zhang et al., 2012; Zhou et al., 2017; Li et al., 2017). This implies that with the same amount of urban area increment, a larger city tends to experience a smaller increase in SUHI intensity. However, this does not mean it is preferable to have urban expansion concentrated in large cities, as the cost from heat stress is a super-linear function of temperature and population size (Estrada et al., 2017; Krummenauer et al., 2019).

Regarding the urban morphology, the relationship between GUM index D and SUHI intensity ΔT_s varies with the exponents α and β. Specifically, when $\alpha = 0.2$ and $\beta = 2$, D has a high correlation with ΔT_s, the Pearson correlation coefficient r reaches 0.64 (see Appendix C, Table C.1 and Fig. C.1 for the correlation and the spreading range of D). In Fig. 4.1(a-f) we show six example urban clusters with approximately the same area and corresponding D values when $\alpha = 0.2$ and $\beta = 2$ are used. It can be seen – when keeping the urban size constant – compact cities generally tend to have a larger D value. However, it has to be noted that this does not always hold as the impervious surface density also has an influence on D. As D is a very complex indicator which involves the spatial configuration of the urban cells as well as their built-up density, without some preconditions (i.e., same size or same impervious surface fraction), it is hard to get the conceptual impression of whether one city is more compact than another through comparison of their value D. Generally, cities with a rounder shape and higher impervious density will have a larger D value. Fig. 4.1(g) shows ΔT_s against D (with $\alpha = 0.2$, $\beta = 2$) of some example cities with approximately the same area ($15 \pm 0.06 \text{km}^2$, for other areas sizes, see Appendix C, Fig. C.2). As shown, ΔT_s is positively related to the D value despite the fluctuation that might be attributed to the influence of other factors, in particular background climate and water bodies.

This implies that more compact and denser urban structures tend to have higher SUHI intensities. Moreover, urban heat mitigation strategy through optimizing urban morphology should carefully consider the local scale context sensitivity of SUHI, as this neighbourhood effect can impact the city scale thermal environment when aggregated.

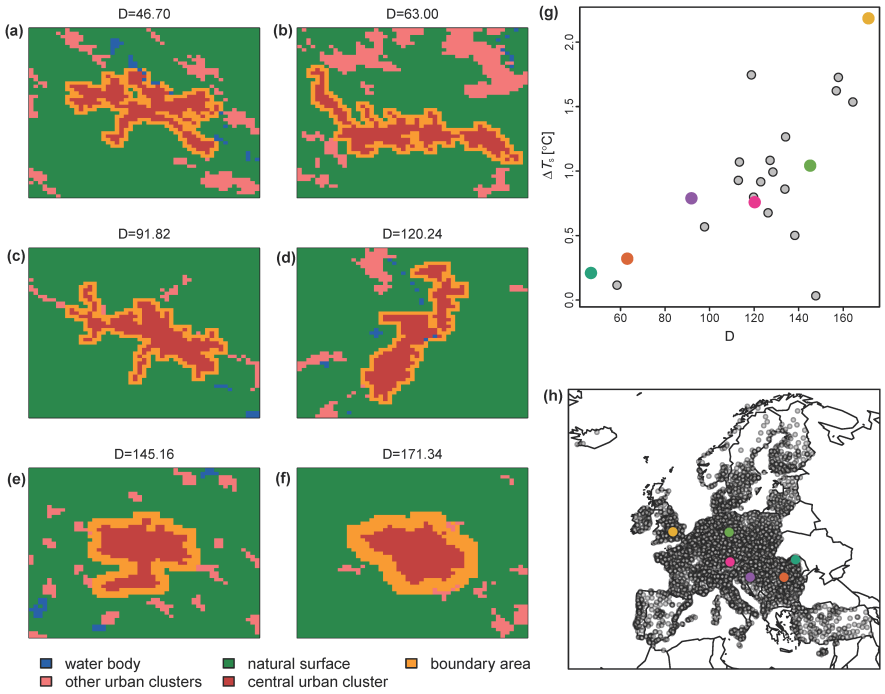

Figure 4.1: Some example urban clusters with approximately the same size, their boundary areas, as well as the corresponding D values and surface urban heat island (SUHI) intensities. Panel (**a**-**f**) show the clusters of the highlighted clusters in panel **g**, the size of these six clusters ranges from 14.94-15.06 km^2. Panel (**g**) shows the SUHI intensity against D value of 41 urban clusters with approximately the same size, where the points in colours represent the clusters in Panel (**a**-**f**). Panel (**h**) shows the spatial locations of all 5,000 clusters with the clusters in panel (**a**-**f**) highlighted in colours.

Similar to the approach used by Li et al. (2020c), we regress ΔT_s with A and D as:

$$\Delta T_s = a_1 \ln A + a_2 D + a_3 \quad \text{with} \quad D = \frac{1}{N} \sum_{j}^{N} \sum_{i \neq j}^{N} u_i^{\alpha} d_{ij}^{-\beta}, \tag{4.3}$$

where a_1, a_2, a_3 are parameters. Fitting Eq. (4.3) using the data of all 5,000 cities with different combinations of α and β, we obtain varying R^2 (see Fig. 4.2).

We find $\alpha = 0.2$, $\beta = 2$ leads to best results in terms of R^2 (which is 0.40). These values differ from the ones found by Li et al. (2020c) for canopy layer UHI intensity ($\alpha = 0.5$, $\beta = 1.5$). Since the canopy layer and surface UHI involve different processes, we cannot directly compare them, but it is still worth thinking about possible

implications for the conceptualization. A larger β value implies that the neighbourhood influence of the LST decays faster and thus has a shorter range than the canopy layer temperature. It is plausible that air temperature has a smoother spatial gradient than the LST as the former is more easily influenced by energy and airflow. This indicates that at the local scale, SUHI is less context-sensitive than CUHI. For SUHI, the influence from nearby urban cells decays very fast with increasing distance. Thus, the neighbourhood influence can only reach a rather small range.

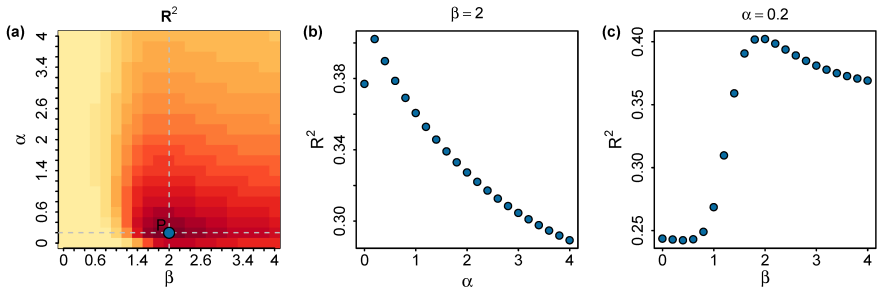

Figure 4.2: The R^2 of the ordinary least squares (OLS) fitting on Eq. (4.3) as a function of α and β values. (**a**) 2D visualization, deeper red for higher R^2. (**b**) R^2 profile when $\beta = 2$. (**c**) R^2 profile when $\alpha = 0.2$.

The coefficients from the fitting for Eq. (4.3) with $\alpha = 0.2$, $\beta = 2$ are also shown in Table 4.1, all of them are above 95% significance level. It is also worth mentioning that although D and $\ln A$ are not independent, a variance inflation factor of 2.21 suggests an insignificant impact of the co-linearity between $\ln A$ and D on the reliability of the regression, as usually a value > 10 is considered severe (Neter et al., 1996).

To avoid ambiguity, the GUM index D refers to the one calculated with $\alpha = 0.2$, $\beta = 2$ for the remainder of this paper.

4.3.2 *Influence of additional urban factors*

Although we obtain a slightly higher R^2 when using Eq. (4.3) as regression with fewer parameters compared to the multivariate linear regression in (Zhou et al., 2017), there is still a large part of the variance of ΔT_s that is not explained by $\ln A$ and D (see Appendix C, Fig. C.5 and Fig. C.3). This is due to the influences of many other factors. As reported in various studies, water bodies (Zhou et al., 2014; Yin et al., 2018; Wang et al., 2019), vegetation (Zhou et al., 2011; Zhou et al., 2014; Yu et al., 2018), and altitude (Mathew et al., 2017; Guo et al., 2020) are also associated with SUHI intensity. This is further confirmed by our results, as we can see in Fig. 4.3, there is a statistically significant correlation between ΔT_s and urban-boundary difference in EVI ($U_{\Delta Veg}$), in water surface fraction ($U_{\Delta Wat}$), and in elevation ($U_{\Delta Ele}$). In general,

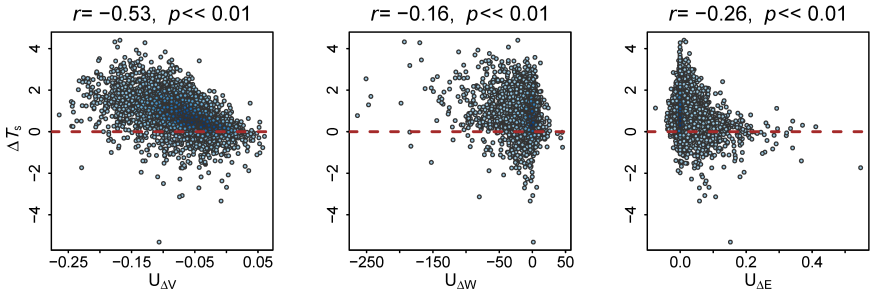

Figure 4.3: ΔT_s against additional urban factors. (a) $U_{\Delta Veg}$, urban-boundary difference in EVI, (b) $U_{\Delta Ele}$, urban-boundary difference in elevation, and (c) $U_{\Delta Wat}$, urban-boundary difference in water surface fraction. On the top of each panel, Pearson Correlation (r) and p value are listed.

cities with less vegetation, lower altitude, and less water surface than their surroundings, tend to experience stronger SUHI intensities. This is consistent with previous studies on the contributions of green and blue infrastructure to urban heat mitigation. Our results particularly underpin the effect of urban greening on SUHI reduction. Including these factors in Eq. (4.3) and using the regression

$$\Delta T_s = b_1 \ln A + b_2 D + b_3 U_{\Delta Wat} + b_4 U_{\Delta Veg} + b_5 U_{\Delta Ele} + b_6 \,, \quad (4.4)$$

we obtain coefficients detailed in Table 4.1, where all coefficients are above 99% significance level. Including $U_{\Delta Wat}$, $U_{\Delta Veg}$, and $U_{\Delta Ele}$ in the regression model, Eq. (4.4) achieved a clear improvement of R^2 and of RMSE in contrast to Eq. (4.3).

4.3.3 *Sensitivity of SUHI to regional climate context*

Besides the intrinsic urban factors that denote the urban-boundary differences due to land surface modification from urbanization, SUHI has been reported to be associated also with various background biophysical factors such as precipitation, temperature, humidity, wind speed, latitude, and altitude, among which precipitation (Peng et al., 2012; Zhao et al., 2014; Manoli et al., 2019), and temperature (Peng et al., 2012; Zhou et al., 2016; Manoli et al., 2019) seem to be most documented. Therefore, SUHI is also context-sensitive to regional climate background.

This regional scale context sensitivity can be seen in Fig. 4.4. When plotting ΔT_s against each of the 6 background factors, ΔT_s has a clear correlation with B_{Pre} and with B_{Tmax}, which is consistent with previous studies (Peng et al., 2012; Zhou et al., 2014). The positive relationship between ΔT_s and B_{veg} can be explained by the tendency of boundary areas with higher EVI to be generally cooler due to stronger evapotranspiration. There is a positive correlation between ΔT_s and B_{Lat}, which is consistent with the finding in (Li et al., 2017). However, beyond a certain latitude, ΔT_s seems to decrease when

latitude increases. Our results do not show a statistically significant correlation between ΔT_s and B_{Ele} or B_{Win}, which might be due to the correlation being too weak to stand out from noises caused by other factors. The correlation between the residuals from the regression

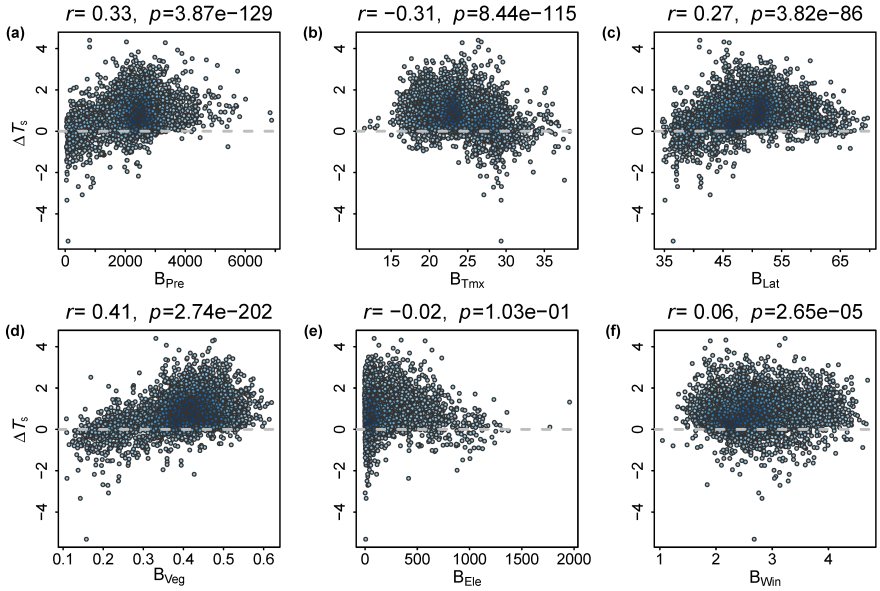

Figure 4.4: SUHI intensity ΔT_s against background biophysical factors: (a) summer precipitation B_{Pre}. (b) summer mean maximum temperature B_{Tmx}. (c) latitude B_{Lat}. (d) summer EVI of boundary area B_{veg}. (e) elevation B_{Ele}. (f) summer 10 m wind speed B_{Win}. r and p on the top of each panel indicate the Pearson correlation coefficient and the significant level of the plotted variables.

of Eq. (4.4) and the six background biophysical factors (as shown in Appendix C, Fig. C.4) indicate that the explanatory power of the regression model could be improved by including these background factors. In principle, one could just extend the regression by including them in the multivariate linear model. However, those background factors are likely to interact with urban factors and the interactions are not necessarily linear (Li et al., 2019a; Manoli et al., 2019). Moreover, It is plausible that the dependence of SUHI on climate context results from the role of background climate in controlling how SUHI respond to urban factors.

4.3.4 *Geographically Weighted Regression*

We are interested in exploring how the influence of urban factors on the SUHI intensity varies regionally across the climate context. To this end, we apply the GWR

$$\Delta T_i = \theta_0(\vec{P}_i) + \sum_k^5 \theta_k(\vec{P}_i) x_{k,i} + \epsilon_i \,, \tag{4.5}$$

where $\theta_0(\vec{P}_i)$ is the intercept of the regression for the ith city, $x_{k,i}$ is the kth independent variable as that used in Eq. (4.4) of the ith city.

Fitting Eq. (4.5) leads to a set of coefficients $\{\theta_{0,i}, \theta_{1,i}, ..., \theta_{5,i}, \epsilon_i\}$ for each of the 5,000 cities, and thus we get 5,000 sets of coefficients. We notice that Li et al. (2017) applied GWR on 5,000 urban clusters across the conterminous US based on their geographical location and then investigated the spatial variation of the relationship between SUHI and urban area. In our work, the GWR is applied based on a constructed 6-dimension biophysical space in order to study the variation of the relationship between SUHI and various urban factors against each background biophysical factor.

The statistics of GWR results can be found in Table 4.1. Compared with the regression of Eq. (4.3) and Eq. (4.4), it shows apparent improvement in R^2 and RMSE. This indicates that the relationship between SUHI and urban factors is not stationary across the climate context. The density plot of residuals from all three regression models are also compared in Appendix C, Fig. C.5.

Model	Eq. (4.3)	Eq. (4.4)	GWR
coef. ln A	5.13×10^{-2}	0.17	$5.44 \times 10^{-2}(0.10)$
coef. D	1.31×10^{-2}	6.15×10^{-3}	$1.09 \times 10^{-2}(6.05 \times 10^{-3})$
coef. $U_{\Delta Wat}$	–	-6.00	-4.90 (2.03)
coef. $U_{\Delta Veg}$	–	-6.53	-4.27 (3.24)
coef. $U_{\Delta Ele}$	–	-3.90×10^{-3}	$-5.69 \times 10^{-3}(2.21 \times 10^{-3})$
intercept	-0.90	-0.79	-0.86 (0.21)
R^2	0.40	0.55	0.74
RMSE	0.63	0.54	0.41
AICc	1161.56	395.67	-979.27

Table 4.1: Comparison of OLS fitting and GWR fitting. Numbers within the bracket are the standard deviations of corresponding values. AICc (corrected AIC) is calculated following Zhou et al. (2016).

We also plot the residuals of the GWR model against the background biophysical factors as in Fig. 4.5. Compared to Appendix C, Fig. C.4 where residuals from the linear regression of Eq. (4.4) are plotted against the background biophysical factors, we can clearly see that the residuals from the GWR model are much less correlated with background factors. This implies that the variation of coefficients of the GWR model to a large extent resolves the sensitivity of SUHI to regional climate context and the background factors that impact SUHI by affecting the way that SUHI responds to urban factors. These varying relationships also suggest that the cost-efficiency of different urban heat mitigation strategies is highly dependent on climate context. Special caution should be exercised when extending lessons

learned from one city to another, especially when they share less in common regarding background climate.

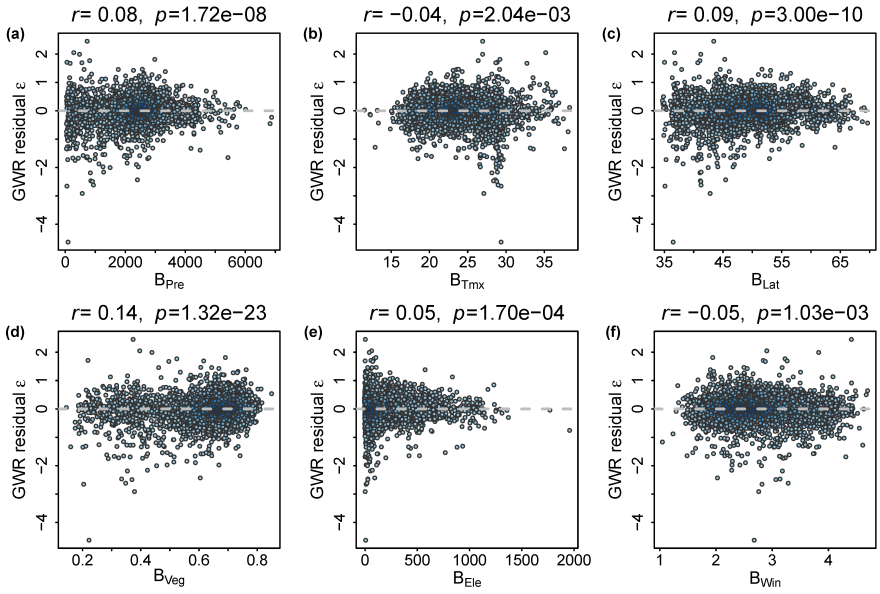

Figure 4.5: residuals from GWR model against background factors: (a) summer precipitation B_{Pre}. (b) summer mean maximum temperature B_{Tmx}. (c) latitude B_{Lat}. (d) summer EVI of boundary area B_{veg}. (e) elevation B_{Ele}. (f) summer 10 m wind speed B_{Win}.

4.3.5 *Non-stationary influences of urban factors governed by background climates*

The GWR model gives flexibility to the coefficients of the regression. Thus, it takes the non-stationary associations of different factors with SUHI into consideration. As this non-stationarity is also believed to be modulated by climate context, we apply the GWR based on a constructed climate space. In this way, the local regression is applied on the clusters of cities with the most similar background climate, so that the influence from background factors is minimized and the statistical contribution of each urban factor can be examined regionally.

In Appendix C, Table C.2 we show the Pearson correlation coefficients between the GWR coefficients and the background biophysical factors. Some background factors, such as precipitation B_{Pre}, air temperature B_{Tmx}, latitude B_{Lat}, and vegetation condition B_{Veg}, have a clear correlation with GWR coefficients, where the highest correlation coefficient reaches 0.84, indicating the strong influence of the background factors on the variation of the GWR coefficients. This is not surprising as in previous studies it has been found that precipitation and temperature show a strong control on daytime SUHI (Zhao et al., 2014; Zhou et al., 2016; Manoli et al., 2019). We can also see that some coefficients show a strong correlation with more than one

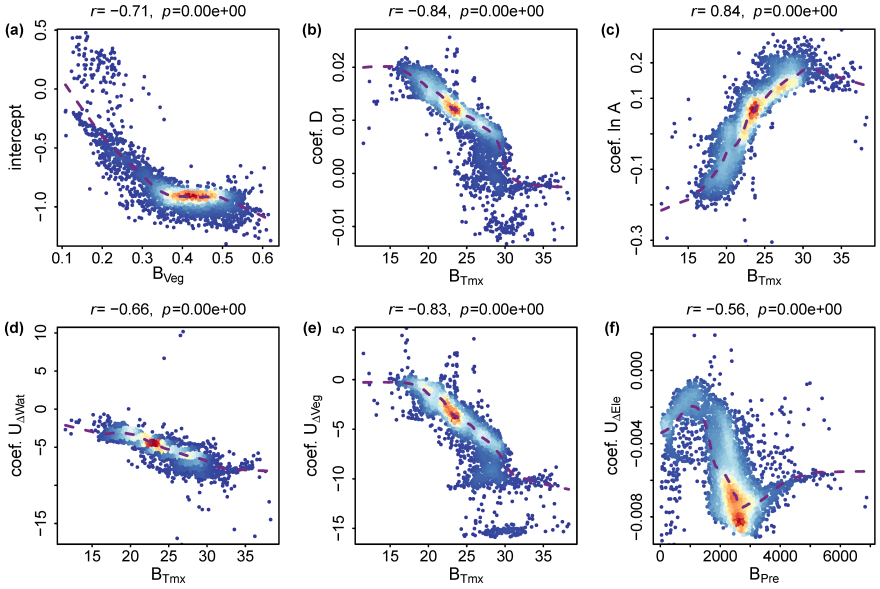

Figure 4.6: Relationship between some coefficients from GWR and background climate factors. The dashed lines are a guide to the eye from LOWESS (Locally Weighted Scatter plot Smoothing) regression.

background factor. However, without comprehensively studying the underlying dynamics it is difficult to prioritize one background factor over another.

We plot each GWR coefficient against its highest correlated background factor in Fig. 4.6. Despite some noise, all the GWR coefficients except that of ln A generally maintain the sign while varying in quantity. This implies that strategies for SUHI reduction through changing one of the urban factors might show different efficiency under different biophysical contexts – the consequence seems to be consistent qualitatively. Our results indicate that when other urban factors remain constant, urban sprawl tends to cause smaller SUHI increment for cities in northern European, or more specifically, in colder, wetter, windier and more vegetated areas (see Appendix C, Fig. C.6). Likewise, with similar preconditions, we can infer that a colder, wetter, windier and more vegetated context would favour the contribution of urban morphology D to SUHI, but weaken the contribution of water surface share difference $U_{\Delta Wat}$ and EVI difference $U_{\Delta Veg}$ (see Appendix C, Fig. C.7-C.9). However, a general trend on the variation of coefficient of elevation difference $U_{\Delta Ele}$ is more complex and can hardly be drawn qualitatively (Appendix C, Fig. C.10).

4.3.6 *Nonlinear model considering climate influence on SUHI*

In principle, all the factors used in this study can be fed into a multiple linear regression model of the form

$$\begin{aligned}\Delta T_s =& c_1 \ln A + c_2 D + c_3 U_{\Delta Wat} + c_4 U_{\Delta Veg} + c_5 U_{\Delta Ele} + \\ & c_6 B_{Pre} + c_7 B_{Tmx} + c_8 B_{Veg} + c_9 B_{Ele} + c_{10} B_{Lat} + c_{11}\,,\end{aligned} \tag{4.6}$$

and with more variables, we could obtain an RMSE of 0.46, which is better than that of fitting Eq. (4.4), but still larger than the RMSE from the GWR model. As there are complex dynamic processes controlling the SUHI, the factors, both from urban metrics and from background biophysical factors, tend to interact with each other non-linearly. A linear regression model certainly cannot capture the interacting effect as it is just a combination of the linear approximation for each factor.

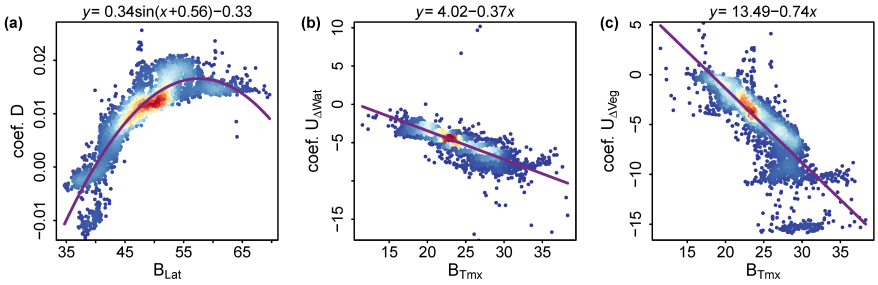

Figure 4.7: GWR coefficients as a function of background biophysical factors. The solid line is the fitted curve as expressed on top of each panel.

Although regression with the GWR model has higher accuracy, it does not necessarily mean the GWR model has better practical usability. The parameter estimation of GWR comes from local fitting with location-specific information, which limits the generality of the model and a better understanding cannot be obtained without further exploration. Instead, by examining the linkages between the variation of the GWR coefficients of each urban factor and background factors, the effect of interactions between the background factors and urban factors can be quantitatively studied. This could help to formulate a more general regression model to estimate the SUHI intensity. For example, in Fig. 4.7(a), after having a closer look at the relationship between the GWR coefficients of D and the latitude B_{Lat}, and considering that the total solar irradiance should be a trigonometric function of the latitude, we could fit the coefficient of D with latitude B_{Lat} in the form of $e_1 \sin(x + e_2) + e_3$. Similarly, for the coefficient of $U_{\Delta Wat}$ and the coefficient of $U_{\Delta Veg}$, we find they can be roughly expressed as a linear function of B_{Tmx}. With this knowledge, we extend the global linear regression of Eq. (4.4) by replacing the coefficients of D, $U_{\Delta Wat}$ and $U_{\Delta Veg}$ with functions of the above-mentioned climate factors

$$\begin{aligned}\Delta T_s =& d_1 \ln A + [d_2 \sin(B_{Lat} + d_3) + d_4]\, D + \\ & d_5 B_{Tmx} U_{\Delta Wat} + (d_6 B_{Tmx} + d_7) U_{\Delta Veg} + d_8 U_{\Delta Ele} + d_9,\end{aligned} \tag{4.7}$$

and we obtain an RMSE of 0.44 from fitting Eq. (4.7), which is better than the multivariate linear fitting with all considered factors (Eq. (4.6)) and very close to the RMSE from the GWR model.

In Appendix C, Fig. C.5, we compare all the regression models mentioned in this work in terms of their residuals, RMSE, and AICc Zhou et al. (2016). It can be seen that the GWR model outperforms all other models, which is followed by the nonlinear regression of Eq. (4.7). Particularly, if we compare the regression of Eq. (4.7) with that of Eq. (4.6), a smaller RMSE is achieved with fewer parameters when some interactions between the factors are taken into account. This shows that the GWR model can help to find a better SUHI prediction model as it enables us to explore the interactions between some factors. Thus, the model based on Eq. (4.7) is preferable as a tool for SUHI prediction and may have even more implications for SUHI assessment under the scenarios of future urbanization and climate change, as the model uses both urban factors and background biophysical factors as predictors for SUHI intensity.

It has to be noted that the nonlinear model in the form of Eq. (4.7) may not be the optimal one as different background factors can be introduced with functions taking different forms (see Supplementary Fig. C.6-C.10). Rather, we illustrate here how the GWR model can help to obtain a better model that captures the context sensitivity of SUHI to regional background climate.

4.4 DISCUSSION

4.4.1 *Urban morphology and SUHI*

Taking a similar form as the one proposed in (Li et al., 2020c) which was used to link CUHI intensity with urban morphology, the GUM index in this work turns out to be also an effective indicator to capture the relationship between SUHI intensity and urban morphology. Our results agree with previous studies on the contribution both of 2D urban compactness (Zhang et al., 2012; Zhou et al., 2017) and of the urban density (Zhang et al., 2012; Li et al., 2018; Song et al., 2020) to SUHI intensity. Compared with various metrics for quantifying 2D urban morphology in previous studies, our approach underlines the importance of looking at cities from a 3D perspective, as 2D urban morphology neglects the influences from urban development within already urbanized areas (i.e., urban densification). The GUM index combines the 2D geometry of the urban clusters and the spatial heterogeneity of the impervious density inside, where the latter is key to capturing the local scale context sensitivity of SUHI and could affect the city scale SUHI when aggregated. It can serve as an effective predictor for SUHI intensity assessment in view of urbanization which usually involves both densification and sprawl.

Also similar to (Li et al., 2020c), generally the GUM index indicates that cities with higher compactness and density tend to have stronger SUHI. However, specific implications regarding the influence of urban morphology on SUHI intensity could only be interpreted with some preconditions. For example, assuming the urban area A remains unchanged and the impervious surface fraction u is homogeneous within the urban cluster, the GUM index D degrades to an indicator that measures the compactness of the 2D urban morphology. Under this circumstance, it implies that from a 2D perspective cities with a rounder shape will have larger SUHI intensity.

In principle, the weight function used in calculating the GUM index D should not be limited to a function of only urban impervious surface fraction u. Other indices like urban canyon geometry, building density, water surface fraction, and vegetation fraction can also modulate the LST at the local scale (Zhang et al., 2012; Mathew et al., 2017; Song et al., 2020; Liu et al., 2021a). Therefore, a more complex indicator that considers the heterogeneous configuration of and the interaction between these indices within the urban cluster probably can carry more prediction power on the resulted SUHI intensity. However, this requires much more effort and a more comprehensive understanding of the underlying biophysical processes (Manoli et al., 2019) through which the considered factors influence the LST. Future work in this direction is needed.

4.4.2 *Drivers of SUHI*

While it is easy to infer the statistical linkages between SUHI and related factors, revealing the causality is a very different challenge, especially given the fact that many natural and socioeconomic factors found to be associated with SUHI are correlated among themselves. Therefore, efforts to identify the driving factors as well as their corresponding contribution to SUHI might lead to discrepant and sometimes contradicting conclusions. This is either due to the combination of factors chosen or due to the studied samples that are not suitable for factor separating.

For example, although the association between SUHI and the urban area has been examined by studies at different scales (Peng et al., 2012; Zhou et al., 2017; Li et al., 2017), community consensus over the understanding of this statistical correlation still lacks. Peng et al. (2012) find no obvious effect of urban size on the SUHI for 419 global big cities, but a significant positive correlation exists for 56 European cities, they surmise that the effect of urban size at the global scale might be masked by the differences in background climate or economic development. Zhou et al. (2017) take a logarithmic function to capture the relationship between SUHI and urban size, meanwhile, they also illustrate the suitability of a log-logistic function

as an alternative. Li et al. (2017) point out that although the log-linear relationship between SUHI and urban area exists across the continental US with local variation attributed to contextual biome, the urban area is only a useful surrogate of other factors determining SUHI instead of being a major direct driving factor. This is plausible, especially considering the fact that urban area is strongly correlated with population size, infrastructure size, energy consumption, and many other city-level socioeconomic metrics via well-documented urban scaling laws (Gudipudi et al., 2019).

For other factors, attempts to quantify their contribution as a driving factor of UHI face similar problems as when studying urban areas as driving factors. Thus, without a general understanding, results from one region carry little application capability for another region, or at least, it is risky to extrapolate the implication from one study beyond space and time. Therefore, causal attribution requires more than statistical analyses between SUHI and the potential driving factors. A combination of a statistical with a proper analytical attribution model (Li et al., 2019a; Chen et al., 2020) based on energy balance could help to advance our understanding of the SUHI and thus guide the inference of causality between SUHI and related factors. For instance, in the work by Manoli et al. (2019), various urban characteristics and aerodynamic properties are expressed using urban population size resorting to the urban scaling law and a coarse-grained model has been developed to foster the general understanding of SUHI and the model has been shown capable of explaining the seasonal SUHI hysteresis (Zhou et al., 2013; Manoli et al., 2020).

Partitioning the contribution from different factors to the SUHI is beyond the scope of this work. With the observed results, we could only draw the implication that in general, larger, more compact cities with less water surface, less vegetation and lower than surrounding area altitude tend to experience a stronger SUHI. When taking these factors as predictors, the regression model works quite well. With the help of the GWR model, we are also able to see how the influence of each urban factor varies across background biophysical space. Generally, cities in Europe with colder, wetter, windier and more vegetated backgrounds tend to experience stronger SUHI increment due to increased compactness, but less SUHI reduction due to increased water surface and vegetation. Moreover, with the help of the GWR model, we are able to build a more general nonlinear model that can take the context sensitivity of SUHI at both local and regional scales. This model could serve as a useful quantitative tool for SUHI intensity assessment with different urbanization scenarios and climate change scenarios as input.

4.4.3 *Possible explanation of outliers*

In addition to the factors considered in this study, many others like building density, albedo, humidity, wind direction, and water proximity also play a role in the formation of SUHI (Peng et al., 2012; Oke et al., 2017), and we assume they can be neglected. Although the urban-boundary differences in water surface fraction and in elevation are considered in the regression model, they cannot fully capture the influence of water proximity and topography on SUHI.

In Appendix C, text, by further analysing the cities with large errors ($|\epsilon| > 1$) of the GWR regression, we examine qualitatively how water proximity affects the SUHI intensity of a city in some cases. Specifically, the proximity to the nearby large water bodies and particularly, whether the urban area is closer to the water body than the boundary area, can strongly influence their difference in the received cooling effect (see Fig. C.13). However, a proper indicator is in need to quantitatively capture this difference. Based on fine resolution Landsat LST image, Wang et al. (2019) proposed a gravitational water index that measures the cooling effect from nearby water cells received by grid cell i as $GWI_i = \sum_{d_{ij}<R} \frac{A_j}{d_{ij}^{\gamma}}$, where A_j is the water area in cell j. This index considers the influence from other water surfaces within a certain distance R for each grid cell and the influence decays as a power-law function of the distance to the water surface. The gravitational water index was found to be able to explain the LST variation at different grid scales. Probably a similar index can be developed for quantifying city-scale influence from nearby water surfaces, and it may be an effective predictor of SUHI intensity. However, as two major parameters of the gravitational water index, the exponent γ which defines how stark the cooling effect decays and the distance threshold R up to which the cooling effect can reach, are very likely to vary even within one city (Du et al., 2016), not to mention for whole Europe. Therefore, it is beyond our scope to verify such an index or its variant.

Moreover, we also observe some cities with a larger positive prediction error which are situated in a valley like in Fig. C.12(b-c). This might imply that topography also plays a role by influencing heat dissipation. Although the GWR model already showed that cities with larger elevation differences between urban and boundary areas tend to have stronger SUHI, the topography characteristics as in Fig. C.12(b-c) may not be simply quantified by elevation differences. Future efforts for proper indicators that consider the spatial pattern of the topography can help with a better SUHI intensity estimation model.

4.5 CONCLUSION

In this study, we investigate the summer daytime SUHI intensity of the 5,000 largest urban clusters in Europe and demonstrate the capability of the proposed GUM index as an effective predictor of SUHI intensity. The GUM index is designed to capture the context sensitivity of SUHI to the local neighbourhood effect and it quantifies the urban structure from a 3D perspective. The regression model can be improved when taking other urban factors like urban-boundary differences in vegetation, water surface fraction and elevation into account. The regression models show that generally larger, denser, and more compact cities tend to experience stronger SUHI, whereas cities with a larger urban-boundary difference in elevation, vegetation cover and water surface cover tend to have lower SUHI intensity.

To explore the sensitivity of SUHI to regional climate context, we then project all the cities in a 6-dimension climate space constructed using six background biophysical factors. The GWR model is applied based on the constructed climate space to explore how the coefficients vary against different background biophysical factors. The GWR model shows further considerable improvement in terms of R^2 and RMSE compared with multivariate linear models. By enabling the variation of coefficients, the control from the background climate on the non-stationary contribution of different urban factors to SUHI can be captured by the GWR model. As the influence of different urban factors on SUHI is context-sensitive to regional climate, extrapolating knowledge from one area to another should be done with great caution, especially between areas with disparate climates.

Investigating how the GWR coefficients vary against different background biophysical factors, we demonstrate how to replace the coefficients in the multivariate linear model with the background factors and propose a nonlinear model that can capture some of the interactions between the urban factors and the background biophysical factors. It carries fewer parameters but outperforms multivariate linear models. The nonlinear model considers the context sensitivity of SUHI at both local and regional scales, it is a more general model that can be used for SUHI assessment under different urbanization and climate change scenarios.

Our results could provide useful information regarding urban heat reduction strategies, especially considering the ongoing rapid global urbanization and climate change. A better urban development plan that takes the influence of urban morphology into account could benefit the urban thermal environment. Moreover, measures for urban heat mitigation should also consider the predicted climate change. As the climate context of a city may change in the future, heat mitigation strategies that are effective for the short term might show little efficiency in the long term.

5 SYNTHESIS

5.1 GENERAL ACHIEVEMENTS

The urban heat island (UHI) effect exposes urban dwellers to additional heat stress (Chapman et al., 2017). A comprehensive understanding of the UHI dynamics along with urbanization is of great importance for efficient heat stress mitigation strategies towards sustainable urban development. In this work, we present a quantitative analysis of how urban intrinsic properties (e.g., urban size, density, morphology, etc.) influence the most studied UHI types – CUHI and SUHI.

We first combine urban growth modelling and urban climate simulation to separate the influence of urban intrinsic factors from that of background climate, so as to focus on the impact of urbanization on the UHI effect. The urban climate model (Schubert et al., 2012) makes it possible to conduct controlled experiments to separate the influences from different driving factors. We develop a stochastic gravitational urban growth model that can generate 3D structures varying in size, morphology, compactness, and density gradient. The urban growth model provides detailed 3D structures that can be then parameterized into different urban development scenarios tailored for these experiments. We run several series of simulations with urban structures varying in properties like size, density and morphology, under the same forcing background climate. Based on the analysis of how the CUHI intensity varies in response to the variation of the considered urban factors, we propose a regression model to predict the CUHI intensity as a function of urban size, urban gross building volume, and a newly proposed indicator to capture the 3D urban morphology. The regression model can accurately predict the CUHI intensity under various urban development scenarios of Berlin area when compared to the numerically simulated CUHI intensity. Our regression model can be used to quantitatively assess the UHI intensity for different urban development scenarios of real-world cities that are heterogeneous in the configuration and composition regarding urban density.

We find a similar regression model that also works for predicting the SUHI intensity of 5000 European cities. By analysing the spatial variation of the regression coefficients through geographically weighted regression, we extend the model to a nonlinear one by integrating some climate parameters, such as the average of daily maximal temperature and latitude, to make it applicable across a range of background climates.

5.2 ANSWERS TO RESEARCH QUESTIONS

In this section, I will wrap up the knowledge gained through the efforts addressing each of our research questions, and discuss the respective implications.

5.2.1 *Research Question 1 (RQ1)*

The complex interactions among the myriads of contributing factors of UHI pose a great challenge for UHI attributing study. The modelling approach is the most viable and probably the only practicable solution to properly separate the influence of a specific urban factor from that of background climate and of other urban factors, so that the contribution from the very factor can be rigorously analysed.

But there are two fundamental obstacles to overcome:

1. Choosing an appropriate urban climate model,
2. Designing and running controlled simulation experiments.

To meet the challenges faced by the specific goal of this work, the urban climate model should properly resolve the 3D urban structure (during the parametrization process) with relatively high spatio-temporal resolution and coverage but with acceptable computational demand. Depending on the model chosen, efficiently controlled simulation experiments have to be designed with prepared 3D urban structures. Apart from that, the place and time for the reference simulation have to be carefully identified, taking into account the availability of in situ records for validating the model.

Considering the factors above, we chose the CCLM/DCEP model. The Double Canyon Effect Parametrization (DCEP) urban scheme takes parameterized 3D urban structure data as inputs, and it has been verified for its performance in some previous studies (Schubert et al., 2012; Schubert et al., 2013; Schubert et al., 2014; Schubert, 2013). We chose the Berlin area for the reference simulation and decided to take the condition during a typical heatwave event of a week in 2003 as the forcing climate.

Therefore, with the climate model, we build a laboratory environment within which we run urban climate simulations with different urban structures under the same driving climate. In this way, the influence of urban factors is isolated from that of background climate. To further harness the advantages of numerical modelling for factor separating, we feed the climate model with tailored urban canopy parameters (UCP) from generated 3D structures that resemble real-world cities.

The most effort was devoted to preparing the UCP datasets tailored for the controlled experiments. To this end, we updated a 2D gravitational model (Rybski et al., 2013) and proposed a 3D variant of

it. The stochastic urban growth model as described in Chapter. 2 has only two parameters but with enough flexibility to generate 3D structures varying in size, geometry, compactness, and density gradient. After comparing various characteristics, like fractal dimensions (Batty et al., 1994) (obtained through box-counting, area-perimeter scaling, area-population scaling, etc.) and radial gradient profile (Lemoy et al., 2020) of land use share and of population density, with properties of real cities in empirical studies, we found this model is capable of reproducing these characteristics.

By using the 3D stochastic gravitational model, we create a huge pool of 3D structures of more than 200000 3D structures that resemble real-world cities. Out of this pool, we select several groups of structures with the purpose of controlled experiments on urban size, density, and morphology, and then parameterize them into the input of the urban climate model. This makes it possible to further isolate the influence from a specific urban factor (i.e., fixing size and density but varying morphology). This innovative method enables us to systematically study the relationship between the UHI intensity and some key urban intrinsic properties through controlled experiments. It lays the basis on which we can quantitatively analyse the relationship, and generalize the obtained knowledge with a regression model.

5.2.2 *Research Question 2 (RQ2)*

Urban morphology has been shown to influence the SUHI effect in some studies (Zhang et al., 2012; Zhou et al., 2013; Oke et al., 2017; Zhou et al., 2017; Zhou et al., 2018; Liang et al., 2020; Liu et al., 2021b; Liu et al., 2021a). Many metrics have been used, for example, the fractal dimension and shape indices like area-perimeter ratio, elongation, anisometry, eccentricity. However, We find they do not provide good predicting indicators for the CUHI intensities. The reason might be that these metrics are all 2D indicators and do not capture the information on the 3rd dimension. This major challenge is to find a proper urban morphology indicator, yet there is no shortcut around a great number of tests.

We develop a hypotheses based on the reacting curve of CUHI intensity to each specific factor and on knowledge from the literature (Oke, 1981; Oke, 1982; Marciotto et al., 2010; Oke et al., 2017). After having tested hundreds of combinations of the hypotheses, we pick out the best one according to different statistical criteria. As a result, some factors were not included to balance the fitting performance and the model complexity. The hypothesis that each urban grid has a warming effect on others and this effect decays as a power function of the distance between them, leads to an efficient indicator that relates 3D urban morphology to CUHI intensity (namely term D in Eq. (3.4)). We name it Gravitational Urban Morphology (GUM)

indicator, and it captures the internal spatial configuration of urban density. Together with the urban size A and gross building volume S, we build a regression model ($\Delta T_a = c_1 \ln A + c_2 \ln S + c_3 D + c_4$, as in Eq. (3.4)) that can reproduce the CUHI intensity.

The empirically obtained regression model provides us helpful insights on how urban morphology, together with the urban size and gross building volume, influences the CUHI intensity. Our results (Fig. 3.2b) clearly show that urban size is not a primary determiner of the CUHI intensity. Instead, it is the urban density that fundamentally determines the CUHI intensity of a city (Schubert et al., 2013; Van Hove et al., 2015; Yin et al., 2018; Li et al., 2019b; Straka et al., 2019).

Regarding the influence of urban morphology, our model shows that sprawling development will lead to a better thermal environment when considering the entire urban area (note the parameter c_1 in Eq. (3.4) carries a negative sign). However, without some preconditions, it is difficult to clearly prefer one development design over another before their detailed 3D urban structures are available, or at least some factors are fixed. The main reason is that the factors in Eq. (3.4), in particular building height and street width, interact and impose limits on each other. Under the premise that the street canyon geometry is homogeneous over all urban sites, the term D clearly indicates that more compact urban clusters will lead to higher CUHI intensities. In addition to that, when the urban area A and the gross building volume S are controlled, some implications from a simplified situation can be derived:

- with homogeneous canyon geometry (building width, street width, building height throughout the city), cities with scattered/slender shapes will have smaller CUHI intensity,
- with homogeneous building density, cities with taller buildings (i.e., taller buildings instead of fatter buildings) experience smaller CUHI intensity,
- with homogeneous building density, less sealed surface (including building footprints, street, and other impervious surfaces) will lead to a smaller CUHI intensity.

The regression model as in Eq. (3.4), to some extent, crosses the scale hierarchy in regard to urban heat stress mitigation. By aggregating the complex interactions of vegetation fraction and canyon geometry at the neighbourhood scale grid cell into an impact at the city scale, the GUM proposed indicator captures the influence of internal urban density configuration on the UHI effect. It also clearly shows that city-scale UHI intensity cannot simply be scaled up from that of the neighbourhood scale, as nearby neighbourhoods also influence each other.

Most importantly, our model can serve as an assessment tool (Mills et al., 2010; Ng, 2012; Oke, 1984) that takes the 3D urban structures

of different urban development scenarios as inputs and enables the comparison between these scenarios in terms of heat stress mitigation on the city scale.

5.2.3 *Research Question 3 (RQ3)*

To answer this question, we investigate the summer daytime SUHI intensity of the 5,000 largest urban clusters in Europe. Due to the data availability problem, we reduce the complexity of the GUM index that worked well for predicting CUHI intensity (as in Eq. (3.4)) to a simplified version (as D in Eq. (4.3)) – in a way that the urban impervious surface fraction is treated like the 3rd dimension information. The simplified GUM index demonstrates the capability of effectively predicting the SUHI intensity. This agrees with previous studies on the contribution of both 2D urban compactness (Zhang et al., 2012; Zhou et al., 2017) and the urban density (Zhang et al., 2012; Li et al., 2018; Song et al., 2020) to SUHI intensity. Our results underline the importance of investigating cities from a 3D perspective, as 2D urban morphology neglects the influences from urban development within already urbanized areas (i.e., urban densification). Therefore, our model can serve as an effective predictor for SUHI intensity assessment in view of urbanization which usually involves both internal densification and outward sprawl.

Generally, the model can be interpreted similarly as in the answers to RQ2. Specifically, the GUM index indicates that cities with higher compactness and density tend to have stronger SUHI. However, specific implications regarding the influence of urban morphology on SUHI intensity could only be interpreted with some preconditions. For example, assuming the urban area A remains unchanged and the impervious surface fraction u is homogeneous within the urban cluster, the GUM index D degrades to an indicator that measures the compactness of the 2D urban morphology. Under this circumstance, it implies that from a 2D perspective cities with a rounder shape will have larger SUHI intensity whilst a more stretched shape leads to less surface warming (Zhou, 2017; Liu et al., 2021b).

To explore the influence of background climate factors, we then project all the cities into a 6-dimensioned climate space constructed using six background biophysical factors. The Geographically Weighted Regression (GWR) model is applied based on the constructed climate space to explore how the coefficients vary against different background climate factors. The GWR model shows further considerable improvement in its predictive ability. Investigating how the GWR coefficients vary against different background climate factors, we integrate some of the factors by replacing the coefficients in the multivariate linear model. This results in a nonlinear model that can capture some interactions between the urban factors and the background climate factors.

The nonlinear model, though with fewer parameters, outperforms multivariate linear models. It can be used for SUHI intensity assessment under different urbanization scenarios and climate backgrounds.

Results from Chapter 4 could provide useful information regarding urban heat reduction strategies, especially considering the ongoing rapid global urbanization and climate change. A better urban development plan that takes the influence of urban morphology into account could benefit the urban thermal environment. Moreover, measures for urban heat mitigation should also consider the predicted climate change. For instance in Table (C.2) we can see with same urban compactness (measured by GUM indicator D), cities in wetter area tend to experience higher SUHI intensity. As the climate context of a city may change in the future, heat mitigation strategies that are effective for the short term might become less beneficial in the long run (Fitzpatrick et al., 2019).

5.2.4 *Summary of research findings*

To sum up, this work investigates quantitatively how the UHI effect is influenced by several key city scale factors (e.g., urban size, density, morphology, background climates). We further advance our understanding of the formation of UHI by adding two major findings:

- The urban density and morphology are the major factors that determine the UHI intensity. In contrast to previous studies that link stronger UHI to larger city, we show that urban sprawl (the increase of urban size A) can lead to a UHI reduction if the urban density decreases.
- Compared with commonly used 2D shape indices, a quantitative 3D urban morphology indicator can better predict the intensity of both CUHI and SUHI.
- With same building volume increment, increasing urban density will lead to stronger UHI than expanding urban area.
- When city is constrained from sprawling outward, growing vertically will lead to smaller CUHI intensity increment than increasing building footprints.

Taking Berlin city as an example, our results show that doubling the gross building volume of the city by expanding urban area will lead to less than 0.1 °C increase in the CUHI intensity. However, by increasing the building height, the CUHI intensity will be around 0.4 °C stronger, whereas by increasing the fraction of building footprint, the CUHI intensity can be 0.8 °C stronger.

Our Gravitational Urban Morphology (GUM) indicator provides a more generalized quantitative urban morphology measurement. When density is homogeneous throughout the city, our 3D Gravitational Urban Morphology (GUM) indicator degrades to a 2D indicator, showing

that rounder and less stretched urban shape favours the urban heat accumulation, which is consistent with previous studies (Zhang et al., 2012; Zhou et al., 2017; Liu et al., 2021b).

Our work reiterates the essential role of urban density and morphology in shaping the urban thermal environment (Oke, 1984; Zhang et al., 2012; Zhou et al., 2017; Liu et al., 2021b). In addition, the results further our knowledge by demonstrating the influence of urban 3D morphology on the UHI effect. This underlines the importance of inspecting cities as a whole from a 3D perspective. While urban 3D morphology is an aggregated feature of small-scale urban elements, the influence it has on the city-scale UHI intensity cannot simply be scaled up from that of its neighbourhood-scale components. The spatial composition and configuration of urban elements both need to be captured when quantifying urban 3D morphology as nearby neighbourhoods also cast influence on each other. Our models can serve as useful UHI assessment tools for the quantitative comparison of urban intervention/development scenarios.

5.3 CONSTRAINTS AND CONSIDERATIONS

The results of this study provide valuable insights into the UHI effect and advance our understanding of the relationship between the UHI intensity and some major urban intrinsic properties. Despite the achievements, we also acknowledge a number of constraints and limitations of this study.

Firstly, some factors are simplified in the urban climate simulations. For example, building geometry, materials and properties of urban fabrics like walls and roofs, as well as street directions, are extremely heterogeneous in realistic cities, this cannot be resolved in our mesoscale urban climate model due to the simplification during urban canopy data parametrization. To date, in order to conduct sensitivity tests on a certain factor and separate the factor of interest from others, most local-scale 3D urban climate models reduce the complexity of the urban structure to idealized street canyons composed of cubic building elements (Martilli et al., 2002; Marciotto et al., 2010; Schubert et al., 2012; Theeuwes et al., 2014; Oke et al., 2017; Zhou et al., 2018). As the simple models may perform as well as the complex ones Best et al., 2015; Zhou, 2017, our choice of the model makes trade-offs between the computational requirement and the scale of our study. Simplification of these factors is necessary for running the model at the city scale and for isolating the factors we are interested in.

Secondly, also for simplification and to better separate the influences of the various factors, we do not consider anthropogenic heat in the simulations. The influence of anthropogenic heat release on nocturnal UHI effect should be relatively small during summer according to studies on other temperate cities (Taha, 1997; Runnalls et al., 2000;

Shahmohamadi et al., 2011; Bohnenstengel et al., 2014; Oke et al., 2017). Moreover, during the night, anthropogenic heat release from cooling should be negligible as the majority of households in Berlin do not use air conditioning so far. However, for cities or scenarios where cooling equipment is widely operated during hot summer, UHI intensity can be increased by more than 1 °C (Li et al., 2014; Salamanca et al., 2014; De Munck et al., 2013). A model that integrates the influence of anthropogenic heat will be helpful for more accurate UHI prediction for cities where cooling devices are widely used.

In addition, background climate (Runnalls et al., 2000; Oke, 1987; Oke et al., 2017) plays an important role in determining the UHI intensity, which means extrapolating knowledge from one area to another should be done with great caution, especially between areas with distinct climates. To apply our regression model (as Eq. (3.4)) to another city for the CUHI assessment, one would need to derive the coefficients of the regression again. This hampers the fast application of our CUHI predicting model, especially for those without expertise in running numerical climate simulations. As for our regression model for SUHI, the uncertainty of the predicted SUHI intensities can be high if the background climate differs from that of the studied cities. Therefore, a bigger sample set from a large range of climate backgrounds will improve the generality of the model.

5.4 FUTURE WORK

Looking ahead, there are several directions in which this research could be extended. One possibility is to explore the linkage between the Gravitational Urban Morphology (GUM) indicator and some more intuitive morphology indicators, to gain a more intuitive understanding of this quantitative indicator. Another possibility is to extend our UHI predicting model into a more generalized one with the background climate more comprehensively integrated.

5.4.1 *A better understanding of the GUM indicator*

Despite the capability of our proposed models in UHI intensity prediction, the complex form of the Gravitational Urban Morphology (GUM) indicator D makes it rather difficult to draw an intuitive expression from the number, especially considering the great heterogeneity that cities have in their density. Future work that links the quantity D to factors like urban fractality (Batty et al., 1994; Batty et al., 1989; Zhou et al., 2017), urban centrality/poly-centrism (Stone et al., 2010; Batty, 2013), anisometry (Zhou et al., 2017), and urban gradient profile in built density will further our understanding of the influence of the urban form on the UHI effect.

Besides, instead of being limited to a function of only urban impervious surface fraction u, the weight function used in calculating the GUM index D for predicting SUHI may work better in different forms. Many other street canyon morphology indices like aspect ratio, building density, water surface fraction, and vegetation fraction can also modulate the SUHI effect at the local scale (Zhang et al., 2012; Mathew et al., 2017; Song et al., 2020; Liu et al., 2021a). This is rather challenging due to the availability of fine-scale 3D building structure datasets. Things are changing recently as some datasets with global coverage are becoming available with the help of machine learning techniques (Li et al., 2020a; Biljecki et al., 2022; Li et al., 2022). Future efforts in this regard would be helpful for broadening our understanding.

5.4.2 *Generalized UHI predicting model integrating climate factor*

Urbanization and climate change are widely recognized as two of the most pressing challenges for sustainable development (Baer et al., 2016; Zhou, 2017; UNEP, 2021). Considering that the two are closely intertwined, a holistic and integrated approach is essential to address them (UN-Habitat, 2016; Oke et al., 2017; UNEP et al., 2021; UNEP, 2021). A more generalized UHI predicting model that integrates climate factors, when combine with models that predict future urban growth (Glockmann et al., 2022; Rybski et al., 2021b), can support long term urban heat mitigation decisions.

The gap of our CUHI predicting models in their application across climate backgrounds (as discussed in section 5.3) suggests the extension of the model with the background climate integrated. This challenge asks for further comprehensive and quantitative studies on how the background climate influence plays a role in controlling the UHI effect jointly with other factors.

The benefits brought by a more generalized UHI predicting model would be twofold:

- Under the current climate, it provides a readily usable UHI assessment tool for fast applications on cities with various background climates.
- For future scenarios, it enables UHI assessment in view of urbanization under the context of climate change.

Potentially, the SUHI analysis in this work can be extended to a global scale, so that the influence from a much wider range of climate backgrounds can be studied. This requires high-resolution 3D urban structure and background climate data with global coverage (Biljecki et al., 2022; Li et al., 2022; Zhou et al., 2022; Zhang et al., 2022a; Zhang et al., 2022b; Zhao et al., 2022), which are increasingly available in the big earth data era. Regarding CUHI assessment, the simulation experiment in our work can be repeatedly driven by different weather

conditions, and ideally, with extended temporal coverage. This demands huge computational resources, carefully designed experiments with properly selected representative driving data could help to avoid unnecessary simulations.

A

APPENDIX CHAPTER 2

A.1 SUPPLEMENTARY NOTES FOR CHAPTER 2

Here we want to complement the numerical analysis on our stochastic urban growth model proposed in Chapter 2, by economics arguments employing travel costs as well as housing rent determined by supply and demand.

A.1.1 *Economics Reasoning of the population gradient*

We want to motivate Eq. (2.4), i.e. propose a setting under which the density gradient goes as

$$D(r) \sim r^{-\alpha} \tag{A.1}$$

whereas $\alpha \approx 2$. The population density is given by population per area. The area of concentric rings is proportional to the distance from the center, i.e. $\sim 2\pi r$. Then $D(r) = \frac{S(r)}{A(r)} \sim \frac{S(r)}{r}$ and the population follows $S(r) \sim r^{-\alpha+1}$. If we normalize to the total population, then we have a probability density

$$p(r) \sim r^{-\alpha+1}\,. \tag{A.2}$$

We begin with the common approach according to which the commodity Z is given by the wages W minus the housing rent R and the transportation costs T, see e.g. (Barthelemy, 2016, Ch. 3.3), i.e.

$$Z = W - R - T\,, \tag{A.3}$$

which is maximized by minimizing expenses

$$\max(Z) = W - \min(R + T)\,. \tag{A.4}$$

In the mono-centric case it is common sense that the rents decrease further away from the city center but the transportation costs increase. We assume power-law relations

$$R = a\, r^{-\rho} \tag{A.5}$$

$$T = b\, r^{\tau}\,, \tag{A.6}$$

with the distance r from the center and $\rho, \tau > 0$. The power-law rent profile is motivated below, for the power-law transportation costs see e.g. (Fabinger, 2012, Sec. 1.4.3) and references therein. Delloye et al. (2018) use linear transportation costs ($\tau = 1$).

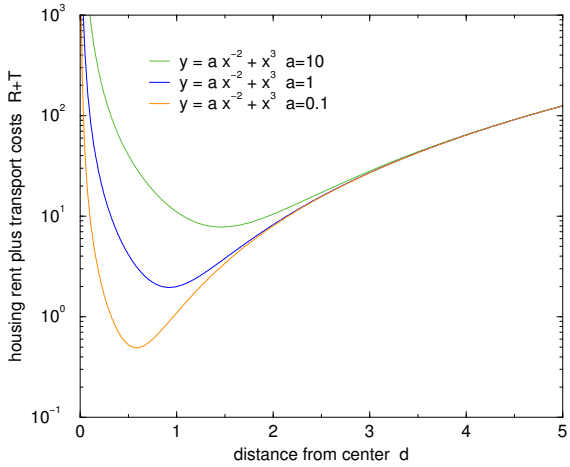

Figure A.1: Illustration of the sum of housing rent and transportation costs as well as the influence of the weight a. The values $\rho = 2$, $\tau = 3$, and $b = 1$ have been used exemplary. With decreasing a the minimum moves towards the center.

In order to find the optimal distance to the center, the derivative of $R + T$ needs to be zero, i.e.

$$r_{\text{opt}} = \left(\frac{\rho a}{\tau b}\right)^{1/(\rho+\tau)} . \tag{A.7}$$

By summing R with T we are essentially comparing apples with oranges. However, the prefactors a and b determine the weights they have relative to each other. Certainly, for wealthy people the rent becomes less of an issue and the weight should be smaller while transportation is similar for everyone [people spend 20 % to 30 % of their time commuting (Kahneman et al., 2006)]. We assume $a \sim W^{-1}$, $b = \text{const}$ (see Fig. A.1) and obtain

$$r_{\text{opt}} \sim W^{-1/(\rho+\tau)} . \tag{A.8}$$

Wealthier people can afford living close to the city center while low income population is pushed outward.

Further, we take the power-law income or wealth distribution

$$p(W) \sim W^{-\zeta} \tag{A.9}$$

with $\zeta \approx 2.5$ [$\zeta_{\text{USA}} \simeq 2.4$ (Levy et al., 1997; Brzezinski, 2014)]. The exponent ζ is also related to the Gini coefficient via $\zeta = \frac{1}{2G} + \frac{3}{2}$ (Pfähler, 1985). Typical values are between $G = 0.65$ and $G = 0.80$ corresponding to $\zeta \simeq 2.27$ and $\zeta \simeq 2.13$, respectively.

If two quantities A and B follow power-law distributions with pdfs $p(A) \sim A^{-\zeta_A}$ and $p(B) \sim B^{-\zeta_B}$, then the transformation $B \sim A^{\beta}$ with $\beta = (\zeta_A - 1)/(\zeta_B - 1)$ translates one into the other (Gomez-Lievano et al., 2012). Comparison leads to $\zeta_A = \zeta$, $\zeta_B = \alpha - 1$, and

$$\frac{-1}{\rho + \tau} = \frac{\zeta - 1}{\alpha - 2} . \tag{A.10}$$

The lhs is negative and since $\zeta \gg 1$ the rhs can only become negative if $\alpha < 2$. At $\alpha = 2$ a transition occurs and for $\alpha > 2$ the mono-centric assumption does not hold. This is consistent with the transition at $\gamma = 2.5$ in Eq. (2.8). From $\alpha = 2 - (\zeta - 1)(\rho + \tau)$ it can be seen that only small values of τ and ρ lead to α close to 2.

As a critical remark, we need to add that it is not a surprise to obtain a power-law (or a relation between exponents) when the derivation itself is based on power-laws. However, in economics power-laws are theoretically understood and empirically established (Gabaix, 2016).

A.1.2 *Housing rent*

Here we want to motivate Eq. (A.5) and the exponent ρ. The housing rent is determined by supply and demand. We postulate that the number of people willing to pay rent larger than R decreases as a power-law with R

$$P_{\mathrm{D}}(X \geq R) \simeq R^{-\epsilon_{\mathrm{D}}} . \tag{A.11}$$

Analogously, the number of people willing to sell property or rent it out for a price lower than R decreases as a power-law with R

$$P_{\mathrm{S}}(X \leq R) \simeq 1 - R^{-\epsilon_{\mathrm{S}}} . \tag{A.12}$$

The market price is then given by the price where both curves cross each other

$$a_{\mathrm{D}} P_{\mathrm{D}}(X \geq R_\times) = a_{\mathrm{S}} P_{\mathrm{S}}(X \leq R_\times) \tag{A.13}$$

$$a_{\mathrm{D}} R_\times^{-\epsilon_{\mathrm{D}}} + a_{\mathrm{S}} R_\times^{-\epsilon_{\mathrm{S}}} = a_{\mathrm{S}} , \tag{A.14}$$

where the factors a_{D} and a_{S} are required to adjust for the amount and convert the cdfs into cumulative frequency distributions. Increasing availability should decrease the price and increasing demand should increase the price. We assume $a_{\mathrm{D}} \sim 1/r$ and $a_{\mathrm{S}} \sim r$ leading to $1/r\, R_\times^{-\epsilon_{\mathrm{D}}} + r R_\times^{-\epsilon_{\mathrm{S}}} \sim r$. For large r the second term dominates, implying $R_\times = \text{const}$. Thus, large supply leads to a (low) price that is independent of the location. For small r the first term dominates, leading to

$$R_\times \sim r^{-2/\epsilon_{\mathrm{D}}} , \tag{A.15}$$

i.e. $\rho = 2/\epsilon_{\mathrm{D}}$. The price is dominated by the demand.

Linearity should work if we consider the area. In case of living space/apartments another exponent might be necessary to take changes of density into account, i.e. $a_{\mathrm{D}} \sim r^{-\delta_{\mathrm{D}}}$ and $a_{\mathrm{S}} \sim r^{\delta_{\mathrm{S}}}$. With the same reasoning as before, we then obtain $R_\times \sim r^{-(\delta_{\mathrm{S}} + \delta_{\mathrm{D}})/\epsilon_{\mathrm{D}}}$. In particular, if we consider Eq. (A.2) and $\delta_{\mathrm{D}} = \delta_{\mathrm{S}} = \alpha - 1$, then $\rho = (2\alpha - 2)/\epsilon_{\mathrm{D}}$. For $\alpha \approx 2$ we have $\rho \approx 2/\epsilon_{\mathrm{D}}$.

B

APPENDIX CHAPTER 3

B.1 SUPPLEMENTARY NOTES FOR CHAPTER 3

B.1.1 *Introduction of street canyon width and aspect ratio*

If we include B_i, H_i, λ_i as building footprint area, average building height, and street canyon aspect ratio, respectively, for grid cell i (Appendix B.3, Table B.3), then they are related by building volume $w_i = B_i H_i$, street canyon aspect ratio $\lambda_i = H_i / Y_i$, and we can further rewrite D in Eq. (3.4) as:

$$D = \frac{1}{N} \sum_{j}^{N} \sum_{i \neq j}^{N} (f_{u_i} B_i \lambda_i)^{1/2} d_{ij}^{-3/2}, \tag{B.1}$$

Fitting Eq. (B.1) leads to identical to those of Eq. (3.4). This implies that for a specific city with preset area A and gross building volume S, larger sealed surface fraction, building footprint area and street canyon aspect ratio tend to intensify the canopy layer urban heat island (CUHI) effect.

B.2 SUPPLEMENTARY TABLES FOR CHAPTER 3

	Lind.	Alex.	Tegel	Temp.	Dahlem	Schön.
ME	-0.19	-0.51	-0.77	0.42	0.77	0.58
MAE	0.77	0.74	1.04	1.02	1.45	0.81
RMSE	0.94	0.93	1.26	1.27	1.85	1.07

Table B.1: 2m air temperature [K] statistics of the reference run (see "Methods" section of Chapter 3) against observational data.

pattern	number	size A (km^2)	fractal dimension	extra information
p 1	3	64, 512, 4096	1.89	Sierpinski Carpet
p 2	3	25, 125, 625	1.46	Vicsek fractal
p 3	5	102, 256, 625, 1026, 4096	$\approx$1.71 [1]	DLA [2]cluster
p 4	3	16, 64, 256	1.26	Cantor Dust
p 5	3	25, 125, 625	1.46	diagonal Vicsek fractal
p 6	3	16, 64, 256	1.26	diagonal Cantor Dust
p 7	8	25, 129, 621, 997, 1505, 2001, 3001, 4001	2 (small scales)	circle
p 8	2	624, 626	$\approx$1.46*, 1.72*	gravitational model
p 9	5	28, 124, 624, 1004, 2004	1 (small scales)	ring
p 10	7	225, 225, 255, 225, 225, 225, 225	-	space between neighbour cells: 0, 1, 2, 3, 4, 6, 8

Table B.2: Information about the spatial patterns for which the canopy layer urban heat island (CUHI) intensities have been simulated and fitted by Eq. (3.3). We list the abbreviation, the number of realizations, the size, the fractal dimension (* indicate measured values), and additional information. The patterns are illustrated in Fig. B.3.

1 Batty et al., 1994
2 Witten Jr. et al., 1981; Fotheringham et al., 1989; Batty et al., 1989; Batty et al., 1994; Batty, 2013
3 Li et al., 2021a

notation	meaning	unit
S	city gross building volume	km^3
A	urban area	km^2
ΔT_a	canopy layer urban heat island intensity	K
w_i	building volume of grid i	km^3
d_{ij}	distance between grid i, j	km
N	number of urban grid cells	-
v_i	value of cell i in gravitational model output	-
f_u	urban surface fraction	-
f_b	share of building plan area in urban surface	-
W_b	building width	km *
Y	street canyon width	km *
$\bar{v}$	average building height	storey
A_{grd}	area of simulation grid cell	km^2
H_f	height per floor, 0.003km *	-
γ	parameter in the gravitational model	-
B_i	building plan area in grid cell i	km^2
H_i	average building height in grid cell i	km *
λ_i	urban street canyon aspect ratio in grid cell i	-

Table B.3: Notation table. *) We use km instead of m because otherwise the parameters of Eq. (3.4) would become very small.

Exp. series	gravitational clusters	spatial patterns	canyon width tests
UCP data-set	set 1, 2, 3, 4	set 5	set 6
number of simulation	50	42	50
description	Fig. B.1	Fig. B.3	5 from set 1, 5 from set 3
urban fraction f_u	0 - 1	0.53	0 - 1
average building height [m]	3 - 90	8.63	3 - 90
street canyon Y [m]	20	15	10,15,20,25,30
building width W_b [m]	15	20	$W_b/Y = 15/20$
regression applied	Eq. (3.2), (3.4), (B.1)	Eq. (3.3)	Eq. (3.4), (B.1)

Table B.4: Information about urban canopy parameters (UCP) parameters taken in different simulations.

B.3 SUPPLEMENTARY FIGURES FOR CHAPTER 3

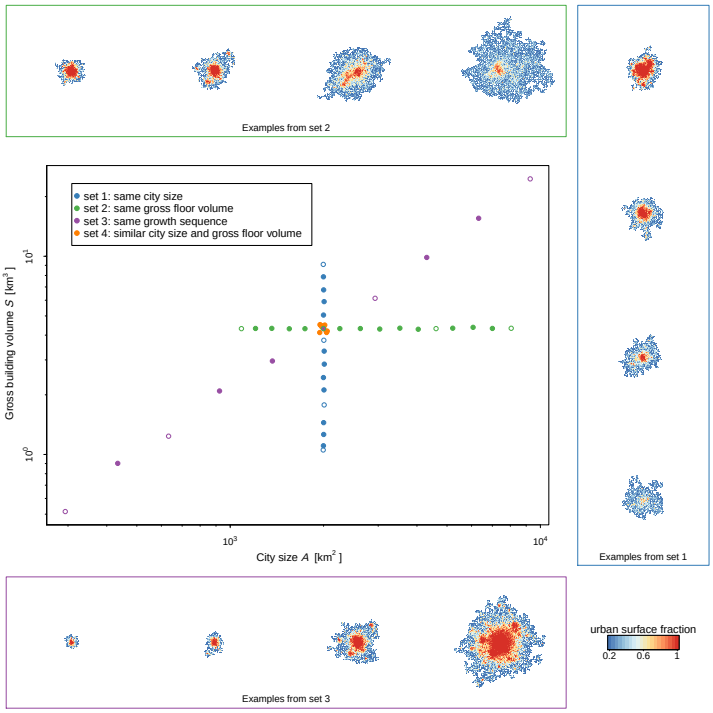

Figure B.1: Examples of analysed urban clusters. From the large number of previously generated urban clusters (Li et al., 2021a), 50 have been selected which are illustrated here. The clusters are organized into sets according to the criteria they have been chosen by, i.e. same area (set 1, blue), same gross building volume (set 2, green), same growth sequence (set 3, violet), and similar size and similar gross building volume (set 4, orange), see details in the "Methods" section of Chapter 3. The surrounding panels display 4 examples each and the colour scale indicates the urban fraction in each urban site.

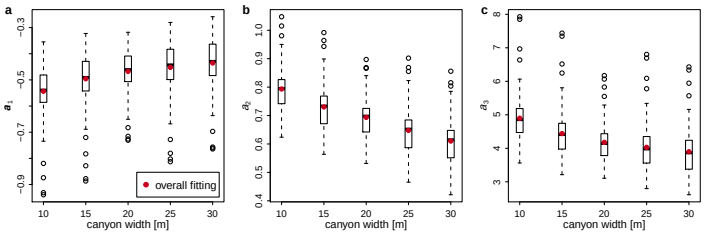

Figure B.2: Parameters from Eq. (3.2) depending on the canyon width. In order to assess the influence of the canyon width on the pre-factors in Eq. (3.2) we run the urban climate simulations for 10 generated urban clusters (see Fig. B.1 and "Methods" section of Chapter 3) and repeat for different canyon widths between 10 m and 30 m. The panels show box plots of the parameters vs. the canyon width, i.e. for a_1 in **a**, for a_2 in **b**, and for a_3 in **c**. The spreading is obtained from bootstrapping (200 repetitions) and the red dots represent the estimated parameters without bootstrapping.

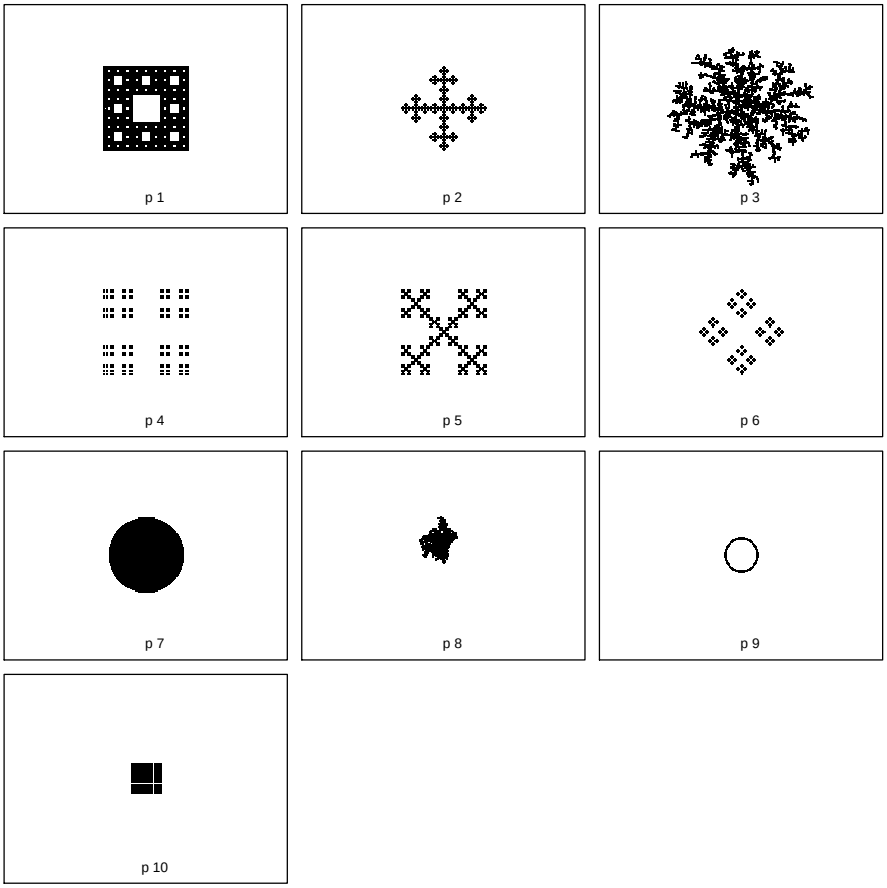

Figure B.3: Examples of analysed spatial patterns in set 5. Different sizes of these patterns were used for the urban climate simulations. Details on the patterns are provided in Table B.2. The building volume in each pixel is set constant throughout the patterns. Pattern 2 resembles the Ville Contemporaine as envisioned by Le Corbusier; pattern 9 resembles the Apple Park in Cupertino, California.

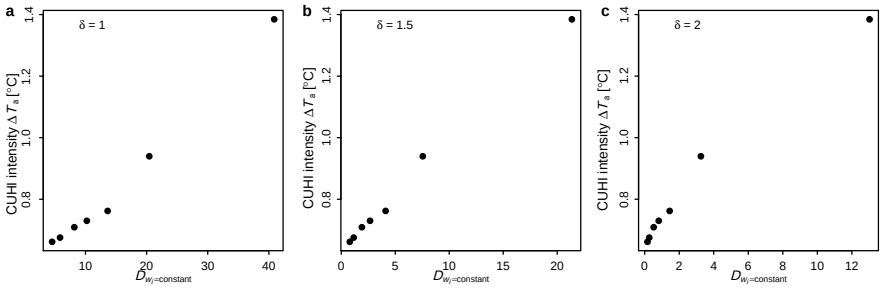

Figure B.4: Estimation of exponent δ in Eq. (3.3). For pattern 10 (see Extended Data Fig. B.3) with variable spacing and constant size we plot the UHI intensity ΔT_a as a function of $D_{w_i=\mathrm{const.}} = \frac{1}{N}\sum\sum_{i,j}^{N,N} d_{i,j}^{-\delta}$ for $\delta = 1$ (panel **a**), $\delta = 1.5$ (panel **b**), and $\delta = 2$ (panel **c**). For $\delta = 1.5$ we find an approximately linear relation implying that D linearly relates to the canopy layer urban heat island intensity given the constant number of urban sites and only capturing the spatial organization.

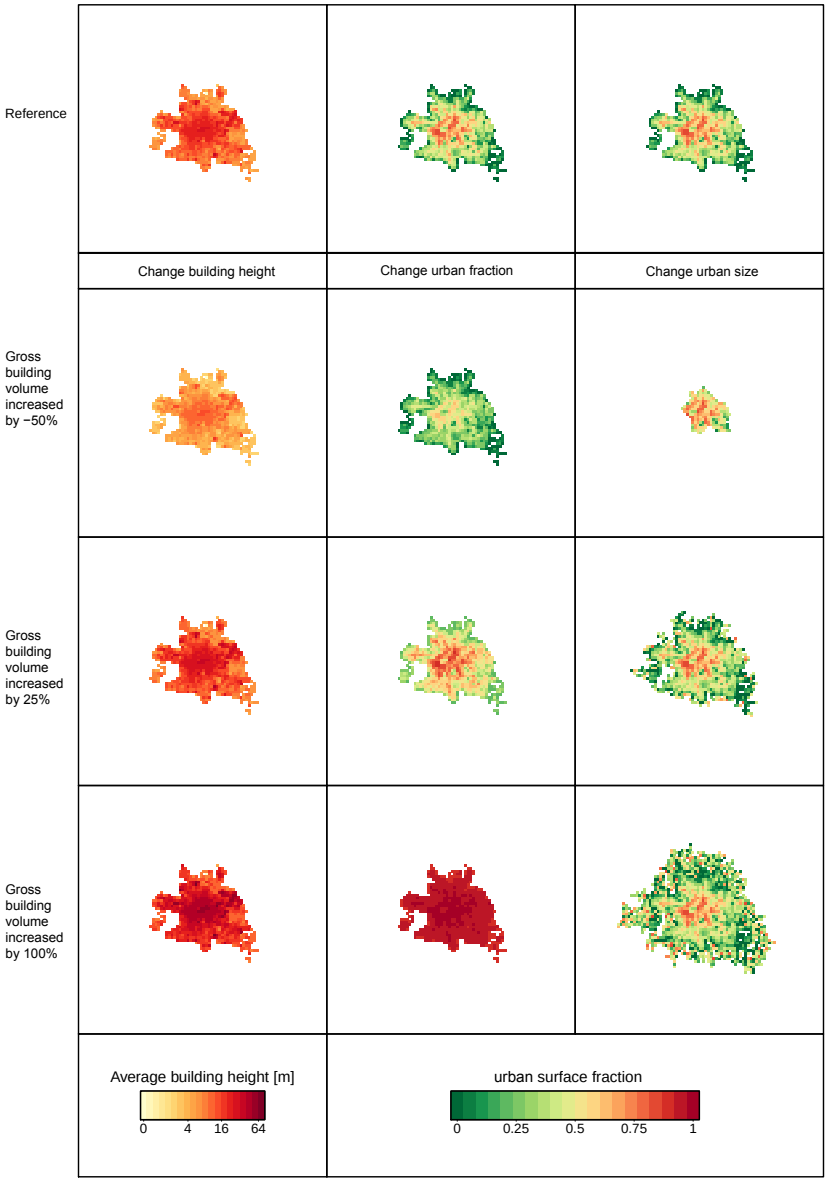

Figure B.5: Visualization of some urban canopy parameters (UCP) datasets from different urbanization scenarios based on the UCP dataset of Berlin. The first column shows the average building height map, the second and third show the urban surface fraction maps, respectively. Panels in the first row are from real UCP dataset of Berlin used in the reference run, whereas Panels in other rows are from UCP datasets where gross building volume is increased by -50%, +25%, and +100%.

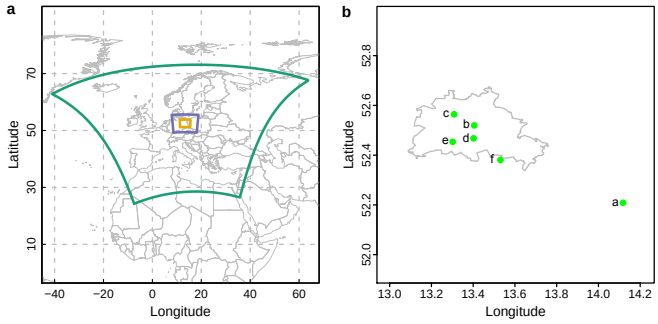

Figure B.6: Climate simulation domains and location of weather stations. **a,** Nested domains with resolution of 0.165° (aqua green), 0.025° (purple), 0.009° (orange). **b,** Green points indicate locations of weather stations, a) Lindenberg, b) Alexanderplatz, c) Tegel, d) Tempelhof, e) Dahlem, f) Schönefeld, grey line is the administrative boundary of Berlin city.

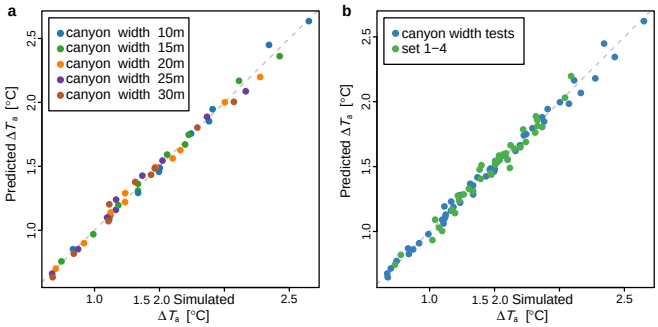

Figure B.7: Fitting performances of Eq. (B.1). **a**, Fitting for varying canyon width tests (see "Methods" section of Chapter 3). **b**, Fitting for both canyon width tests and simulations with clusters in Extended Data Fig. B.1.

C

APPENDIX CHAPTER 4

C.1 SUPPLEMENTARY NOTES FOR CHAPTER 4

To examine influence of water proximity on canopy layer urban heat island (CUHI), we plot the spatial distribution of the residuals from the Geographically Weighted Regression (GWR) model as in Fig. C.12. Most of the cities with large errors ($|\epsilon| > 1$) of the GWR regression are located at the coast of the sea or a big lake. This might be due to the urban-boundary difference in received cooling effect of the breeze from large water bodies. This difference could be influenced by wind direction and the proximity to water bodies. The influence from wind speed and urban-boundary difference in water surface share can be captured by the GWR model, so we assume the cooling effect from nearby water bodies not considered in the regression model can explain large predicting errors, as the cooling effect of water bodies has been found to decay along the distance (Su et al., 2012; Du et al., 2016; Wang et al., 2019).

As an attempt to quantify the difference in water body proximity between urban area and boundary area, for each city we calculate the ratio of neighbouring water cells for both urban area and boundary area (namely the number of water cells adjacent to urban cells divided by the number of urban cells, and the number of water cells adjacent to boundary area cells divided by the number of boundary area cells, respectively) and take the difference in the ratios as an indicator. From the supplementary Fig. C.13 we can see that the majority of the cities with large negative prediction errors ($\Delta T_s - \Delta T_{s,predicted} < -1°C$) have a larger ratio of neighbouring water cells for the boundary area than for the urban area and a majority of the cities with large positive prediction errors ($\Delta T_s - \Delta T_{s,predicted} > 1°C$) have a larger ratio of neighbouring water cells of the urban area than of the boundary area. However, Fig. C.13 also shows that a large difference in ratio of neighbouring water cells does not necessarily lead to a large prediction error. This means that a better indicator is needed to quantify the influence of water proximity on SUHI.

We explore the influence of water bodies rather qualitatively. In Fig. C.12(d-i) we show the maps of some example urban clusters as well as their boundary areas. In the panels (d) and (e) the GWR prediction error is larger than 1 °C, which means the SUHI intensity is larger than the GWR model predicted. It might be due to their boundary areas which are relatively close to water compared to the urban clusters. For example, in panels (f)-(i) the predicted SUHI intensity

is much larger than observed, as the GWR prediction error is always smaller than -1°C. A possible reason is that urban clusters are much closer to water bodies than the corresponding boundary area, thus the urban clusters are exposed to more cooling. We find that similar to the examples in Fig. C.12(f)-(i), most of the cities spreading in a strip shape along the coast of the sea or a lake, tend to have a larger negative prediction error. Whereas only a few exceptions exist, which might be because the influence from topography or the summer prevailing wind direction that does not favour the penetration of cool breeze into urban area.

C.2 SUPPLEMENTARY TABLES FOR CHAPTER 4

	ΔT_s	$\ln A$	D	$U_{\Delta Veg}$	$U_{\Delta Wat}$	$U_{\Delta Ele}$	B_{Pre}	B_{Tmx}	B_{Lat}	B_{Veg}	B_{Ele}	B_{Win}
Δ_T		0.50	0.64	−0.53	−0.26	−0.16	0.34	−0.32	0.28	0.42	−0.04	0.06
$\ln A$	0.50		0.74	−0.26	0.003	−0.21	−0.02	−0.04	0.02	0.02	−0.05	0.08
D	0.64	0.74		−0.50	−0.14	−0.05	−0.10	−0.07	0.01	−0.07	−0.13	0.26
$U_{\Delta Veg}$	−0.53	−0.26	−0.50		−0.15	0.12	−0.18	0.27	−0.12	−0.47	0.16	−0.24
$U_{\Delta Wat}$	−0.26	0.003	−0.14	−0.15		−0.13	−0.08	0.003	0.06	−0.09	−0.15	−0.002
$U_{\Delta Ele}$	−0.16	−0.21	−0.05	0.12	−0.13		−0.07	−0.07	0.16	−0.09	−0.35	0.21
B_{Pre}	0.34	−0.02	−0.10	−0.18	−0.08	−0.07		−0.53	0.55	0.73	0.06	−0.11
B_{Tmx}	−0.32	−0.04	−0.07	0.27	0.003	−0.07	−0.53		−0.84	−0.59	0.21	−0.46
B_{Lat}	0.28	0.02	0.01	−0.12	0.06	0.16	0.55	−0.84		0.48	−0.32	0.24
B_{Veg}	0.42	0.02	−0.07	−0.47	−0.09	−0.09	0.73	−0.59	0.48		−0.07	0.04
B_{Ele}	−0.04	−0.05	−0.13	0.16	−0.15	−0.35	0.06	0.21	−0.32	−0.07		−0.44
B_{Win}	0.06	0.08	0.26	−0.24	−0.002	0.21	−0.11	−0.46	0.24	0.04	−0.44	

Table C.1: Pearson correlation coefficient between all the used variables.

	B_{Pre}	B_{Tmx}	B_{Lat}	B_{Veg}	B_{Ele}	B_{Win}
Intercept	-0.61	0.64	-0.59	-0.71	0.43	-0.21
Coef. D	0.74	-0.84	0.78	0.80	-0.33	0.32
Coef. $\ln A$	-0.48	0.84	-0.74	-0.57	0.41	-0.64
Coef. $U_{\Delta Wat}$	0.49	-0.66	0.66	0.49	-0.04	0.15
Coef. $U_{\Delta Veg}$	0.76	-0.83	0.77	0.80	-0.31	0.29
Coef. $U_{\Delta Ele}$	-0.56	0.49	-0.53	-0.54	-0.09	0.02

Table C.2: Pearson correlation coefficient between the Geographically Weighted Regression (GWR) coefficients and the background biophysical factors.

C.3 SUPPLEMENTARY FIGURES FOR CHAPTER 4

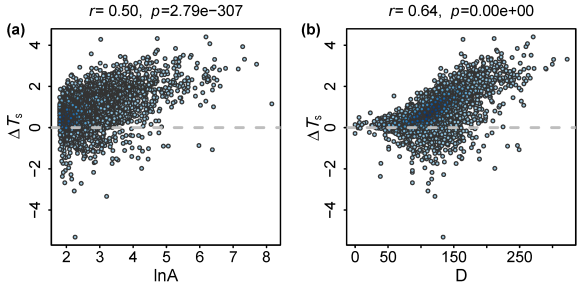

Figure C.1: Pearson correlation coefficient between (a) ΔT_s and $\ln A$, (b) ΔT_s and D.

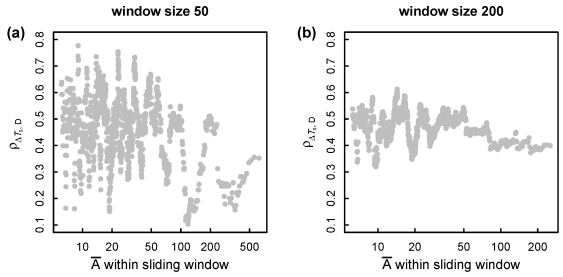

Figure C.2: Pearson correlation coefficient between the ΔT_s and D of the sample set selected by a sliding window, plotted against the average area A of the sample set. The sample sets are selected using a window size (number of cities within each sample set) of 50 (panel **a**) and 200 (panel **b**) according to their ranking in area, so that cities within one sample set have a similar value of area A, the smaller the window size, the closer the area values.

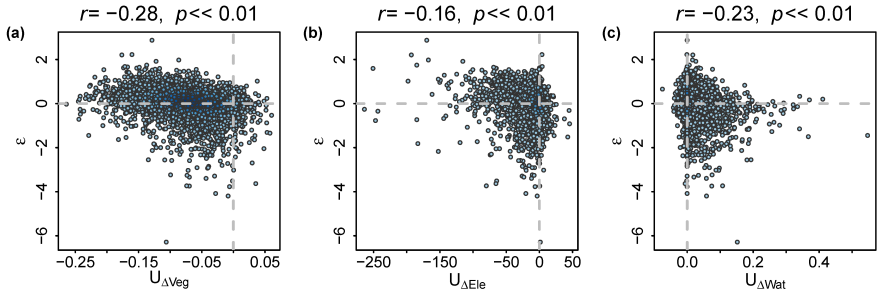

Figure C.3: Residuals from regression of Eq. (4.3) against $U_{\Delta Wat}$, $U_{\Delta Veg}$ and $U_{\Delta Ele}$.

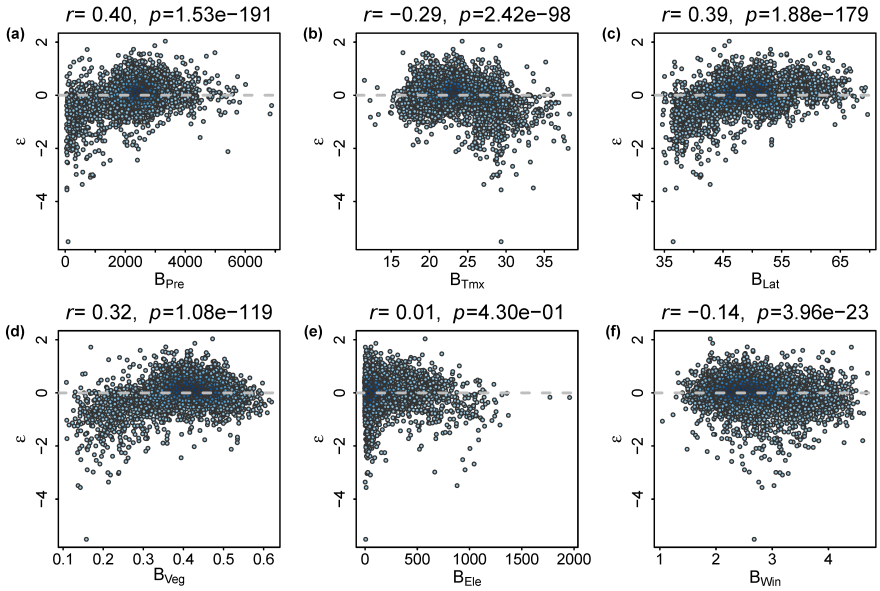

Figure C.4: Residuals from fitting of Eq. (4.4) against background biophysical factors. (a) summer precipitation B_{Pre}. (b) summer mean maximum temperature B_{Tmx}. (c) latitude B_{Lat}. (d) summer EVI of boundary area B_{veg}. (e) elevation B_{Ele}. (f) summer 10 m wind speed B_{Win}.

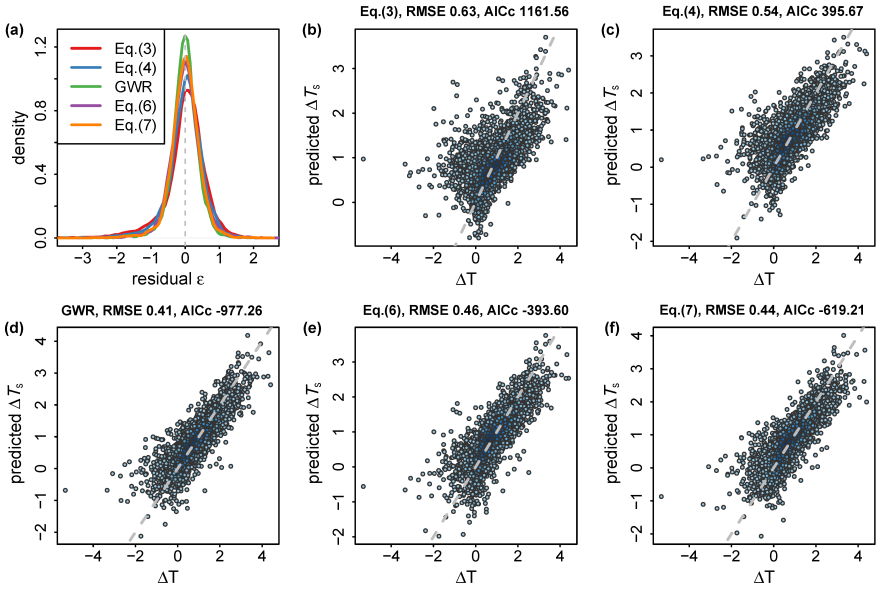

Figure C.5: Comparison of residuals from fitting of Eq. (4.3), Eq. (4.4), GWR, Eq. (4.6), Eq. (4.7).

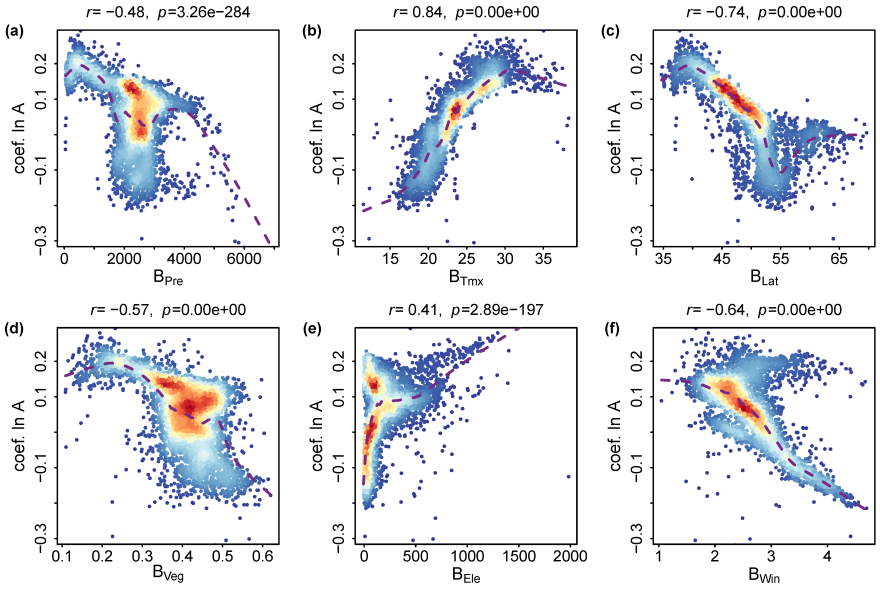

Figure C.6: Coefficient of ln A from Geographically Weighted Regression (GWR) against the background biophysical factors.

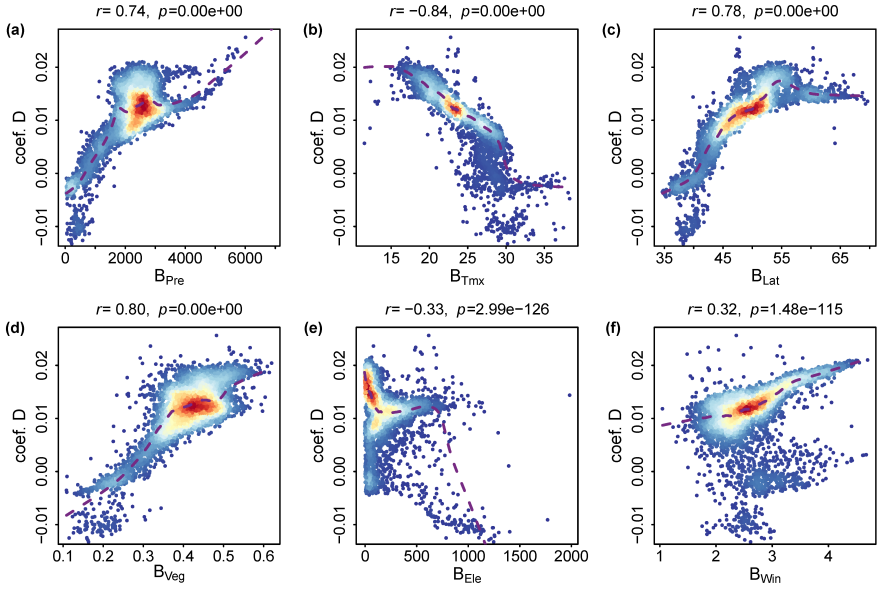

Figure C.7: Coefficient of D from GWR against the background biophysical factors.

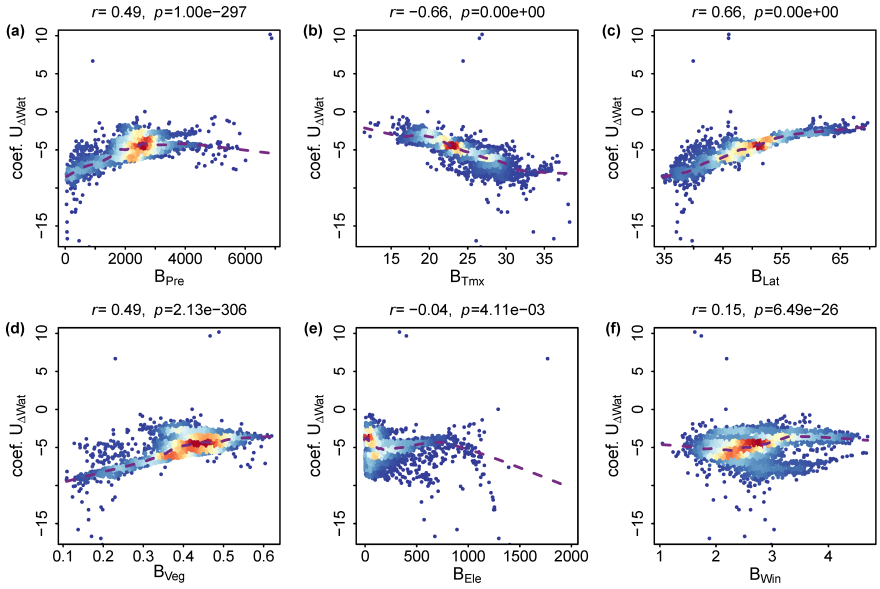

Figure C.8: Coefficient of $U_{\Delta Wat}$ from GWR against the background biophysical factors.

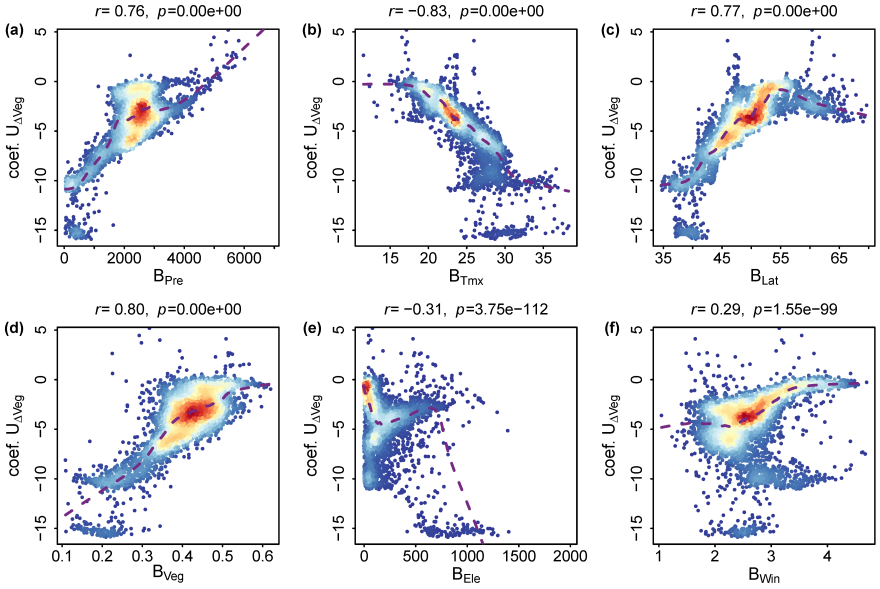

Figure C.9: Coefficient of $U_{\Delta Veg}$ from GWR against the background biophysical factors.

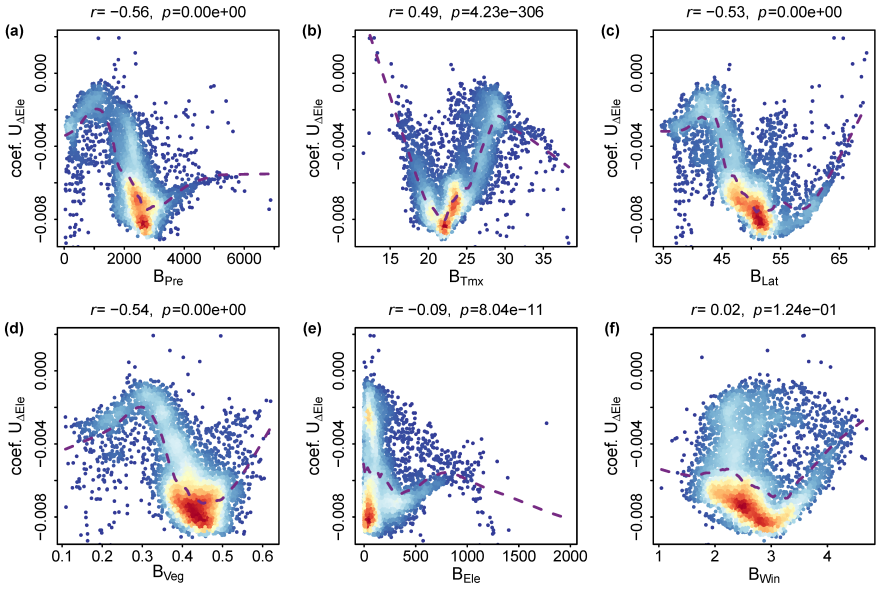

Figure C.10: Coefficient of $U_{\Delta Ele}$ from GWR against the background biophysical factors.

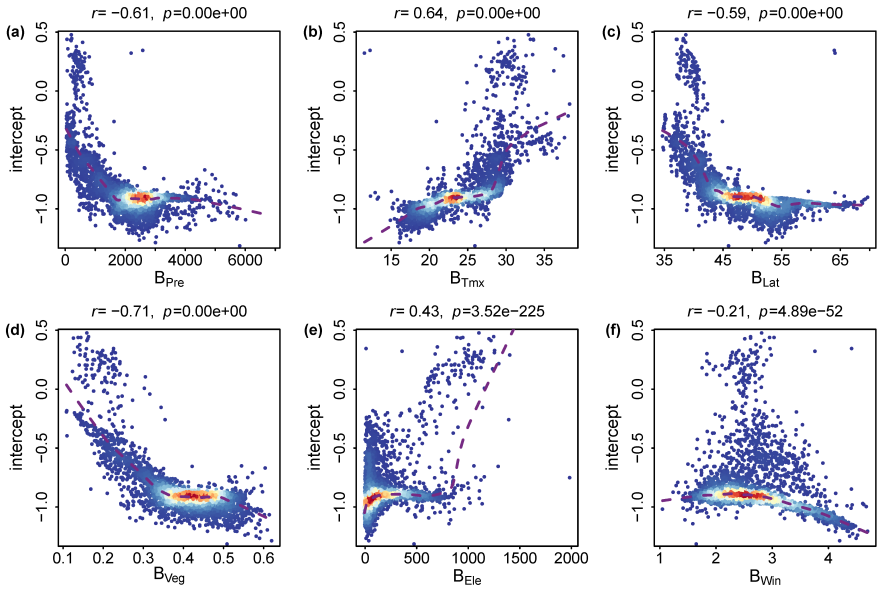

Figure C.11: Intercept from GWR against the background biophysical factors.

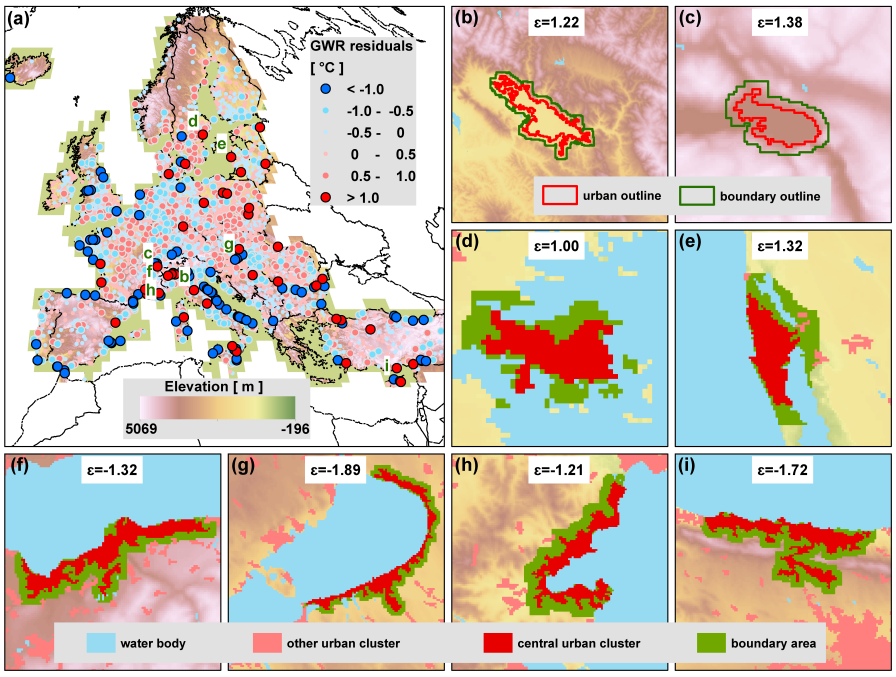

Figure C.12: Examples with large residuals (observed ΔT_s - model predicted ΔT_s) of the GWR model. (a) the spatial distribution of the residuals overlapping on the elevation map. (b-e) examples of cities with very large positive residual (ϵ). (f-i) examples of cities with very large negative residual.

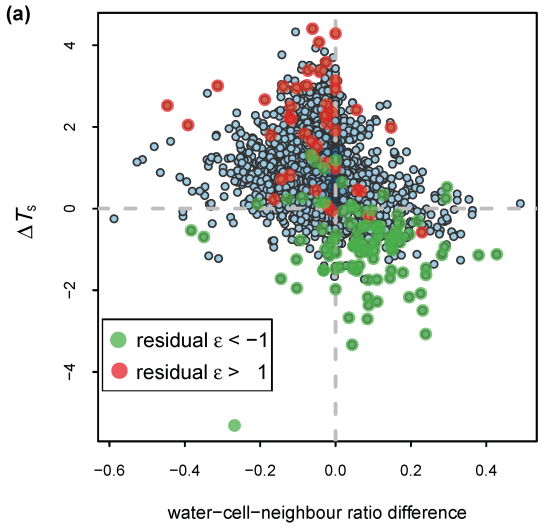

Figure C.13: ΔT_s plotted against the water-cell-neighbour ratio difference between urban area and boundary area. The water-cell-neighbour ratio is calculated as number of neighbouring water body cells of a cluster divided by the number of cells of this area. For each city the water-cell-neighbour ratio is calculated for the urban cluster and its boundary area respectively, and then the difference between them is calculated (ratio of urban cluster minus ratio of boundary area). Points highlighted in red are the ones with residual from GWR larger than 1°C, which means they have much larger ΔT_s than the GWR model predicted. While the ones in green have residual smaller than -1°C.

BIBLIOGRAPHY

Ali-Toudert, F. and H. Mayer (2006). "Numerical study on the effects of aspect ratio and orientation of an urban street canyon on outdoor thermal comfort in hot and dry climate." *Build. Environ.* 41.2, pp. 94–108. DOI: 10.1016/j.buildenv.2005.01.013 (cit. on p. 43).

Argüeso, D. et al. (2014). "Temperature response to future urbanization and climate change." *Clim. Dyn.* 42.7-8, pp. 2183–2199. DOI: 10.1007/s00382-013-1789-6 (cit. on pp. 11, 32).

Baer, H. and M. Singer (2016). *Global warming and the political ecology of health: Emerging crises and systemic solutions*. Routledge. DOI: 10.4324/9781315428017 (cit. on p. 79).

Barthelemy, M. (2016). *The Structure and Dynamics of Cities – Urban Data Analysis and Theoretical Modeling*. Cambridge, UK: Cambridge University Press. ISBN: 9781316271377. DOI: 10.1017/9781316271377 (cit. on pp. 20, 81).

Batten, D. F. and D. E. Boyce (1987). "Spatial interaction, transportation, and interregional commodity flow models." *Handbook of regional and urban economics* 1, pp. 357–406. DOI: 10.1016/S1574-0080(00)80012-7 (cit. on p. 29).

Batty, M. (2013). *The New Science of Cities*. Cambridge, MA: MIT Press. ISBN: 978-0262019521 (cit. on pp. 20, 29, 46, 78, 86).

Batty, M. and P. Ferguson (2011). "Defining city size." *Environ. Plan. B* 38.5, pp. 753–756. DOI: 10.1068/b3805ed (cit. on pp. 27, 28).

Batty, M. and P. Longley (1994). *Fractal Cities: A Geometry of Form and Function*. San Diego, CA and London: Academic Press Inc. ISBN: 978-0124555709. URL: http://www.fractalcities.org/ (cit. on pp. 24, 25, 29, 41, 46, 73, 78, 86).

Batty, M., P. Longley, and S. Fotheringham (1989). "Urban growth and form: scaling, fractal geometry, and diffusion-limited aggregation." *Environ. Plan. A* 21.11, pp. 1447–1472. DOI: 10.1068/a211447 (cit. on pp. 29, 46, 78, 86).

Batty, M. and K. Sik Kim (1992). "Form follows function: reformulating urban population density functions." *Urban Stud.* 29.7, pp. 1043–1069. DOI: 10.1080/00420989220081041 (cit. on p. 28).

Benenson, I. and P. M. Torrens (2004). *Geosimulation: Automata-based modeling of urban phenomena*. West Sussex, England: John Wiley & Sons Ltd. ISBN: 9780470843499 (cit. on p. 28).

Best, M. and C. Grimmond (2015). "Key conclusions of the first international urban land surface model comparison project." *Bull. Amer. Meteorol. Soc.* 96.5, pp. 805–819. DOI: 10.1175/BAMS-D-14-00122.1 (cit. on p. 77).

Bettencourt, L. M. A. and J. Lobo (2016). "Urban scaling in Europe." *J. Roy. Soc. Interface* 13.116, p. 20160005. DOI: 10.1098/rsif.2016.0005 (cit. on p. 28).

Biljecki, F. et al. (2016). "Population estimation using a 3D city model: A multi-scale country-wide study in the Netherlands." *PLoS One* 11.6, e0156808. DOI: 10.1371/journal.pone.0156808 (cit. on p. 30).

Biljecki, F. and Y. S. Chow (2022). "Global Building Morphology Indicators." *Comput. Environ. Urban Syst.* 95, p. 101809. DOI: 10.1016/j.compenvurbsys.2022.101809 (cit. on p. 79).

Bohnenstengel, S. et al. (2014). "Impact of anthropogenic heat emissions on London's temperatures." *Q. J. R. Meteorol. Soc.* 140.679, pp. 687–698. DOI: 10.1002/qj.2144 (cit. on pp. 47, 78).

Brinckmann Sven; Bissolli, P. (2016). *DecReg/MiKlip gridded data of near-surface temperature (2m) and wind speed (10m) in Europe for the period 2001-2010.Version v002*. DOI: 10.5676/DWD_CDC/DECREG0110v2 (cit. on p. 54).

Brinckmann, S., S. Krähenmann, and P. Bissolli (2016). "High-resolution daily gridded data sets of air temperature and wind speed for Europe." *Earth Syst. Sci. Data* 8.2, pp. 491–516. DOI: 10.5194/essd-8-491-2016 (cit. on p. 54).

Brzezinski, M. (2014). "Do wealth distributions follow power laws? Evidence from 'rich lists'." *Phys. A* 406, pp. 155–162. DOI: 10.1016/j.physa.2014.03.052 (cit. on p. 82).

Bunde, A. and S. Havlin (1995). "Fractals in Science." Ed. by A. Bunde and S. Havlin. Berlin: Springer-Verlag. Chap. 1, pp. 1–25. ISBN: 3-540-56221-4. URL: https://books.google.de/books?id=dh7rCAAAQBAJ (cit. on pp. 25, 26).

Büttner, G. et al. (2012). *Implementation and achievements of CLC2006*. Tech. Rep. Barcelona: European Topic Centre Land Use and Spatial Information, Eur. Environ. Agency. URL: https://land.copernicus.eu/user-corner/technical-library/implementation-and-achievements-of-clc2006 (cit. on p. 54).

Buyantuyev, A. and J. Wu (2010). "Urban heat islands and landscape heterogeneity: linking spatiotemporal variations in surface temperatures to land-cover and socioeconomic patterns." *Landsc. Ecol.* 25.1, pp. 17–33. DOI: 10.1007/s10980-009-9402-4 (cit. on p. 51).

Cao, C. et al. (2016). "Urban heat islands in China enhanced by haze pollution." *Nat. Commun.* 7, p. 12509. DOI: 10.1038/ncomms12509.

Cao, Q. et al. (2018). "Impacts of future urban expansion on summer climate and heat-related human health in eastern China." *Environ. Int.* 112, pp. 134–146. DOI: 10.1016/j.envint.2017.12.027 (cit. on pp. 4, 11, 32).

Carrothers, G. A. P. (1956). "An historical review of the gravity and potential concepts of human interaction." *J. Am. I. Planners* 22.2, pp. 94–102. URL: http://www.jstor.org/stable/2785468 (cit. on p. 20).

Chapman, S. et al. (2017). "The impact of urbanization and climate change on urban temperatures: a systematic review." *Landsc. Ecol.* 32.10, pp. 1921–1935. DOI: 10.1007/s10980-017-0561-4 (cit. on pp. 4, 8, 11, 13, 14, 32, 40, 41, 45, 71).

Chen, C. et al. (2020). "Attribution of Land-Use/Land-Cover Change Induced Surface Temperature Anomaly: How Accurate Is the First-Order Taylor Series Expansion?" *J. Geophys. Res. Biogeosciences* 125.9, e2020JG005787. DOI: 10.1029/2020JG005787 (cit. on p. 68).

Chun, B. and J.-M. Guldmann (2018). "Impact of greening on the urban heat island: Seasonal variations and mitigation strategies." *Comput. Environ. Urban Syst.* 71, pp. 165–176. DOI: 10.1016/j.compenvurbsys.2018.05.006 (cit. on p. 51).

Clark, C. (1951). "Urban population densities." *J. R. Stat. Soc. Ser. A – G.* 114.4, pp. 490–496. DOI: 10.2307/2981088 (cit. on p. 28).

Dai, Z., J.-M. Guldmann, and Y. Hu (2018). "Spatial regression models of park and land-use impacts on the urban heat island in central Beijing." *Sci. Total Environ.* 626, pp. 1136–1147. DOI: 10.1016/j.scitotenv.2018.01.165 (cit. on p. 51).

Daqing, L. et al. (2011). "Dimension of spatially embedded networks." *Nat. Phys.* 7.6, p. 481. DOI: 10.1038/nphys1932 (cit. on p. 25).

De Munck, C. et al. (2013). "How much can air conditioning increase air temperatures for a city like Paris, France?" *Int. J. Climatol.* 33.1, pp. 210–227. DOI: 10.1002/joc.3415 (cit. on pp. 47, 78).

Deilami, K., M. Kamruzzaman, and Y. Liu (2018). "Urban heat island effect: A systematic review of spatio-temporal factors, data, methods, and mitigation measures." *Int. J. Appl. Earth Obs. Geoinf.* 67, pp. 30–42. DOI: 10.1016/j.jag.2017.12.009 (cit. on pp. 8, 10, 50, 51).

Delloye, J., R. Lemoy, and C. Geoffrey (2018). "Alonso and the Scaling of Urban Profiles." *arXiv.org e-Print archive* arXiv:1801.07512 [physics.soc-ph]. URL: https://arxiv.org/abs/1801.07512 (cit. on p. 81).

Demuzere, M., B. Bechtel, and G. Mills (2019). "Global transferability of local climate zone models." *Urban Clim.* 27, pp. 46–63. DOI: 10.1016/j.uclim.2019.01.005 (cit. on p. 51).

Didan, K. (2015). *MOD13A3 MODIS/Terra vegetation indices monthly L3 global 1km SIN grid V006 (Data set) NASA EOSDIS Land Process.* DOI: 10.5067/MODIS/MOD13Q1.006 (cit. on p. 53).

Du, H. et al. (2016). "Research on the cooling island effects of water body: A case study of Shanghai, China." *Ecol. Indic.* 67, pp. 31–38. DOI: 10.1016/j.ecolind.2016.02.040 (cit. on pp. 69, 93).

Eliasson, I. (2000). "The use of climate knowledge in urban planning." *Landsc. Urban Plan.* 48.1-2, pp. 31–44. DOI: 10.1016/S0169-2046(00)00034-7 (cit. on pp. 11, 13, 32, 45).

Encarnação, S. et al. (2012). "Fractal cartography of urban areas." *Sci. Rep.* 2.527, srep00527. DOI: 10.1038/srep00527 (cit. on p. 24).

Estoque, R. C., Y. Murayama, and S. W. Myint (2017). "Effects of landscape composition and pattern on land surface temperature:

An urban heat island study in the megacities of Southeast Asia." *Sci. Total Environ.* 577, pp. 349–359. DOI: 10.1016/j.scitotenv.2016.10.195 (cit. on p. 4).

Estrada, F., W. W. Botzen, and R. S. Tol (2017). "A global economic assessment of city policies to reduce climate change impacts." *Nat. Clim. Chang.* 7.6, p. 403. DOI: 10.1038/nclimate3301 (cit. on pp. 4, 12, 32, 45, 57).

Fabinger, M. (2012). "Essays on Trade and Imperfectly Competitive Markets." Doctoral dissertation. Harvard University. URL: http://nrs.harvard.edu/urn-3:HUL.InstRepos:9548614 (cit. on p. 81).

Fitzpatrick, M. C. and R. R. Dunn (2019). "Contemporary climatic analogs for 540 North American urban areas in the late 21st century." *Nat. Commun.* 10.1, pp. 1–7. DOI: 10.1038/s41467-019-08540-3 (cit. on p. 76).

Fluschnik, T. et al. (2016). "The size distribution, scaling properties and spatial organization of urban clusters: a global and regional percolation perspective." *Int. J. Geo-Information* 5.7, p. 110. DOI: 10.3390/ijgi5070110 (cit. on pp. 21, 27, 54).

Fotheringham, A. S., C. Brunsdon, and M. Charlton (2003). *Geographically weighted regression: the analysis of spatially varying relationships*. John Wiley & Sons (cit. on p. 55).

Fotheringham, A. S., M. Batty, and P. A. Longley (1989). "Diffusion-limited aggregation and the fractal nature of urban growth." *Pap. Reg. Sci. Assoc.* 67.1, pp. 55–69. DOI: 10.1007/BF01934667 (cit. on pp. 29, 41, 86).

Frankhauser, P. (2008). "Fractal geometry for measuring and modelling urban patterns." *The dynamics of complex urban systems*. Springer, pp. 213–243. DOI: 10.1007/978-3-7908-1937-3_11 (cit. on p. 24).

Frasco, G. F. et al. (2014). "Spatially distributed social complex networks." *Phys. Rev. X* 4.1, p. 011008. DOI: 10.1103/PhysRevX.4.011008 (cit. on p. 29).

Gabaix, X. (2016). "Power laws in economics: An introduction." *J. Econ. Perspect.* 30.1, pp. 185–206. DOI: 10.1257/jep.30.1.185 (cit. on p. 83).

Gabriel, K. M. and W. R. Endlicher (2011). "Urban and rural mortality rates during heat waves in Berlin and Brandenburg, Germany." *Environ. Pollut.* 159.8-9, pp. 2044–2050. DOI: 10.1016/j.envpol.2011.01.016 (cit. on pp. 11, 32, 33, 50).

Galletti, C. S., X. Li, and J. P. Connors (2019). "Establishing the relationship between urban land-cover configuration and night time land-surface temperature using spatial regression." *Int. J. Remote Sens.* 40.17, pp. 6752–6774. DOI: 10.1080/01431161.2019.1594432 (cit. on p. 51).

Geletič, J. et al. (2019). "Inter-/intra-zonal seasonal variability of the surface urban heat island based on local climate zones in three central European cities." *Build. Environ.* 156, pp. 21–32. DOI: 10.1016/j.buildenv.2019.04.011 (cit. on pp. 4, 51).

Georgescu, M. et al. (2013). "Summer-time climate impacts of projected megapolitan expansion in Arizona." *Nat. Clim. Chang.* 3.1, p. 37. DOI: 10.1038/nclimate1656 (cit. on pp. 4, 11, 32).

Glockmann, M. et al. (2022). "Quantitative evidence for leapfrogging in urban growth." *Environ. Plan. B* 49.1, pp. 352–367. DOI: 10.1177/2399808321998713 (cit. on pp. ix, 79).

Gomez-Lievano, A., H. Youn, and L. M. A. Bettencourt (2012). "The statistics of urban scaling and their connection to Zipf's law." *PLoS One* 7.7, e40393. DOI: 10.1371/journal.pone.0040393 (cit. on p. 82).

Grimm, N. B. et al. (2008). "Global change and the ecology of cities." *Science* 319.5864, pp. 756–760. DOI: 10.1126/science.1150195 (cit. on pp. 3, 11, 32, 50).

Grossman-Clarke, S., S. Schubert, and D. Fenner (2017). "Urban effects on summertime air temperature in Germany under climate change." *Int. J. Climatol.* 37.2, pp. 905–917. DOI: {10.1002/joc.4748} (cit. on p. 32).

Gudipudi, R. et al. (2019). "The efficient, the intensive, and the productive: Insights from urban Kaya scaling." *Appl. Energy* 236, pp. 155–162. DOI: 10.1016/j.apenergy.2018.11.054 (cit. on p. 68).

Guérois, M. and D. Pumain (2008). "Built-up encroachment and the urban field: a comparison of forty European cities." *Environ. Plan. B* 40.9, pp. 2186–2203. DOI: 10.1068/a39382 (cit. on p. 22).

Guo, A. et al. (2020). "Influences of urban spatial form on urban heat island effects at the community level in China." *Sustain. Cities Soc.* 53, p. 101972. DOI: 10.1016/j.scs.2019.101972 (cit. on pp. 51, 59).

Haase, D. (2019). "Urban telecouplings." *Telecoupling: Exploring land-use change in a globalised world*. Springer, pp. 261–280. DOI: 10.1007/978-3-030-11105-2_14.

Habeeb, D., J. Vargo, and B. Stone (2015). "Rising heat wave trends in large US cities." *Nat. Hazards* 76.3, pp. 1651–1665. DOI: 10.1007/s11069-014-1563-z (cit. on pp. 11, 32).

He, B.-J. (2018). "Potentials of meteorological characteristics and synoptic conditions to mitigate urban heat island effects." *Urban Clim.* 24, pp. 26–33. DOI: 10.1016/j.uclim.2018.01.004 (cit. on p. 52).

He, C. et al. (2022). "The effects of night-time warming on mortality burden under future climate change scenarios: a modelling study." *Lancet Planet. Health* 6.8, e648–e657. DOI: 10.1016/S2542-5196(22)00139-5 (cit. on pp. 2, 4).

Heaviside, C., H. Macintyre, and S. Vardoulakis (2017). "The urban heat island: implications for health in a changing environment." *Curr. Environ. Health Rep.* 4.3, pp. 296–305. DOI: 10.1007/s40572-017-0150-3 (cit. on pp. 11, 32).

Hooker, J., G. Duveiller, and A. Cescatti (2018). "A global dataset of air temperature derived from satellite remote sensing and weather stations." *Sci. data* 5.1, pp. 1–11. DOI: 10.1038/sdata.2018.246 (cit. on p. 56).

Hoshen, J. and R. Kopelman (1976). "Percolation and cluster distribution. I. Cluster multiple labeling technique and critical concentration algorithm." *Phys. Rev. B* 14.8, pp. 3438–3445. DOI: 10.1103/PhysRevB.14.3438 (cit. on p. 21).

Howard, L. (1818). *The climate of London: deduced from meteorological observations, made at different places in the neighbourhood of the metropolis*. Re-published edtion by The International Association for Urban Climate (IAUC) in 2007. W. Phillips, George Yard, Lombard Street, sold also by J. and A. Arch. URL: http://urban-climate.org/documents/LukeHoward_Climate-of-London-V1.pdf (visited on 09/25/2017) (cit. on p. 3).

Hsieh, C.-M., T. Aramaki, and K. Hanaki (2007). "The feedback of heat rejection to air conditioning load during the nighttime in subtropical climate." *Energy Build.* 39.11, pp. 1175–1182. DOI: 10.1016/j.enbuild.2006.06.016 (cit. on p. 11).

Jian, X., R. A. Olea, and Y.-S. Yu (1996). "Semivariogram modeling by weighted least squares." *Comput. Geosci.* 22.4, pp. 387–397. DOI: 10.1016/0098-3004(95)00095-X (cit. on p. 55).

Jones, B. and B. C. O'Neill (2016). "Spatially explicit global population scenarios consistent with the Shared Socioeconomic Pathways." *Environ. Res. Lett.* 11.8, p. 084003. DOI: 10.1088/1748-9326/11/8/084003 (cit. on p. 30).

Kahneman, D. et al. (2006). "Would you be happier if you were richer? A focusing illusion." *Science* 312.5782, pp. 1908–1910. DOI: 10.1126/science.1129688 (cit. on p. 82).

Kalkstein, L. S. and R. E. Davis (1989). "Weather and human mortality: an evaluation of demographic and interregional responses in the United States." *Ann. Assoc. Am. Geogr.* 79.1, pp. 44–64. DOI: 10.1111/j.1467-8306.1989.tb00249.x (cit. on p. 33).

Kalnay, E. and M. Cai (2003). "Impact of urbanization and land-use change on climate." *Nature* 423.6939, p. 528. DOI: 10.1038/nature01675 (cit. on pp. 4, 11, 32).

Karger, D. N. et al. (2017). "Climatologies at high resolution for the earth's land surface areas." *Sci. data* 4, p. 170122. DOI: 10.1038/sdata.2017.122 (cit. on p. 54).

Khan, H. (2022). "On the climatic synergies at the local, regional, and global scales: the impact on the built environment." PhD thesis. UNSW Sydney. DOI: 10.26190/unsworks/24459 (cit. on pp. 4, 11).

Kim, S. W. and R. D. Brown (2021). "Urban heat island (UHI) variations within a city boundary: A systematic literature review." *Renew. Sustain. Energy Rev.* 148, p. 111256. ISSN: 13640321. DOI: 10.1016/j.rser.2021.111256 (cit. on pp. 8, 13).

Kolokotroni, M. et al. (2012). "London's urban heat island: Impact on current and future energy consumption in office buildings." *Energy Build.* 47, pp. 302–311. DOI: 10.1016/j.enbuild.2011.12.019 (cit. on p. 4).

Krapivsky, P. L., S. Redner, and F. Leyvraz (2000). "Connectivity of growing random networks." *Phys. Rev. Lett.* 85.21, p. 4629. DOI: 10.1103/PhysRevLett.85.4629 (cit. on p. 30).

Krayenhoff, E. S. et al. (2018). "Diurnal interaction between urban expansion, climate change and adaptation in US cities." *Nat. Clim. Chang.* 8.12, p. 1097. DOI: 10.1038/s41558-018-0320-9 (cit. on pp. 32, 33).

Kriewald, S. et al. (2016). *osc: Orthodromic Spatial Clustering*. URL: https://cran.r-project.org/web/packages/osc/index.html (cit. on p. 21).

Krummenauer, L. et al. (2019). "Global drivers of minimum mortality temperatures in cities." *Sci. Total Environ.* 695, p. 133560. DOI: 10.1016/j.scitotenv.2019.07.366 (cit. on pp. 11, 50, 57).

Laaidi, K. et al. (2012). "The impact of heat islands on mortality in Paris during the August 2003 heat wave." *Environ. Health Perspect.* 120.2, pp. 254–259. DOI: 10.1289/ehp.1103532 (cit. on pp. 4, 33).

Lemoy, R. and G. Caruso (2017). "Scaling evidence of the homothetic nature of cities." *arXiv.org e-Print archive* arXiv:1704.06508 [physics.soc-ph]. URL: https://arxiv.org/abs/1704.06508 (cit. on pp. 20, 23, 28).

Lemoy, R. and G. Caruso (2020). "Evidence for the homothetic scaling of urban forms." *Environ. Plan. B* 47.5, pp. 870–888. DOI: 10.1177/2399808318810 (cit. on pp. 20, 22–24, 73).

Levy, M. and S. Solomon (1997). "New evidence for the power-law distribution of wealth." *Phys. A* 242.1-2, pp. 90–94. DOI: 10.1016/S0378-4371(97)00217-3 (cit. on p. 82).

Li, C. et al. (2014). "Interaction between urban microclimate and electric air-conditioning energy consumption during high temperature season." *Appl. Energy* 117, pp. 149–156. DOI: 10.1016/j.apenergy.2013.11.057 (cit. on pp. 11, 47, 78).

Li, D. and E. Bou-Zeid (2013a). "Synergistic interactions between urban heat islands and heat waves: The impact in cities is larger than the sum of its parts." *J. Appl. Meteorol. Climatol.* 52.9, pp. 2051–2064. DOI: 10.1175/JAMC-D-13-02.1 (cit. on pp. 4, 32).

Li, D. et al. (2019a). "Urban heat island: Aerodynamics or imperviousness?" *Sci. Adv.* 5.4, eaau4299. DOI: 10.1126/sciadv.aau4299 (cit. on pp. 61, 68).

Li, H. (2018). "Urban heat island and its influencing mechanism in the city of Berlin." doctoralthesis. Freie Universität Berlin, pp. xiii, 119. DOI: http://dx.doi.org/10.17169/refubium-896 (cit. on pp. 3, 8, 9, 14).

Li, H. et al. (2018). "A new method to quantify surface urban heat island intensity." *Sci. Total Environ.* 624, pp. 262–272. DOI: 10.1016/j.scitotenv.2017.11.360 (cit. on pp. 51, 56, 66, 75).

Li, H. et al. (2019b). "Quantifying urban heat island intensity and its physical mechanism using WRF/UCM." *Sci. Total Environ.* 650,

pp. 3110–3119. DOI: 10.1016/j.scitotenv.2018.10.025 (cit. on pp. 4, 14, 16, 33, 46, 74).

Li, J. et al. (2011). "Impacts of landscape structure on surface urban heat islands: A case study of Shanghai, China." *Remote Sens. Environ.* 115.12, pp. 3249–3263. DOI: 10.1016/j.rse.2011.07.008 (cit. on p. 56).

Li, M. et al. (2020a). "Continental-scale mapping and analysis of 3D building structure." *Remote Sens. Environ.* 245, p. 111859. DOI: 10.1016/j.rse.2020.111859 (cit. on p. 79).

Li, M. et al. (2022). "Global maps of 3D built-up patterns for urban morphological analysis." *Int. J. Appl. Earth Obs. Geoinf.* 114, p. 103048. DOI: 10.1016/j.jag.2022.103048 (cit. on p. 79).

Li, S. et al. (2010). "Investigating spatial non-stationary and scale-dependent relationships between urban surface temperature and environmental factors using geographically weighted regression." *Environ. Model. Softw.* 25.12, pp. 1789–1800. DOI: 10.1016/j.envsoft.2010.06.011 (cit. on p. 51).

Li, X. et al. (2017). "The surface urban heat island response to urban expansion: A panel analysis for the conterminous United States." *Sci. Total Environ.* 605, pp. 426–435. DOI: 10.1016/j.scitotenv.2017.06.229 (cit. on pp. 4, 16, 40, 51, 57, 60, 62, 67, 68).

Li, Y. et al. (2020b). "Strong Intensification of Hourly Rainfall Extremes by Urbanization." *Geophys. Res. Lett.* 47.14. ISSN: 0094-8276, 1944-8007. DOI: 10.1029/2020GL088758 (cit. on p. 11).

Li, Y., D. Rybski, and J. P. Kropp (2021a). "Singularity cities." *Environ. Plan. B* 48.1, pp. 43–59. DOI: 10.1177/2399808319843534 (cit. on pp. ix, 19, 35, 36, 39, 41, 52, 86, 88).

Li, Y. et al. (2020c). "On the influence of density and morphology on the Urban Heat Island intensity." *Nat. Commun.* 11.1, pp. 1–9. DOI: 10.1038/s41467-020-16461-9 (cit. on pp. ix, 31, 52, 53, 56, 58, 66, 67).

Li, Y. et al. (2021b). "Context sensitivity of surface urban heat island at the local and regional scales." *Sustain. Cities Soc.* 74, p. 103146. DOI: 10.1016/j.scs.2021.103146 (cit. on pp. ix, 49).

Li, Z.-L. et al. (2013b). "Satellite-derived land surface temperature: Current status and perspectives." *Remote Sens. Environ.* 131, pp. 14–37. ISSN: 00344257. DOI: 10.1016/j.rse.2012.12.008.

Liang, Z. et al. (2020). "Seasonal and Diurnal Variations in the Relationships between Urban Form and the Urban Heat Island Effect." *Energies* 13.22, p. 5909. DOI: 10.3390/en13225909 (cit. on pp. 16, 52, 73).

Liu, H. et al. (2019). "Seasonal variation of the spatially non-stationary association between land surface temperature and urban landscape." *Remote Sens.* 11.9, p. 1016. DOI: 10.3390/rs11091016 (cit. on p. 51).

Liu, H. et al. (2021a). "Impacts of the evolving urban development on intra-urban surface thermal environment: Evidence from 323

Chinese cities." *Sci. Total Environ.* 771, p. 144810. DOI: 10.1016/j.scitotenv.2020.144810 (cit. on pp. 4, 16, 67, 73, 79).

Liu, H. et al. (2021b). "The influence of urban form on surface urban heat island and its planning implications: Evidence from 1288 urban clusters in China." *Sustain. Cities Soc.* 71, p. 102987. DOI: 10.1016/j.scs.2021.102987 (cit. on pp. 4, 15, 16, 52, 73, 75, 77).

Lovejoy, S. (1982). "Area-perimeter relation for rain and cloud areas." *Science* 216.4542, pp. 185–187. DOI: 10.1126/science.216.4542.185 (cit. on p. 25).

Lowe, M. et al. (2022). "City planning policies to support health and sustainability: an international comparison of policy indicators for 25 cities." *Lancet Glob. Health* 10.6, e882–e894. ISSN: 2214109X. DOI: 10.1016/S2214-109X(22)00069-9.

Lu, B. et al. (2014). "The GWmodel R package: further topics for exploring spatial heterogeneity using geographically weighted models." *Geo-spatial Inf. Sci.* 17.2, pp. 85–101. DOI: 10.1080/10095020.2014.917453 (cit. on p. 56).

Makse, H. A., S. Havlin, and H. E. Stanley (1995). "Modeling urban-growth patterns." *Nature* 377.6550, pp. 608–612. DOI: 10.1038/377608a0 (cit. on pp. 24, 29).

Makse, H. A. et al. (1998). "Modeling urban growth patterns with correlated percolation." *Phys. Rev. E* 58.6, pp. 7054–7062. DOI: 10.1103/PhysRevE.58.7054 (cit. on pp. 25, 26, 29).

Malmgren, R. D. et al. (2009). "On universality in human correspondence activity." *Science* 325.5948, pp. 1696–1700. DOI: 10.1126/science.1174 (cit. on p. 22).

Manoli, G. et al. (2019). "Magnitude of urban heat islands largely explained by climate and population." *Nature* 573.7772, pp. 55–60. DOI: 10.1038/s41586-019-1512-9 (cit. on pp. 14, 16, 40, 52, 60, 61, 63, 67, 68).

Manoli, G. et al. (2020). "Seasonal hysteresis of surface urban heat islands." *Proc. Natl. Acad. Sci. U. S. A.* 117.13, pp. 7082–7089. DOI: 10.1073/pnas.1917554117 (cit. on pp. 4, 16, 68).

Marciotto, E. R., A. P. Oliveira, and S. R. Hanna (2010). "Modeling study of the aspect ratio influence on urban canopy energy fluxes with a modified wall-canyon energy budget scheme." *Build. Environ.* 45.11, pp. 2497–2505. DOI: 10.1016/j.buildenv.2010.05.012 (cit. on pp. 33, 43, 46, 73, 77).

Martilli, A., A. Clappier, and M. W. Rotach (2002). "An urban surface exchange parameterisation for mesoscale models." *Bound.-layer Meteor.* 104.2, pp. 261–304. DOI: https://doi.org/10.1023/A:1016099921195 (cit. on pp. 34, 77).

Masson-Delmotte, V. et al. (2021). *Climate Change 2021: The Physical Science Basis*. IPCC Sixth Assessment Report. URL: https://www.ipcc.ch/report/ar6/wg1/ (visited on 10/25/2022) (cit. on p. 2).

Mathew, A., S. Khandelwal, and N. Kaul (2017). "Investigating spatial and seasonal variations of urban heat island effect over Jaipur city

and its relationship with vegetation, urbanization and elevation parameters." *Sustain. Cities Soc.* 35, pp. 157–177. DOI: 10.1016/j.scs.2017.07.013 (cit. on pp. 56, 59, 67, 79).

Middel, A. et al. (2014). "Impact of urban form and design on mid-afternoon microclimate in Phoenix Local Climate Zones." *Landsc. Urban Plan.* 122, pp. 16–28. DOI: 10.1016/j.landurbplan.2013.11.004 (cit. on pp. 13, 45).

Mills, G. (2006). "Progress toward sustainable settlements: a role for urban climatology." *Theor. Appl. Climatol.* 84.1-3, pp. 69–76. DOI: 10.1007/s00704-005-0145-0 (cit. on pp. 12, 47).

Mills, G. et al. (2010). "Climate information for improved planning and management of mega cities (needs perspective)." *Procedia Environ. Sci.* 1, pp. 228–246. DOI: 10.1016/j.proenv.2010.09.015 (cit. on pp. 12, 47, 74).

Mirzaei, P. A. and F. Haghighat (2010). "Approaches to study Urban Heat Island - Abilities and limitations." *Build. Environ.* 45.10, pp. 2192–2201. DOI: 10.1016/j.buildenv.2010.04.001 (cit. on pp. 6–9).

Morabito, M. et al. (2020). "Surface urban heat islands in Italian metropolitan cities: Tree cover and impervious surface influences." *Sci. Total Environ.* 751, p. 142334. DOI: 10.1016/j.scitotenv.2020.142334 (cit. on p. 56).

Morgan, K. (2004). "The exaggerated death of geography: learning, proximity and territorial innovation systems." *J. Econ. Geogr.* 4.1, pp. 3–21. DOI: 10.1093/jeg/4.1.3 (cit. on p. 20).

Nakaya, T. et al. (2014). *GWR4 windows application for geographically weighted regression modeling*. Tech. Rep. Tempe: Geoda Center, Arizona State University. URL: https://sgsup.asu.edu/sites/default/files/SparcFiles/gwr4manual_409.pdf (cit. on p. 55).

Neter, J. et al. (1996). *Applied linear statistical models*. Irwin Chicago (cit. on p. 59).

Ng, E. (2012). "Towards planning and practical understanding of the need for meteorological and climatic information in the design of high-density cities: A case-based study of Hong Kong." *Int. J. Climatol.* 32.4, pp. 582–598. DOI: 10.1002/joc.2292 (cit. on pp. 12, 33, 47, 74).

Nordbeck, S. (1971). "Urban allometric growth." *Geogr. Ann. B* 53.1, pp. 54–67. DOI: 10.1080/04353684.1971.11879355 (cit. on p. 27).

Ochola, E. M. et al. (2020). "Inter-local climate zone differentiation of land surface temperatures for Management of Urban Heat in Nairobi City, Kenya." *Urban Clim.* 31, p. 100540. DOI: 10.1016/j.uclim.2019.100540 (cit. on p. 51).

Oke, T. R. (1973). "City size and the urban heat island." *Atmos. Environ.* 7.8, pp. 769–779. DOI: 10.1016/0004-6981(73)90140-6 (cit. on pp. 2, 13, 40, 41, 45, 46).

Oke, T. R. (1981). "Canyon geometry and the nocturnal urban heat island: comparison of scale model and field observations." *J. Clim.*

1.3, pp. 237–254. DOI: 10.1002/joc.3370010304 (cit. on pp. 4, 6, 8, 32, 33, 46, 73).
Oke, T. R. (1982). "The energetic basis of the urban heat island." *Q. J. R. Meteorol. Soc.* 108.455, pp. 1–24. DOI: 10.1002/qj.49710845502 (cit. on pp. 32, 73).
Oke, T. R. (1984). "Towards a prescription for the greater use of climatic principles in settlement planning." *Energy Build.* 7.1, pp. 1–10. DOI: 10.1016/0378-7788(84)90040-9 (cit. on pp. 12, 47, 74, 77).
Oke, T. R. (1987). *Boundary Layer Climates*. 2nd. Methuen, London. DOI: 10.4324/9780203407219 (cit. on pp. 13, 41, 45, 47, 78).
Oke, T. R. (2006). "Towards better scientific communication in urban climate." *Theor. Appl. Climatol.* 84.1-3, pp. 179–190. DOI: 10.1007/s00704-005-0153-0 (cit. on pp. 12, 39, 47).
Oke, T. R. et al. (2017). *Urban climates*. Cambridge University Press. DOI: 10.1017/9781139016476 (cit. on pp. 3, 4, 6–10, 12, 14, 16, 32, 33, 40, 46, 47, 50, 52, 69, 73, 77–79).
Patz, J. A. et al. (2005). "Impact of regional climate change on human health." *Nature* 438.7066, p. 310. DOI: 10.1038/nature04188 (cit. on pp. 11, 32).
Peiravian, F., A. Kermanshah, and S. Derrible (2014). "Spatial data analysis of complex urban systems." *2014 IEEE International Conference on Big Data*. IEEE, pp. 1–6. DOI: 10.1109/BigData.2014.7004432 (cit. on p. 22).
Peng, S. et al. (2012). "Surface Urban Heat Island Across 419 Global Big Cities." *Environ. Sci. Technol.* 46.2, pp. 696–703. DOI: 10.1021/es2030438 (cit. on pp. 4, 16, 39, 52, 54, 60, 67, 69).
Pfähler, W. (1985). "Relative Concentration Curve: Functional Form and Measures of Non-Proportionality." *B. of Econ. Res.* 37.3, pp. 201–211. DOI: 10.1111/j.1467-8586.1985.tb00194.x (cit. on p. 82).
Pierer, C. and F. Creutzig (2019). "Star-shaped cities alleviate trade-off between climate change mitigation and adaptation." *Environ. Res. Lett.* DOI: 10.1088/1748-9326/ab2081.
Ren, T., W. Zhou, and J. Wang (2021). "Beyond intensity of urban heat island effect: A continental scale analysis on land surface temperature in major Chinese cities." *Sci. Total Environ.* 791, p. 148334. DOI: 10.1016/j.scitotenv.2021.148334 (cit. on p. 4).
Rozenfeld, H. D. et al. (2008). "Laws of Population Growth." *Proc. Natl. Acad. Sci. U. S. A.* 105.48, pp. 18702–18707. DOI: 10.1073/pnas.0807435105 (cit. on pp. 21, 36, 54).
Rozenfeld, H. D. et al. (2011). "The Area and Population of Cities: New Insights from a Different Perspective on Cities." *Am. Econ. Rev.* 101.5, pp. 2205–2225. DOI: 10.1257/aer.101.5.2205 (cit. on pp. 21, 54).
Runnalls, K. and T. R. Oke (2000). "Dynamics and controls of the near-surface heat island of Vancouver, British Columbia." *Phys. Geogr.* 21.4, pp. 283–304. DOI: 10.1080/02723646.2000.10642711 (cit. on pp. 13, 41, 43, 45, 47, 77, 78).

Rybski, D. (2016). "Relating urban scaling, fundamental allometry, and density scaling." *arXiv.org e-Print archive* arXiv:1609.01217 [physics.soc-ph]. URL: https://arxiv.org/abs/1609.01217 (cit. on p. 27).

Rybski, D., A. G. C. Ros, and J. P. Kropp (2013). "Distance weighted city growth." *Phys. Rev. E* 87.4, p. 042114. DOI: 10.1103/PhysRevE.87.042114 (cit. on pp. 20, 21, 23, 26, 28, 29, 35, 39, 72).

Rybski, D. et al. (2017). "Cities as nuclei of sustainability?" *Environ. Plan. B* 44.3, pp. 425–440. DOI: 10.1177/0265813516638340 (cit. on p. 27).

Rybski, D. and Y. Li (2021a). "Chapter 27: Comparing power laws and exponentials in simulations of gravitational growth." *Handbook on Entropy, Complexity and Spatial Dynamics*. Cheltenham, UK: Edward Elgar Publishing. DOI: 10.4337/9781839100598.00037 (cit. on p. ix).

Rybski, D. et al. (2021b). "Modeling urban morphology by unifying Diffusion-Limited Aggregation and Stochastic Gravitation." *Findings*, p. 22296. DOI: 10.32866/001c.22296 (cit. on pp. ix, 79).

Salamanca, F. et al. (2014). "Anthropogenic heating of the urban environment due to air conditioning." *J. Geophys. Res. Atmos.* 119.10, pp. 5949–5965. DOI: 10.1002/2013JD021225 (cit. on pp. 47, 78).

Schatz, J. and C. J. Kucharik (2015). "Urban climate effects on extreme temperatures in Madison, Wisconsin, USA." *Environ. Res. Lett.* 10.9, p. 094024. DOI: 10.1088/1748-9326/10/9/094024 (cit. on pp. 11, 32, 45).

Schläpfer, M., J. Lee, and L. M. A. Bettencourt (2015). "Urban Skylines: building heights and shapes as measures of city size." *arXiv.org e-Print archive* arXiv:1512.00946 [physics.soc-ph]. URL: https://arxiv.org/abs/1512.00946 (cit. on pp. 20, 27).

Schubert, S. (2013). "Development and evaluation of a double-canyon urban canopy scheme, and estimation of urban heat island mitigation effects." PhD thesis. Freie Universität Berlin Berlin. DOI: http://dx.doi.org/10.17169/refubium-15766 (cit. on pp. 3, 9, 14, 72).

Schubert, S. and S. Grossman-Clarke (2014). "Evaluation of the coupled COSMO-CLM/DCEP model with observations from BUBBLE." *Q. J. R. Meteorolog. Soc.* 140.685, pp. 2465–2483. DOI: 10.1002/qj.2311 (cit. on pp. 34, 72).

Schubert, S. and S. Grossman-Clarke (2013). "The influence of green areas and roof albedos on air temperatures during extreme heat events in Berlin, Germany." *Meteorol. Z.* 22.2, pp. 131–143. DOI: 10.1127/0941-2948/2013/0393 (cit. on pp. 12, 33–35, 37–39, 46, 72, 74).

Schubert, S., S. Grossman-Clarke, and A. Martilli (2012). "A double-canyon radiation scheme for multi-layer urban canopy models." *Bound.-Layer Meteor.* 145.3, pp. 439–468. DOI: 10.1007/s10546-012-9728-3 (cit. on pp. 14, 34, 38, 71, 72, 77).

Shahmohamadi, P. et al. (2011). "The impact of anthropogenic heat on formation of urban heat island and energy consumption balance." *Urban Stud.* 2011. DOI: 10.1155/2011/497524 (cit. on pp. 4, 47, 78).

Shen, G. (2002). "Fractal dimension and fractal growth of urbanized areas." *Int. J. Geogr. Inf. Sci.* 16.5, pp. 419–437. DOI: 10.1080/13658810210137013 (cit. on p. 26).

Simon, A. et al. (2010). *Urban Morphological Zones version F2vo: Definition and procedural steps*. Tech. Rep. Barcelona: European Topic Centre Land Use and Spatial Information, Eur. Environ. Agency. URL: https://www.eea.europa.eu/data-and-maps/data/urban-morphological-zones-2000-1 (cit. on p. 53).

Singh, P., N. Kikon, and P. Verma (2017). "Impact of land use change and urbanization on urban heat island in Lucknow city, Central India. A remote sensing based estimate." *Sustain. Cities Soc.* 32, pp. 100–114. DOI: 10.1016/j.scs.2017.02.018 (cit. on p. 51).

Song, J. et al. (2020). "Effects of building density on land surface temperature in China: Spatial patterns and determinants." *Landsc. Urban Plan.* 198, p. 103794. DOI: 10.1016/j.landurbplan.2020.103794 (cit. on pp. 51, 56, 66, 67, 75, 79).

Song, J. et al. (2014). "The relationships between landscape compositions and land surface temperature: Quantifying their resolution sensitivity with spatial regression models." *Landsc. Urban Plan.* 123, pp. 145–157. DOI: 10.1016/j.landurbplan.2013.11.014 (cit. on p. 51).

Stanley, H. E. (1999). "Scaling, universality, and renormalization: Three pillars of modern critical phenomena." *Rev. Mod. Phys.* 71.2, S358–S366. DOI: 10.1103/RevModPhys.71.S358 (cit. on p. 22).

Steppeler, J. et al. (2003). "Meso-gamma scale forecasts using the nonhydrostatic model LM." *Meteorol. Atmos. Phys.* 82.1-4, pp. 75–96. DOI: 10.1007/s00703-001-0592-9 (cit. on p. 34).

Stewart, I. D. (2011). "Redefining the urban heat island." PhD thesis. University of British Columbia Vancouver. DOI: 10.14288/1.0072360 (cit. on pp. 8, 10).

Stewart, I. D. and G. Mills (2021a). *The Urban Heat Island: A guid book*. Elsevier. ISBN: 978-0-12-815017-7. DOI: https://doi.org/10.1016/C2017-0-02872-0 (cit. on pp. 3, 4, 6, 10).

Stewart, I. D. and T. R. Oke (2006). "Methodological concerns surrounding the classification of urban and rural climate stations to define urban heat island magnitude." *preprints of ICUC6 Göteborg* 431 (cit. on pp. 11, 39).

Stewart, I. D. and T. R. Oke (2012). "Local climate zones for urban temperature studies." *Bull. Amer. Meteorol. Soc.* 93.12, pp. 1879–1900. DOI: 10.1175/BAMS-D-11-00019.1 (cit. on pp. 36, 51).

Stewart, I. D. et al. (2021b). "Time Evolution of the Surface Urban Heat Island." *Earths Future*. ISSN: 2328-4277, 2328-4277. DOI: 10.1029/2021EF002178 (cit. on p. 10).

Stewart, J. Q. (1948). "Demographic gravitation: evidence and applications." *Sociometry* 11.1/2, pp. 31–58. DOI: 10.2307/2785468 (cit. on p. 20).

Stewart, J. Q. and W. Warntz (1958). "Physics of population distribution." *J. Regional Sci.* 1.1, pp. 99–121. DOI: 10.1111/j.1467-9787.1958.tb01366.x (cit. on p. 27).

Stone, B., J. J. Hess, and H. Frumkin (2010). "Urban form and extreme heat events: are sprawling cities more vulnerable to climate change than compact cities?" *Environ. Health Perspect.* 118.10, pp. 1425–1428. DOI: 10.1289/ehp.0901879 (cit. on pp. 33, 46, 78).

Straka, M. and S. Sodoudi (2019). "Evaluating climate change adaptation strategies and scenarios of enhanced vertical and horizontal compactness at urban scale (a case study for Berlin)." *Landsc. Urban Plan.* 183, pp. 68–78. DOI: 10.1016/j.landurbplan.2018.11.006 (cit. on pp. 12, 33, 40, 46, 74).

Su, Y.-F., G. M. Foody, and K.-S. Cheng (2012). "Spatial non-stationarity in the relationships between land cover and surface temperature in an urban heat island and its impacts on thermally sensitive populations." *Landsc. Urban Plan.* 107.2, pp. 172–180. DOI: 10.1016/j.landurbplan.2012.05.016 (cit. on pp. 51, 93).

Sultana, S. and A. Satyanarayana (2020). "Assessment of urbanisation and urban heat island intensities using landsat imageries during 2000–2018 over a sub-tropical Indian City." *Sustain. Cities Soc.* 52, p. 101846. DOI: 10.1016/j.scs.2019.101846 (cit. on p. 51).

Szymanowski, M. and M. Kryza (2012). "Local regression models for spatial interpolation of urban heat island—an example from Wrocław, SW Poland." *Theor. Appl. Climatol.* 108.1-2, pp. 53–71. DOI: 10.1007/s00704-011-0517-6 (cit. on p. 51).

Taha, H. (1997). "Urban climates and heat islands: albedo, evapotranspiration, and anthropogenic heat." *Energy Build.* 25.2, pp. 99–103. DOI: 10.1016/S0378-7788(96)00999-1 (cit. on pp. 4, 47, 77).

Tan, J. et al. (2010). "The urban heat island and its impact on heat waves and human health in Shanghai." *Int. J. Biometeorol.* 54.1, pp. 75–84. DOI: 10.1007/s00484-009-0256-x (cit. on pp. 2, 4, 11, 32, 45, 50).

Theeuwes, N. et al. (2014). "Seasonal dependence of the urban heat island on the street canyon aspect ratio." *Q. J. R. Meteorol. Soc.* 140.684, pp. 2197–2210. DOI: 10.1002/qj.2289 (cit. on pp. 9, 77).

UN-Habitat (2016). *New urban agenda*, pp. 1–27. URL: https://habitat3.org/the-new-urban-agenda (visited on 10/25/2022) (cit. on pp. 1, 2, 79).

UNEP (2021). *Beating the Heat: A Sustainable Cooling Handbook for Cities.* Nairobi, Kenya. URL: https://www.unep.org/resources/report/beating-heat-sustainable-cooling-handbook-cities (visited on 10/25/2022) (cit. on pp. 2, 11, 79).

UNEP and UN-Habitat (2021). *Global Environment for Cities-GEO for Cities: Towards Green and Just Cities*. UNEP, Nairobi. URL: https:

//www.unep.org/resources/report/geo-cities-towards-green-and-just-cities (visited on 10/25/2022) (cit. on pp. 1, 2, 79).

United Nations Population Division (2019). "World Population Prospects 2019: Highlights." URL: https://population.un.org/wpp/Publications/Files/WPP2019%5C_Highlights.pdf (visited on 06/21/2019) (cit. on pp. 1, 2, 11, 12, 45).

Van den Broek d'Obrenan, H. and R. Huxley (2022). "Measuring what matters: supporting cities in tackling climate and health challenges." *Lancet Glob. Health* 10.6, e788–e789. ISSN: 2214109X. DOI: 10.1016/S2214-109X(22)00198-X (cit. on p. 1).

Van Hove, L. et al. (2015). "Temporal and spatial variability of urban heat island and thermal comfort within the Rotterdam agglomeration." *Build. Environ.* 83, pp. 91–103. DOI: 10.1016/j.buildenv.2014.08.029 (cit. on pp. 33, 46, 74).

Vardoulakis, S. and P. Kinney (2019). "Grand challenges in sustainable cities and health." *Front. Sustain. Cities* 1, p. 7. DOI: 10.3389/frsc.2019.00007 (cit. on p. 1).

Vlahov, D. and S. Galea (2002). "Urbanization, urbanicity, and health." *J. Urban Health* 79.1, S1–S12. DOI: 10.1093/jurban/79.suppl_1.S1 (cit. on p. 1).

Volpati, V. and M. Barthelemy (2018). "The spatial organization of the population density in cities." *arXiv.org e-Print archive* arXiv:1804.00855 [physics.soc-ph]. URL: https://arxiv.org/abs/1804.00855 (cit. on p. 30).

Wagenmakers, E.-J. and S. Farrell (2004). "AIC model selection using Akaike weights." *Psychon. Bull. Rev.* 11.1, pp. 192–196. DOI: 10.3758/BF03206482 (cit. on p. 43).

Wan, Z., S. Hook, and G. Hulley (2015). "MOD11A2 MODIS/Terra land surface temperature/emissivity 8-day L3 global 1km SIN grid V006." *NASA EOSDIS Land Processes DAAC* 10. DOI: 10.5067/MODIS/MYD11A2.006 (cit. on pp. 10, 53).

Wang, J. et al. (2015). "Spatiotemporal variation in surface urban heat island intensity and associated determinants across major Chinese cities." *Remote Sens.* 7.4, pp. 3670–3689. DOI: 10.3390/rs70403670 (cit. on p. 51).

Wang, Y., Q. Zhan, and W. Ouyang (2019). "How to quantify the relationship between spatial distribution of urban waterbodies and land surface temperature?" *Sci. Total Environ.* 671, pp. 1–9. DOI: 10.1016/j.scitotenv.2019.03.377 (cit. on pp. 59, 69, 93).

Watkins, R. et al. (2002). "The London Heat Island: results from summertime monitoring." *Building Serv. Eng. Res. Technol.* 23.2, pp. 97–106. DOI: 10.1191/0143624402bt031oa (cit. on p. 30).

White, R., G. Engelen, and I. Uljee (2015). *Modeling cities and regions as complex systems: From theory to planning applications*. Cambridge, MA: MIT Press. ISBN: 9780262029568. DOI: 10.7551/mitpress/9780262029568.001.0001 (cit. on p. 20).

Wickramasinghe, S. et al. (2018). "Modeling spatial social complex networks for dynamical processes." *Complexity* 2018, p. 1428719. DOI: 10.1155/2018/1428719 (cit. on p. 29).

Witten Jr., T. A. and L. M. Sander (1981). "Diffusion-limited aggregation, a kinetic critical phenomenon." *Phys. Rev. Lett.* 47.19, pp. 1400–1403. DOI: 10.1103/PhysRevLett.47.1400 (cit. on pp. 29, 41, 86).

Wouters, H. et al. (2017). "Heat stress increase under climate change twice as large in cities as in rural areas: A study for a densely populated midlatitude maritime region." *Geophys. Res. Lett.* 44.17, pp. 8997–9007. DOI: 10.1002/2017GL074889 (cit. on p. 4).

Yang, J. et al. (2019). "Spatial differentiation of urban wind and thermal environment in different grid sizes." *Urban Clim.* 28, p. 100458. DOI: 10.1016/j.uclim.2019.100458 (cit. on p. 51).

Yin, C. et al. (2018). "Effects of urban form on the urban heat island effect based on spatial regression model." *Sci. Total Environ.* 634, pp. 696–704. DOI: 10.1016/j.scitotenv.2018.03.350 (cit. on pp. 46, 51, 56, 59, 74).

Yu, Z. et al. (2018). "Strong contributions of local background climate to the cooling effect of urban green vegetation." *Sci. Rep.* 8.1, pp. 1–9. DOI: 10.1038/s41598-018-25296-w (cit. on pp. 14, 59).

Zhang, P. et al. (2012). "Exploring the influence of impervious surface density and shape on urban heat islands in the northeast United States using MODIS and Landsat." *Can. J. Remote Sens.* 38.4, pp. 441–451. DOI: 10.5589/m12-036 (cit. on pp. 14, 16, 52, 57, 66, 67, 73, 75, 77, 79).

Zhang, T. et al. (2022a). "A global dataset of daily maximum and minimum near-surface air temperature at 1 km resolution over land (2003–2020)." *Earth Syst. Sci. Data* 14.12, pp. 5637–5649. DOI: 10.5194/essd-14-5637-2022 (cit. on p. 79).

Zhang, T. et al. (2022b). "Estimating 1 km gridded daily air temperature using a spatially varying coefficient model with sign preservation." *Remote Sens. Environ.* 277, p. 113072. DOI: 10.1016/j.rse.2022.113072 (cit. on p. 79).

Zhang, Y., A. Middel, and B. Turner (2019). "Evaluating the effect of 3D urban form on neighborhood land surface temperature using Google Street View and geographically weighted regression." *Landsc. Ecol.* 34.3, pp. 681–697. DOI: 10.1007/s10980-019-00794-y (cit. on p. 51).

Zhao, L. et al. (2014). "Strong contributions of local background climate to urban heat islands." *Nature* 511.7508, p. 216. DOI: 10.1038/nature13462 (cit. on pp. 4, 13, 32, 40, 41, 45, 52, 60, 63).

Zhao, L. et al. (2018). "Interactions between urban heat islands and heat waves." *Environ. Res. Lett.* 13.3, p. 034003. DOI: 10.1088/1748-9326/aa9f73 (cit. on pp. 4, 11, 32, 45).

Zhao, M. et al. (2022). "A global dataset of annual urban extents (1992–2020) from harmonized nighttime lights." *Earth Syst. Sci. Data* 14.2, pp. 517–534. DOI: 10.5194/essd-14-517-2022 (cit. on p. 79).

Zhou, B. (2017). "On the assessment of surface urban heat island: size, urban form, and seasonality." doctoralthesis. Universität Potsdam, pp. xiii, 119. URL: https://publishup.uni-potsdam.de/frontdoor/index/index/docId/40438 (cit. on pp. 3, 5, 9, 16, 75, 77, 79).

Zhou, B., D. Rybski, and J. P. Kropp (2013). "On the statistics of urban heat island intensity." *Geophys. Res. Lett.* 40.20, pp. 5486–5491. DOI: 10.1002/2013GL057320 (cit. on pp. 16, 35, 39, 40, 51, 54, 55, 68, 73).

Zhou, B., D. Rybski, and J. P. Kropp (2017). "The role of city size and urban form in the surface urban heat island." *Sci. Rep.* 7.1, p. 4791. DOI: 10.1038/s41598-017-04242-2 (cit. on pp. 14–16, 24, 26, 30, 33, 40, 41, 46, 52–54, 57, 59, 66, 67, 73, 75, 77, 78).

Zhou, D. et al. (2014). "Surface urban heat island in China's 32 major cities: Spatial patterns and drivers." *Remote Sens. Environ.* 152, pp. 51–61. DOI: 10.1016/j.rse.2014.05.017 (cit. on pp. 4, 52, 56, 59, 60).

Zhou, D. et al. (2016). "Climate–vegetation control on the diurnal and seasonal variations of surface urban heat islands in China." *Environ. Res. Lett.* 11.7, p. 074009. DOI: 10.1088/1748-9326/11/7/074009 (cit. on pp. 4, 60, 62, 63, 66).

Zhou, D. et al. (2019a). "Satellite remote sensing of surface urban heat islands: progress, challenges, and perspectives." *Remote Sens.* 11.1, p. 48. DOI: 10.3390/rs11010048 (cit. on pp. 3–5, 8, 10, 16, 50, 51).

Zhou, W., G. Huang, and M. L. Cadenasso (2011). "Does spatial configuration matter? Understanding the effects of land cover pattern on land surface temperature in urban landscapes." *Landsc. Urban Plan.* 102.1, pp. 54–63. DOI: 10.1016/j.landurbplan.2011.03.009 (cit. on p. 59).

Zhou, X. and H. Chen (2018). "Impact of urbanization-related land use land cover changes and urban morphology changes on the urban heat island phenomenon." *Sci. Total Environ.* 635, pp. 1467–1476. DOI: 10.1016/j.scitotenv.2018.04.091 (cit. on pp. 4, 13, 14, 33, 73, 77).

Zhou, Y., D. Li, and X. Li (2019b). "The effects of surface heterogeneity scale on the flux imbalance under free convection." *J. Geophys. Res. Atmos.* 124.15, pp. 8424–8448. DOI: 10.1029/2018JD029550 (cit. on p. 51).

Zhou, Y. et al. (2022). "Satellite mapping of urban built-up heights reveals extreme infrastructure gaps and inequalities in the Global South." *Proc. Natl. Acad. Sci. U. S. A.* 119.46, e2214813119. DOI: 10.1073/pnas.221481311 (cit. on p. 79).

Zipf, G. K. (1946). "The P_1P_2/D hypothesis: on the intercity movement of persons." *Am. Social. Rev.* 11.6, pp. 677–686. DOI: 10.2307/2087063 (cit. on p. 20).

DECLARATION

I hereby declare that I have not submitted the thesis at any other university and that I prepared it without illegal assistance.

Potsdam, June 17, 2023

Yunfei Li

COLOPHON

This document was typeset using the typographical look-and-feel `classicthesis` developed by André Miede and Ivo Pletikosić. The style was inspired by Robert Bringhurst's seminal book on typography "*The Elements of Typographic Style*". `classicthesis` is available for both LaTeX and LyX:

https://bitbucket.org/amiede/classicthesis/

Happy users of `classicthesis` usually send a real postcard to the author, a collection of postcards received so far is featured here:

http://postcards.miede.de/